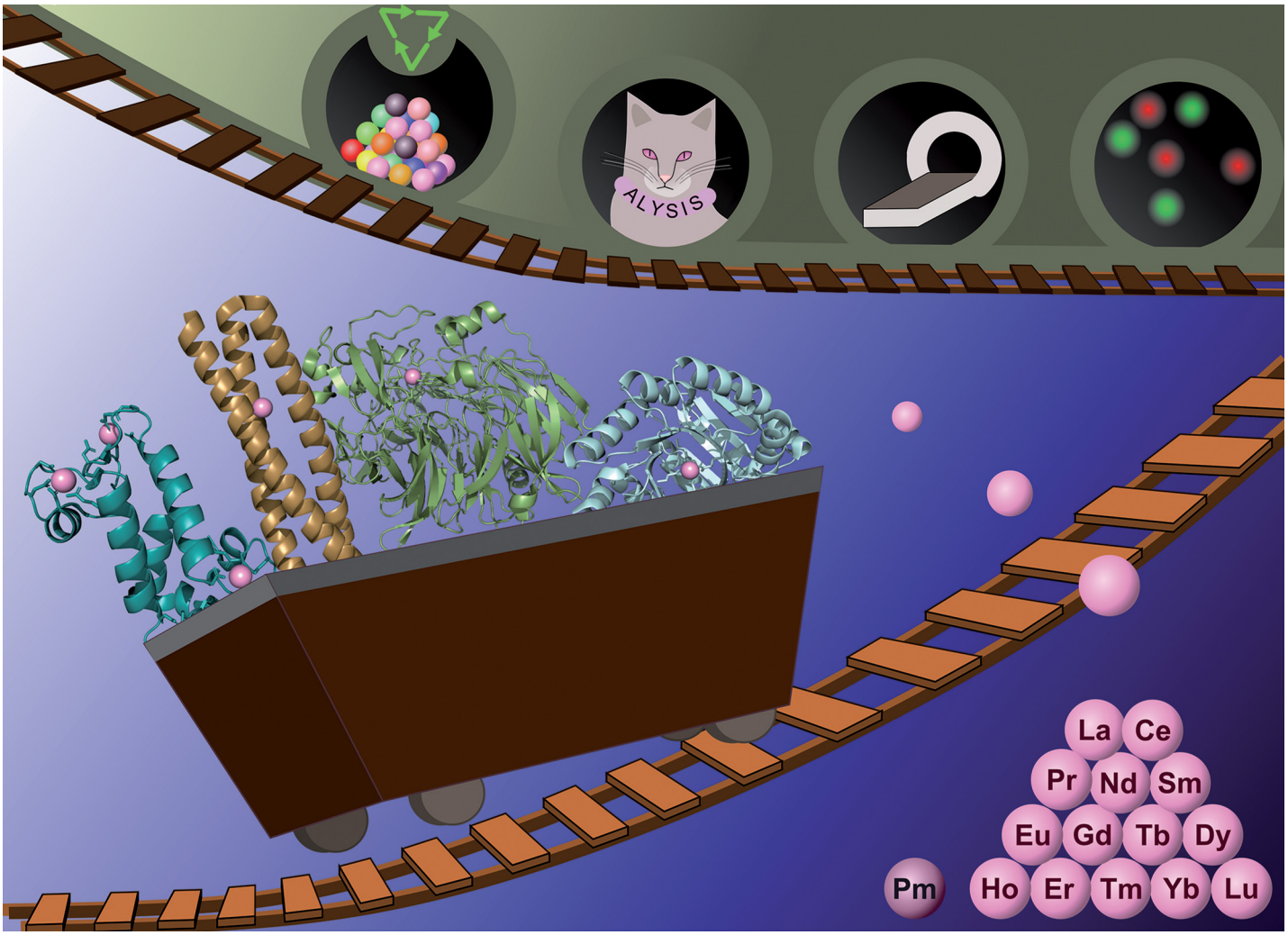

Showcasing research from Dr Hureau's laboratory, Laboratoire de Chimie de Coordination (LCC), CNRS, Toulouse, France.

Lanthanide(III)-binding peptides and proteins: coordination properties and applications

Our review provides a critical overview on the structural, thermodynamic and kinetic properties of both natural and artificial lanthanide(III)-binding peptides and proteins, as well as their emerging applications in imaging, Ln recovery and recycling, and catalysis.

Image reproduced by permission of Emilie Mathieu from *Chem. Soc. Rev.*, 2025, **54**, 9245.

As featured in:

See Enrico Falcone, Emilie Mathieu and Christelle Hureau, *Chem. Soc. Rev.*, 2025, **54**, 9245.

ROYAL SOCIETY OF CHEMISTRY

rsc.li/chem-soc-rev

Registered charity number: 207890

Chem Soc Rev

REVIEW ARTICLE

View Article Online
View Journal | View Issue

Open Access Article. Published on 22 September 2025. Downloaded on 4/1/2026 8:13:17 PM.
This article is licensed under a Creative Commons Attribution-NonCommercial 3.0 Unported Licence.

Check for updates

Cite this: *Chem. Soc. Rev.*, 2025, **54**, 9245

Received 21st December 2024

DOI: 10.1039/d4cs01148a

rsc.li/chem-soc-rev

Lanthanide(III)-binding peptides and proteins: coordination properties and applications

Enrico Falcone, *† Emilie Mathieu *† and Christelle Hureau

Lanthanides play a crucial role in modern medicine and technology as well as in the metabolism of methylotrophic bacteria. In this context, the research on lanthanide-binding peptides and proteins is an active and rapidly developing field. This comprehensive and critical review focuses on the structural, thermodynamic (affinity and selectivity) and kinetic parameters governing the interaction of Ln^{3+} ions with different peptides and proteins, including both naturally occurring and *de novo*-designed scaffolds. It thus provides guidelines and future directions for the rational design of Ln-binding peptides and proteins with suitable features for the main applications explored to date, including luminescent sensing, magnetic resonance imaging, Ln separation and recovery and Ln-based (photo)-catalysis.

1. Introduction

1.1 Context and scope

Lanthanides (Ln) are f-block elements known for their unique magnetism and luminescence properties. They are used in a wide variety of fields: as contrast agents in medicine, in laser technology, in superconductors and in permanent magnets.[1] Rare earth elements (REE), which include Ln, lanthanum (La), yttrium (Y) and scandium (Sc), have been identified as strategic resources by the European Union (EU).[2] Indeed, many advanced technologies depend on them, and China remains the main exporter of these resources, supplying over 98% of REE importation to the EU. Of note, the mining and extraction of REE have a deleterious impact on the environment.[3]

Even before the emergence of interest in Ln biochemistry due to the discovery of the first Ln-utilizing bacteria in the 2010s,[4–7] the design of Ln^{3+}-binding peptides was an intensive research field aimed at exploiting the unique physical properties of Ln^{3+} ions for applications in sensing or imaging.[8]

The discovery of Ln-utilizing bacteria has been accompanied by the identification of natural Ln^{3+}-binding proteins and Ln^{3+}–enzymes, paving the way for a better description of the lanthanome, which corresponds to the proteins involved in Ln^{3+}-uptake, trafficking and utilisation.[9–12] These findings have inspired a large community of biologists and chemists, resulting in a proliferation of studies on the rational design of Ln-binding peptides and proteins, and their applications in biomedicine,[13] biohydrometallurgy,[14,15] and catalysis.[16–21]

Previous reviews in the field focused on the rational design of lanthanide-binding peptides,[8] and a general presentation of the coordination of f-block elements to bio-relevant ligands, including peptides and proteins.[22] Here, we first discuss some critical parameters of Ln^{3+} aqueous chemistry and the design of peptides and proteins with a high affinity for Ln^{3+} ions. Then, we provide guidelines on how selectivity against metal ions (Ca^{2+}, actinides (An^{3+}), d-block metal ions) or among Ln^{3+} can be achieved, and on how to include kinetic considerations in the description of these systems. Last, we highlight recent applications for sensing, MRI, Ln separation and catalysis. In this review, we focus on Ln^{3+}-binding peptides and proteins using natural and/or unnatural amino acids, excluding peptides and proteins functionalized with macrocycles such as DOTA, some of which were reviewed in ref. 23. This choice was driven by the focus on the interplay between the structure and the coordination properties (affinity, selectivity and kinetics) of Ln^{3+}-binding peptides and proteins scaffold, which do not apply to macrocycles. Nevertheless, small chelators will be occasionally discussed to introduce key features and concepts (*e.g.* selectivity) useful for Ln-binding peptides and proteins, and peptides with appended macrocycles will be briefly mentioned among the applications, as they represent useful models for the design of luminescent and MRI probes.

1.2 Chemistry of Ln ions in aqueous solution

The most stable oxidation state for Ln in aqueous solution is +3 (electronic configuration $[Xe]4f^n$, with n = 0–14 from La^{3+} to Lu^{3+}). Other oxidation states are also accessible for some Ln ions in aqueous solution, such as +2 for Eu and +4 for Ce, due to the enhanced stability associated with a half-filled 4f subshell ($[Xe]4f^7$ for Eu^{2+}) and with closed shell ($[Xe]4f^0$ for Ce^{4+}) configuration (Fig. 1A). Of note, in organic solvents, the entire

LCC-CNRS, Université de Toulouse, CNRS, Toulouse, France.
E-mail: enrico.falcone@lcc-toulouse.fr, emilie.mathieu@lcc-toulouse.fr
† These authors contributed equally to this work.

Open Access Article. Published on 22 September 2025. Downloaded on 4/1/2026 8:13:17 PM.
This article is licensed under a Creative Commons Attribution-NonCommercial 3.0 Unported Licence.

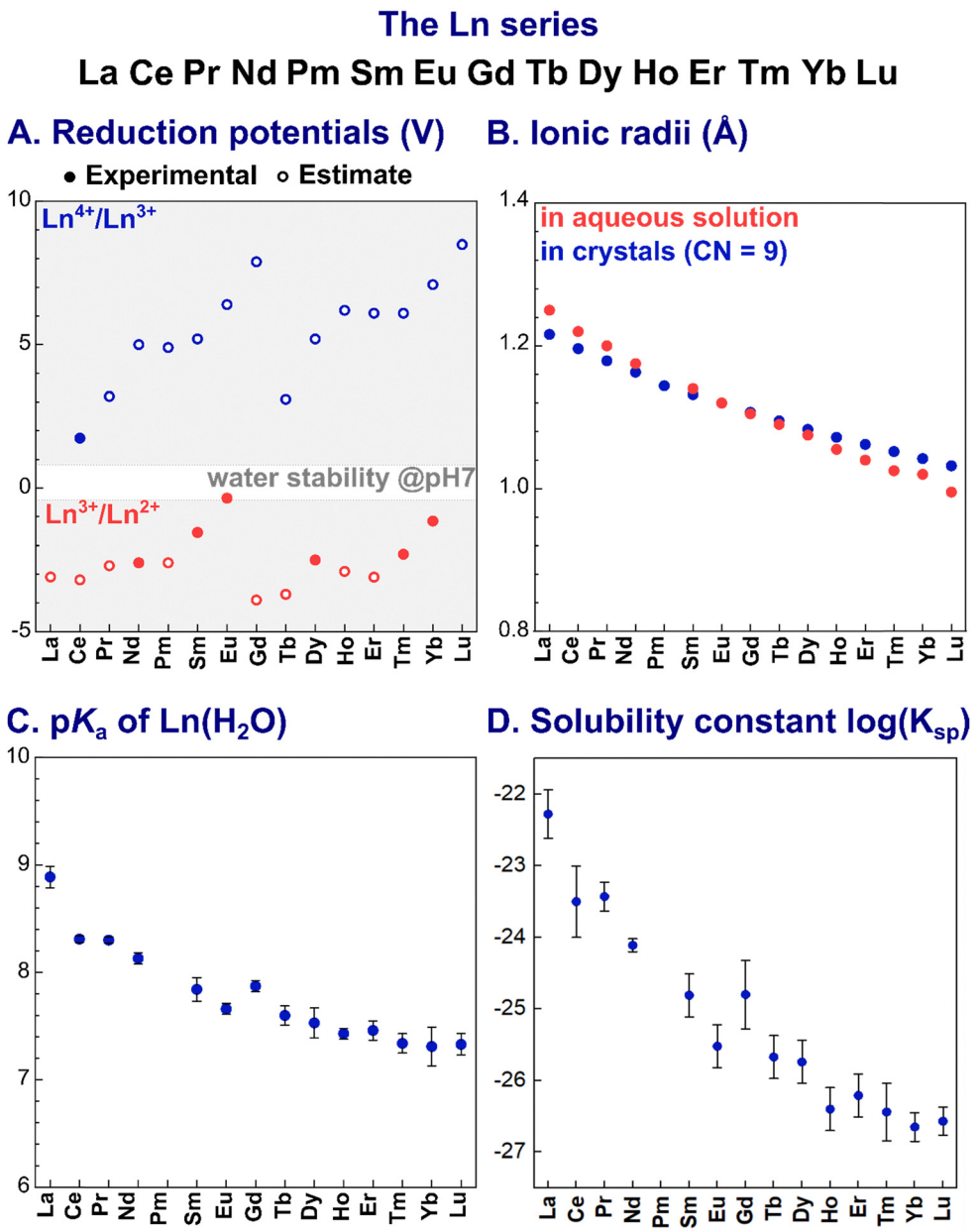

Fig. 1 Trends of key parameters along the Ln series: (A) reduction potentials;[26] (B) ionic radii in aqueous solution[27] and in crystals (CN = 9);[28] (C) acidity constants (pK_a) for Ln^{3+}-bound water molecule; and (D) solubility constants ($\log K_{sp}$).[29] The values plotted are reported in Table 14.

series of Ln (except for the radioactive Pm) could be stabilised in the +2 oxidation state, while for the +4 oxidation state only Ce^{4+}, Tb^{4+} and Pr^{4+} complexes were isolated.[24]

Ln^{3+} ions are hard Lewis acids. Their Lewis acidity slightly increases along the series as a consequence of the decrease of the ionic radius, known as lanthanide contraction (Fig. 1B). Noteworthy, Ln^{3+} ions have a similar size to Ca^{2+} (~1.0 Å), but are larger than d-block metal ions. As a consequence, Ln^{3+} have higher coordination numbers (CN) than d-block elements.

Due to their hard character, according to Pearson's HSAB principle,[25] Ln^{3+} ions prefer hard negatively charged ligands (*e.g.* carboxylate and phosphate). As a result of the core nature of the f orbitals, the nature of the Ln^{3+}–ligand bond is mainly ionic, and coordination geometries are hence mostly dictated by electrostatic and steric repulsions between the ligands.

In water, the larger Ln^{3+} ions (La^{3+}–Nd^{3+}) are coordinated by 9 water molecules and adopt a tri-capped trigonal prismatic coordination geometry, whereas smaller Ln^{3+} (Gd^{3+}–Lu^{3+}) are bound to 8 water molecules in a square-antiprismatic arrangement. For Pm^{3+} to Eu^{3+}, $[Ln(H_2O)_8]^{3+}$ and $[Ln(H_2O)_9]^{3+}$ are in equilibrium.[30]

Importantly, as Ln^{3+} aqua ions display Brønsted acidity in aqueous solution, Ln^{3+} speciation depends on the pH, with the acidity constant pK_a (eqn (1)) decreasing along the series

 This journal is © The Royal Society of Chemistry 2025

Open Access Article. Published on 22 September 2025. Downloaded on 4/1/2026 8:13:17 PM.
This article is licensed under a Creative Commons Attribution-NonCommercial 3.0 Unported Licence.

(Fig. 1C):

$$[Ln(H_2O)_n]^{3+} + H_2O \rightleftarrows [Ln(H_2O)_{n-1}(OH)]^{2+} + H_3O^+$$

$$K_a = \frac{[Ln(H_2O)_{n-1}(OH)][H_3O^+]}{[Ln(H_2O)_n]} \quad (1)$$

The stepwise deprotonation of bound water molecules leads to the formation of poorly soluble Ln^{3+} hydroxides, $Ln(OH)_3$. In particular, the solubility (expressed by the solubility product K_{sp}, eqn (2)) decreases along the Ln series (Fig. 1D).

$$Ln(OH)_3\ (s) \rightleftarrows Ln^{3+}(aq) + 3HO^-$$

$$K_{sp} = [Ln^{3+}][HO^-]^3 \quad (2)$$

In light of the trends described above, it appears that Ln^{3+} share some properties: they are all predominantly found in their +3 redox state and have similar Lewis acidities due to their similar ionic radii. At a more detailed level, Ln^{3+} display differences in their chemical properties: along the series, Ln^{3+} Lewis acidity increases, which can modulate their reactivity, the pK_a of the Ln^{3+}-bound water molecule decreases by approximately 2 units (Fig. 1C) and the solubility of $Ln(OH)_3$ drops from almost 5 order of magnitude (Fig. 1D); moreover Ln ions have different redox properties (Fig. 1A), which have been capitalized on for catalysis (see 6.4 Catalysis).

2. Scaffolds structure & Ln^{3+} coordination

2.1 Generalities

2.1.1 Type of scaffolds. The binding of Ln^{3+} ions to peptides and proteins has been accomplished either by using existing proteins with adequate coordination environment (*e.g.* 2.2 EF-hand peptides and proteins and 2.5.1 Naturally occurring proteins) or by the rational design of a Ln^{3+}-coordination site using natural and/or unnatural amino-acids (*e.g.* 2.3 Short peptides and 2.4 Peptide scaffolds of intermediate size). These scaffolds range from sequences of a few amino acids (AAs) to proteins, and can be divided into two main categories (Fig. 2): (i) those relying on an "EF-hand-like" motif for Ln-binding (2.2 EF-hand peptides and proteins); and (ii) other types of scaffolds.

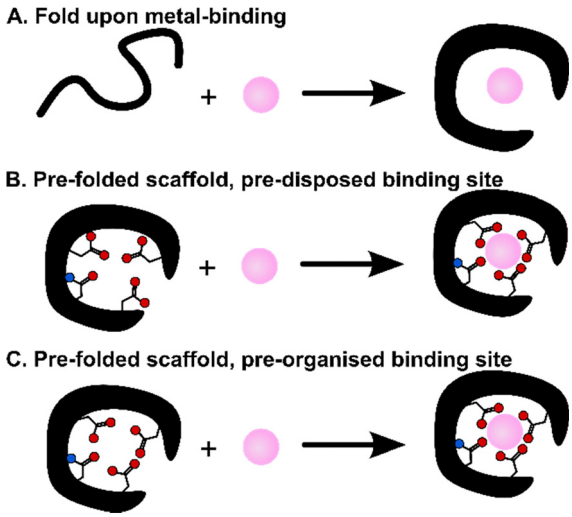

Fig. 3 Scaffolds that fold upon metal-binding (A), or are folded in the apo-form with a pre-disposed (B) or a pre-organized (C) binding site.

These scaffolds can be also differentiated based on their structure in the apo-form, *i.e.* in the absence of metal ions (Fig. 3). Whereas some are disordered in the apo-form and fold upon metal binding, others are pre-folded even in the absence of metal ions. In this latter case, the binding site can be (i) pre-disposed, *i.e.* the coordinating residues are placed at appropriate positions for metal-binding, or (ii) pre-organised, *i.e.* the coordinating residues are not only at an appropriate position but also with a good orientation that requires minimal reorganisation upon metal-binding.[31] To our knowledge, there is no example of a pre-organised metal binding site in Ln^{3+}-binding peptides and proteins, and hence, in the following, we will only describe unfolded scaffolds, or folded ones with a predisposed binding site. In order to discuss the scaffold structure and the Ln^{3+}-coordination, we grouped the scaffolds into four subcategories: (i) scaffolds relying on the well-described EF-hand motifs, which are found in short peptides such as lanthanide-binding tags (LBT), in helix-loop-helix (HLH) peptides, and naturally-occurring proteins such as calmodulin and lanmodulin; (ii) short sequences of ~10 amino acids; (iii) peptides of intermediate size, spanning from Ln fingers (LF) to coiled coils (CC); (iv) Ln^{3+}-binding proteins either naturally occurring or

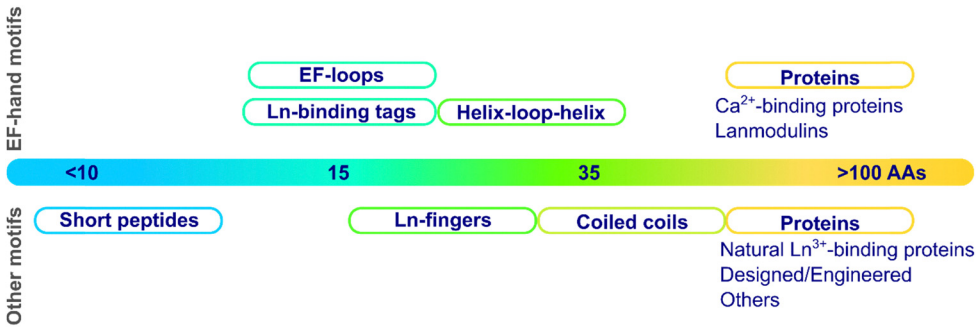

Fig. 2 Categories of scaffolds by size (number of amino acids).

Open Access Article. Published on 22 September 2025. Downloaded on 4/1/2026 8:13:17 PM.
This article is licensed under a Creative Commons Attribution-NonCommercial 3.0 Unported Licence.

engineered, in which the Ln^{3+} ion is not coordinated in an EF-hand motif.

2.1.2 Characterization of Ln^{3+} coordination sphere and scaffold stability. Several techniques give access to information on the Ln^{3+} coordination sphere and on the stability of the apo-peptide and Ln–peptides, which are shortly presented below.

Ln^{3+} coordination sphere. X-ray crystallography is the most accurate way to determine the Ln^{3+} coordination sphere, especially the CN and the mode of binding of certain amino acids (*e.g.* mono- or bi-dentate for carboxylates in Asp and Glu residues). However, it requires the formation of crystals, which are often difficult to obtain, in particular when working with peptides.

Nevertheless, information on the mono- or bi-dentate binding mode of carboxylates can also be obtained in solution through FT-IR measurements.[32,33] Moreover, the CN may be also investigated in solution through X-ray absorption spectroscopy, specifically EXAFS (extended X-ray absorption fine structure),[34–37] which has not been applied to Ln^{3+}-binding peptides and proteins so far.

In addition, insights into the Ln^{3+} coordination sphere can be gained by luminescence measurements. Eu^{3+}-hypersensitive transitions can report on the geometry of the coordination environment.[38] The hydration number q, which corresponds to the number of Ln^{3+}-bound water molecules, is also easily determined by measuring Ln^{3+} luminescence lifetimes (Ln = Eu^{3+}, Tb^{3+}, Yb^{3+}) for a given complex in H_2O and D_2O and using empirical relationships,[39,40] which have been established based on a library of complexes with q ranging from 0 to 6. This is the most solid method and should be favoured compared to other empirical equations that rely only on lifetimes measured in water. Importantly, when working with peptides and proteins it may be difficult to work in H_2O-free conditions. Instead, measurements can be performed for different $H_2O:D_2O$ ratios in order to extrapolate the value in 100% D_2O.[41]

Information beyond the number of Ln^{3+}-bound water molecules can be gained from NMR measurements, by taking advantage of the magnetic properties of lanthanides.[42–46] Comparison of spectra obtained with diamagnetic Ln^{3+} (La, Lu) and paramagnetic ones (all the other) can be used to identify residues in the first coordination sphere or further away from the Ln^{3+}-binding site. For well-folded scaffolds, paramagnetic Ln can even help to refine the protein solution structure. This has been accomplished either by incorporating Ln^{3+} in an intrinsic metal-binding site, such as in Ca^{2+}-binding proteins,[47,48] or by introducing Ln-binding tags (LBT, see Section 2.2.2) in the sequence of the targeted protein.[46]

Scaffolds stability. Information on scaffold stability can be gained from denaturation experiments, either using a temperature ramp or chemical denaturants, followed by circular dichroism. By comparison to a "native" scaffold, these measurements can inform on the impact of engineering a Ln^{3+}-binding site into the scaffold and the range of temperatures for which the peptide/protein is folded. It is also helpful to quantitatively assess the stabilisation induced by rational optimisations of the scaffold and by Ln^{3+} binding.

2.2 EF-hand motifs

EF-hand motifs represent the largest and best-known family of Ln^{3+}-binding sites in peptides/proteins. They are found in most Ca^{2+}-binding proteins, including calmodulin (CaM), parvalbumin and troponin C (TnC), and in a recently discovered selective Ln-binding protein, lanmodulin. The EF-hand consists of two α-helices (almost perpendicular to each other, a topology that reminds the spread thumb and forefinger of human hands) linked by a 12-residues loop, which is responsible for Ca^{2+} and Ln^{3+} binding through the amino acids in positions 1, 3, 5, 7, 9 and 12 (Fig. 4).[49–53] In the following paragraphs, EF-hand proteins and peptides are described starting from long-known Ca^{2+}-binding proteins (Section 2.2.1), which have inspired the design of optimized Ln^{3+}-binding peptides (see 2.2.2 LBTs and 2.2.3 HLHs), and finishing by a recently discovered family of Ln^{3+}-selective proteins (2.2.4 Lanmodulins).

2.2.1 Ca^{2+}-binding proteins. In most EF-hand proteins, Ca^{2+} is coordinated by 7 oxygen ligands with a pentagonal bipyramidal geometry: residues in positions 1, 3, and 5 serve as monodentate ligands, while the Glu_{12} residue binds always in a bidentate fashion (Fig. 4 and entry 1 in Table 1). The amino acid in position 7 (Thr in most natural scaffolds) binds instead with its backbone carbonyl. Finally, the 9th residue, which is most commonly (~30%) Asp, does not bind directly to the metal ion, but it forms a hydrogen bond with a water molecule that completes the coordination sphere.

Since Ln^{3+} ions have similar ionic radius to Ca^{2+}, the luminescent properties of some Ln^{3+} ions, mostly Tb^{3+} and Eu^{3+}, have been exploited to probe the metal binding sites in Ca^{2+}-binding proteins,[54–57] showing that the same coordination sphere with CN = 7 and q = 1 is observed for Ln^{3+} ions bound to Ca^{2+}–proteins such as TnC (Fig. 4 and entry 1 in Table 1).[52,58,59]

2.2.2 Lanthanide-binding tags (LBT). Following the seminal work of Szabo and coworkers,[66] the group of Imperiali has widely exploited the Ln^{3+}-binding ability of EF-hand loops found in Ca^{2+}-binding proteins to develop so-called lanthanide-binding tags (LBT) for various applications (see 6. Applications).[60,67–71]

LBTs are 15- to 20-residue-long peptides that were designed by elongating the core 12-residue EF-loop at both termini with apolar amino acids that stabilize the Ln^{3+}-bound conformation *via* hydrophobic interactions. The primary sequence of LBTs was optimized to feature high affinity for Tb^{3+} (see 3.2 EF-hand motifs),[72,73] and to control the hydration number for specific applications. For instance, LBT featuring a Ln^{3+}-bound water molecule (entries 2–4, in Table 1) were explored for applications as MRI contrast agents (see 6.2 MRI). The crystal structure of Gd^{3+} bound to a double LBT-ubiquitin fusion construct showed a CN = 7, which is as low as that observed in Ca^{2+}-binding proteins.[60]

As Ln^{3+}-bound water molecules quench its luminescence emission (see 6.1 Luminescent tags and probes), the

Open Access Article. Published on 22 September 2025. Downloaded on 4/1/2026 8:13:17 PM.
This article is licensed under a Creative Commons Attribution-NonCommercial 3.0 Unported Licence.

1	2	3	4	5	6	7	8	9	10	11	12
D/N	X	D/N	X	D/N	X	T	X	D/E	X	X	D/E

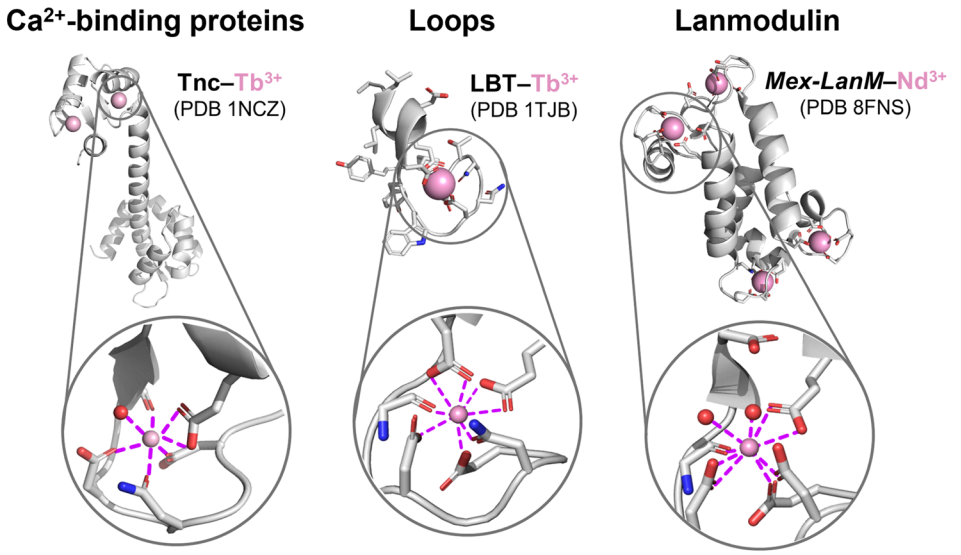

Fig. 4 EF-hand peptides and proteins. Top: EF-loop sequence showing the most common Ln^{3+}-binding amino acids (in bold and highlighted in pink) in each position. Bottom: Protein structures and Ln^{3+} coordination spheres in: left, troponin C (TnC) bound to two Tb^{3+} ions (PDB 1NCZ); middle, a lanthanide-binding tag (LBT) bound to Tb^{3+} (PDB 1TJB); right, *Mex*-LanM bound to four Nd^{3+} ions (PDB 8FNS). Figures were generated using Pymol.

coordination sphere was further optimized to afford efficient luminescent LBT by replacing the hydrogen-bonded Asp_9 with bidentate Glu_9. Thus, Tb^{3+}–LBT complexes with $q = 0$ and CN = 8 were obtained (Fig. 4 and entries 9–11 in Table 1).[64] Moreover, in order to sensitize Tb^{3+} emission a Trp residue serving as the antenna was introduced in the 7th position of the EF-hand motif (see 6.1 Luminescent tags and probes).[66,74]

2.2.3 Chimeric helix-loop-helix (HLH) motifs. The group of Franklin designed chimeric helix-loop-helix (HLH) motifs by engineering an EF-hand loop in a transcription factor helix-turn-helix DNA-binding domain, which were investigated as artificial nucleases (6.4 Catalysis) and DNA-responsive MRI probes (6.2. MRI).[16,75–80] The NMR solution structure of the La^{3+}–P3 complex revealed a coordination site similar to natural EF-hand loops. However, Asp_9 points away from the metal ion, leaving an open face that could easily accommodate two inner-sphere water molecules, which is in agreement with luminescence data recorded on the Eu^{3+}–P3 complex (entry 5 in Table 1).

2.2.4 Lanmodulins. In 2018, a novel family of EF-hand proteins, called lanmodulins (LanM), was discovered in Ln^{3+}-utilising bacteria.[81] Compared to previously known Ca^{2+}-binding proteins, LanM shows considerably higher selectivity for Ln^{3+} *vs.* Ca^{2+} (see 4. Selectivity). Recently, X-ray crystal structures of two LanM proteins from *M. extorquens* AM1 (*Mex*-LanM, Fig. 4) and *H. quercus* (*Hans*-LanM) were reported, thus facilitating a thorough comparison of their binding sites with those found in Ca^{2+}-binding proteins.[62] Of note, while CaM is folded in the apo-state and undergoes a conformational change upon metal-binding,[82] LanM is disordered and only upon binding four Ln^{3+} ions, it forms a compact three-helix bundle fold that is unique among EF-hand proteins.[83] The Ln^{3+} coordination spheres in LanMs feature higher CN (9 or 10) than Ln^{3+} bound to Ca^{2+}-binding loops and LBT (CN = 7–8). In *Mex*-LanM, this stems from a monodentate-to-bidentate switch of Asp_5 (entries 1 *vs.* 6 in Table 1) and the presence of an additional water molecule.

Compared to *Mex*-LanM, no Ln^{3+}-bound water molecules are found in *Hans*-LanM binding sites due to replacement of Asp_9 with Glu_9 (entries 6–8 *vs.* 12–14 in Table 1), as already observed for LBT (entries 9 *vs.* 2 in Table 1). In *Hans*-LanM, the increased CN relative to Ca^{2+}-binding proteins results from the presence of a bidentate Asp_3 (entries 12 and 14) rather than monodentate Asn_3 (entries 1, 9–11) and a monodentate-to-bidentate shift of Asp_5 (entries 12 and 14 *vs.* 9–11 in Table 1). Furthermore, a decrease in the CN is observed when La^{3+} is replaced by the smaller Dy^{3+} stemming from a bidentate-to-monodentate switch of Glu_9 (entries 12 *vs.* 14 in Table 1).[62]

2.3 Short peptides

2.3.1 Cyclic decapeptide (PA). Following the works of Franklin and Imperiali on the design of Ln^{3+}-binding peptides inspired by the Ca^{2+} coordination site in EF-hand motifs, Delangle and coworkers explored a different approach to improve the affinity of small peptides for Ln^{3+}. First, they selected a regioselectively addressable functionalized templates (RAFT) type of cyclic decapeptide (noted PA) in order to design a Ln^{3+}-binding site made of two Asp and two Glu residues (Fig. 5).[41] The

Open Access Article. Published on 22 September 2025. Downloaded on 4/1/2026 8:13:17 PM.
This article is licensed under a Creative Commons Attribution-NonCommercial 3.0 Unported Licence.

Table 1 Structural features of Ln^{3+} bound to EF-hand motifs. EF-loop patterns report the amino acids found in positions 1, 3, 5, 9 and 12 (note that the residue in position 7, not shown, always binds Ln^{3+} *via* a backbone carbonyl donor) and their binding mode (m = monodentate, b = bidentate, hb = hydrogen-bonded to a coordinating water molecule, nb = non-bound). Coordination (CN) and hydration (*q*) numbers are derived from X-ray crystal structures (for which PDB code is reported) or luminescence data obtained in solution using Tb^{3+} or Eu^{3+}

Entry	EF-loop pattern					*q*	CN	Ln^{3+}	EF-hand motifs	Peptide/Protein	PDB code	Ref.
	1	3	5	9	12							
1	D (m)	N (m)	D (m)	D (hb)	E (b)	1	7	Tb	**Ca^{2+}-protein**	TnC	1NCZ	58
2	D	N	D	D	E	1	n/a	Tb	**LBT**	m-sSE3		60
3	D (m)	D (nb)	D (b)	D (hb)	E (b)	1	7	Gd		xq-dSE3-ubiquitin	3VDZ	60
4	D	D	D	D	E	1	n/a	Tb		q-dSE3-ubiquitin		60
5	D	D	D	D	E	2	n/a	Eu	**HLH**	P3 (HLH)		61
6	D (m)	D (m)	D (b)	D (hb)	E (b)	2	9	Nd	**LanM**	*Mex*-LanM (EF1-3)	8FNS	62
7	D	D	D	D	E	2	n/a	Tb		*Mex*-LanM T41W		63
8	N (m)	D (b)	D (b)	D (hb)	E (b)	2	10	Nd		*Mex*-LanM (EF4)	8FNS	62
9	D (m)	N (m)	D (m)	E (b)	E (b)	0	8	Tb	**LBT**	LBT12	1TJB	64
10	D	N	D	E	E	0	n/a	Tb		sSE3		60
11	D (m)	N (m)	D (m)	E (b)	E (b)	0	8	Tb		ILB1β-S1	3LTQ	65
12	N (m)	D (b)	D (b)	E (b)	E (b)	0	10	La	**LanM**	*Hans*-LanM (EF1-3)	8DQ2	62
13	N	D	D	E	E	0	n/a	Eu				62
14	N (m)	D (b)	D (b)	E (m)	E (b)	0	9	Dy			8FNR	62

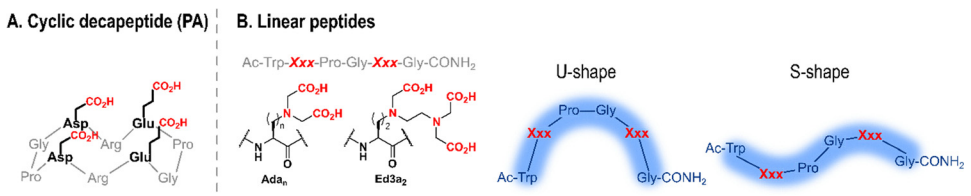

Fig. 5 Schematic structures of short cyclic (A) and linear (B) Ln-binding peptides. In (B) the structures of unnatural amino acids Xxx = Ada_n and $Ed3a_2$, and shapes adopted by linear peptides are shown. Adapted from ref. 8.

Open Access Article. Published on 22 September 2025. Downloaded on 4/1/2026 8:13:17 PM.
This article is licensed under a Creative Commons Attribution-NonCommercial 3.0 Unported Licence.

apo-peptide adopted an antiparallel β-sheet structure with a predisposed Ln-binding site at pH 3 with the side chains of the four coordinating residues on the same face of the cycle. Upon increasing the pH to 7, coulombic repulsions due to the deprotonation of the carboxylates led to an apparently disordered apo-peptide. Nevertheless, the addition of Ln^{3+} (La^{3+}, Tb^{3+}) compensated for this repulsion. The authors showed the presence of two water molecules in Tb^{3+} first coordination sphere (q = 2). By comparison with earlier work by Franklin[16,61,76] and Imperiali,[64] they proposed that the Ln^{3+} coordination sphere includes the four carboxylates (monodentate or bidentate) and two water molecules.

2.3.2 Linear peptides. Next, Delangle and coworkers investigated the use of unnatural amino acids in short linear hexapeptides for improving the affinity for Ln^{3+} (see 3. Thermodynamic stability). All the peptides have the sequence Ac–W–*X*–P–G–*X*–G–$CONH_2$, where *X* is either Ada_n with an aminodiacetate side chain (n = 1–3), or $Ed3a_2$ with an ethylenediamine triacetate side chain (Fig. 5), and Pro-Gly is a β-turn-inducer motif.[84–87] These peptides are disordered in the apo-form and fold upon metal binding. The speciation, coordination and solution structure of Ln–peptides were analysed in details and the authors showed that it was impacted by (i) side chain length; (ii) position of the Ln-binding residues in the sequence; and (iii) the type of residues (Ada_n or $Ed3a_2$, Table 2).

All the peptides formed 1 : 1 ligand : metal complexes below 1 equivalent of Ln^{3+} relative to the peptide, however, in the presence of more equivalents of Ln^{3+} the formation of multimetallic species was also observed (Table 2).

Changes in Ada_n side chain length impacted its coordination mode to Ln^{3+} (Table 2). Ada_2 and Ada_3 bind Ln^{3+} in a tridentate manner,[85] whereas Ada_1 is tri- or tetra-dentate depending on its position in the sequence (fifth or second, respectively).[84] The additional chelating group was proposed to be the backbone carbonyl of the Ada_1 main chain, which can form an additional chelate ring. This change of coordination mode impacted the number of water molecules in the first coordination sphere of Tb^{3+}, which dropped from 3 (P^{22}, P^{21} and P^{33}) to 1 and 0 in peptides where Ada_1 is tetradentate (P^{11} and P^{12}, respectively). It also impacted the structure of Ln^{3+}–peptide complexes in solution: in the presence of Ln^{3+}, P^{22} and P^{21} adopted a U-shape conformation, likely further stabilised by the formation of a type-II β-turn,[85] while coordination of Ada_1 backbone carbonyl to Ln^{3+} did not allow for the formation of a β-turn and resulted instead in an S-shape conformation of P^{11} and P^{12} (Fig. 5).[84]

Building upon this knowledge, Delangle and co-workers combined the pentadentate $Ed3a_2$ unnatural amino acid with Ada_2 either by placing $Ed3a_2$ in the second (P^{HD2}) or fifth (P^{HD5}) position in the sequence (Table 2).[87] Again, the speciation of the complexes depended on the position of the Ln^{3+}-binding amino acids in the sequence. For both peptides, the pentadentate $Ed3a_2$ excluded water molecules from the Tb^{3+} coordination sphere (q = 0).

More recently, short Ln^{3+}-binding peptides rich in Asp or Glu residues were reported. Veliscek-Carolan and co-workers studied peptides made of two to four Glu residues, either with an L- or D-stereochemistry, and coupled to a naphthalene antenna.[88] Simoni and co-workers studied the structure–affinity relationships of three Asp-rich pentapeptides (ADPDA, DPDPD, DGDGD) with actinide ions and Eu^{3+} and they predicted that the Eu^{3+} coordination sphere contained two carboxylates, one backbone carbonyl, and 4–5 water molecules.[89]

2.4 Peptide scaffolds of intermediate size

In the late 1980s, chemists began to dissect the complexity of proteins' fold and function, with the ultimate goal of being able to predict the primary sequence–structure–activity relationship.[90] This led to the development of *de novo* proteins, which refers to proteins designed from first principles. The design of α-helices was soon mastered, and the study of α-helical coiled coil made of the assembly of several α-helices has helped unravel design principles to obtain well-folded coiled coil assemblies. Since then, *de novo* proteins have been implemented with metal-binding site(s) and functions such as catalytic properties or electron transfer capacities.[91] Regarding Ln-binding peptides, a large amount of work has been dedicated to the design of Ln-binding coiled coils (2.4.1 Coiled coils),[92–102] and a seminal work described the design of Ln-fingers[103] (2.4.2 Ln fingers).

2.4.1 Coiled coils. The sequences of α-helices in coiled coils are constituted by a repetition of a heptad of amino acids (*abcdefg*) (Fig. 6 and 8).[93] Their assembly is driven by hydrophobic interactions of core amino acids in positions *a* and *d*. Residues in positions *e* and *g* are used to provide stabilizing electrostatic interactions, which also control the number of helices that assemble as well as their orientations (parallel or anti-parallel). Last, amino acids in position *f* are chosen for their propensity to induce α-helix folding, whereas those in positions *b* and *c* are used to improve solubility.

Three strategies were employed to insert an Ln^{3+}-binding site in such scaffolds: (i) in two-stranded coiled coils (2SCC,

Table 2 Linear peptides speciation, coordination mode, structure and hydration number. The peptides have the sequence Ac–W–*X*–P–G–*X*–G–$CONH_2$, where *X* is either Ada_n with an aminodiacetate side chain (n = 1–3) or $Ed3a_2$

Peptide	Speciation	Ln^{3+}-binding AAs	Coordination mode	Structure	q	Ref.
P^{11}	1 : 1 and multimetallic species	Ada_1	Tri- and tetra-dentate	S-shape	1	84
P^{22}	1 : 1	Ada_2	Tridentate	U-shape	3	85
P^{33}	1 : 1 and multimetallic species	Ada_3	Tridentate	n.d.	3	85
P^{12}	1 : 1	Ada_1 and Ada_2	Ada_1: tetradentate	S-shape	0	86
P^{21}	1 : 1 and multimetallic species	Ada_2 and Ada_1	Ada_1: tridentate	U-shape	3	86
P^{HD2}	1 : 1	Ada_2 and $Ed3a_2$	$Ed3a_2$: pentadentate	n.d.	0	87
P^{HD5}	1 : 1 and multimetallic species	$Ed3a_2$ and Ada_2	$Ed3a_2$: pentadentate	n.d.	0	87

Open Access Article. Published on 22 September 2025. Downloaded on 4/1/2026 8:13:17 PM.
This article is licensed under a Creative Commons Attribution-NonCommercial 3.0 Unported Licence.

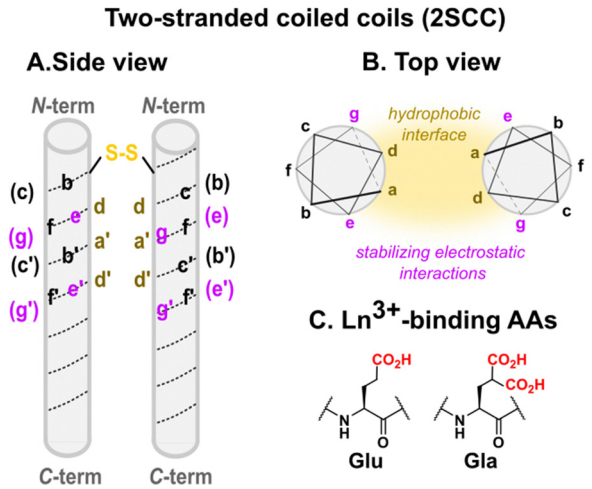

Fig. 6 Two-stranded coiled coils scaffolds designed by Hodges and coworkers: (A) side view, (B) top view, (C) Ln-binding sites are placed at the helical interface using Glu or Gla AAs in *e* and *g* positions. In (B) stabilising non-covalent interactions (hydrophobic, electrostatic) responsible for the folding and assembly of coiled coils are highlighted.

Fig. 6 and Table 3), positions *e* and *g* were used to introduce chelating moieties and place the Ln^{3+}-binding site at the helical interface; in three-stranded coiled coils (3SCC, Fig. 8), the binding site was (ii) either placed at the N-terminal (Table 4) or (iii) buried in the hydrophobic core by replacing core amino acids in position *a* and *d* by Ln^{3+}-binding residues (Table 5).

Two-stranded coiled coils (2SCC). Pioneering works on Ln^{3+}-binding 2SCCs were done by Hodges and coworkers.[94,95] They used as a starting point a *de novo* α-helical peptide made of the repetition of 5 heptads (35 amino acids, Table 3). The formation of a disulphide bridge ensured the obtention of a parallel 2SCC (Fig. 6). The native sequence was modified to include two (E_2) or three (E_3) Glu residues in *e* or *g* positions to form two Ln^{3+}-binding sites per coiled coil.[94] The stability of the apo-peptides in their oxidized form was quantitatively investigated by urea denaturation followed by circular dichroism (Fig. 7). The destabilisation induced by the mutation of Gln to Glu was the greatest for the $E_2(15,20)_{ox}$ construct, in which Glu in positions 15 and 20 generates the highest interchain repulsion. The introduction of a third Glu residue in the sequence (E_3(13,15,20) and E_3(15,20,22)) further destabilised the coiled coil.

A stabilising effect of La^{3+} on peptide unfolding was noted for E_2(15,20) and E_3 constructs, in which the Glu residues are well positioned to bind La^{3+} at the interhelical interface, the resulting interhelical bridges being responsible for the stability enhancement. The higher stabilisation measured for the E_3 sites may also indicate that the third Glu could participate in binding.

In addition, the authors evaluated the stability of the reduced peptides. These were less stable than their oxidised counterparts, highlighting the importance of the disulphide bridge for the stability of the scaffold. The addition of $LaCl_3$ resulted in an important stabilisation, which was attributed not only to La^{3+}-binding but also to a La^{3+}-driven dimerization. Hence, the most stable Ln^{3+}-binding constructs were achieved thanks to the presence of a disulphide bridge to form exclusively a 2SCC, and to Ln^{3+}-binding residues at the helical interface.

In a following work, Hodges and co-workers turned to γ-carboxyglutamic acid (Gla, Fig. 6), with two carboxylate functions, in order to (i) enhance the Ln^{3+}-affinity of the coiled coil thanks to the higher denticity of Gla *vs.* Glu, and (ii) design a system that folds upon metal-binding as the higher electrostatic

Table 3 Two-stranded coiled coil sequences designed by Hodges and coworkers

Name	Peptide sequence	Ref.
	g abcdefg abcdefg abcdefg abcdefg abcdef	
N	Ac-Q CGALQKQ VGALQKQ VGALQKQ VGALQKQ VGALQK-$CONH_2$	94
E_2(13,22)	Ac-Q CGALQKQ VGALEKQ VGALQKE VGALQKQ VGALQK-$CONH_2$	
E_2(20,22)	Ac-Q CGALQKQ VGALQKQ VGALEKE VGALQKQ VGALQK-$CONH_2$	
E_2(15,20)	Ac-Q CGALQKQ VGALQKE VGALEKQ VGALQKQ VGALQK-$CONH_2$	
E_3(13,15,20)	Ac-Q CGALQKQ VGALEKE VGALEKQ VGALQKQ VGALQK-$CONH_2$	
E_3(15,20,22)	Ac-Q CGALQKQ VGALQKE VGALEKE VGALQKQ VGALQK-$CONH_2$	
Gla_2(15,20)N	Ac-Q CGALQKQ VGALQKX VGALXKQ NGALQKQ VGALQK-$CONH_2$ X = Gla	95

Table 4 Three-stranded coiled coil sequences designed by Kashiwada and Ashkenazy

Name	Peptide sequence	Ref.
	efg abcdefg abcdefg abcdefg abcdefg	
Pep1	YGG EEK IAAIEKK IAAIEEK IAAIEKK IAAIEEK GGY	96
Pep3	YGG EEK IAAIEKK IAAAEEK XAAIEKK IAAIEEK GGY X = Gla	
	abcdefg abcdefg abcdefg abcdefg	
HPO-1	HPO-β-A IKQIEDK IEEILSK IYSIENE IARIKKL	97

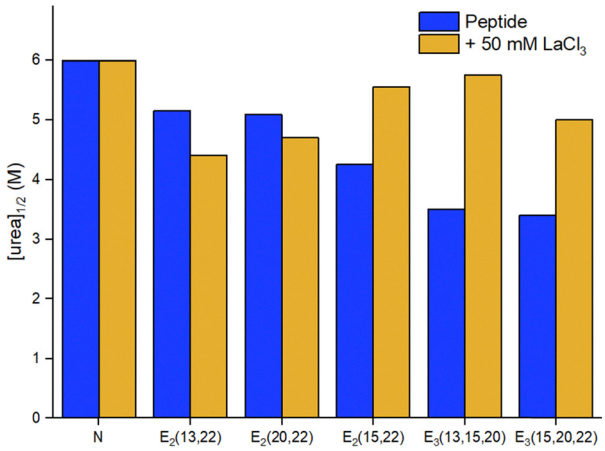

Fig. 7 Urea denaturation of 2SCC at pH 7 followed by circular dichroism.[94] Peptide sequences are given in Table 3. Experiments performed at 20 °C in 50 mM TRIS, 100 mM KCl, [pep] = 70–140 μM, without or with 50 mM $LaCl_3$. $[urea]_{1/2}$ corresponds to the concentration at which 50% of the peptide is unfolded.

Open Access Article. Published on 22 September 2025. Downloaded on 4/1/2026 8:13:17 PM.
This article is licensed under a Creative Commons Attribution-NonCommercial 3.0 Unported Licence.

repulsion induced by Gla was expected to lead an unfolded apo-peptide.[95] In order to further destabilise the apo-peptides, they mutated a Val residue (V) in position 23 by an Asn (N) (Table 3). The resulting peptide in its oxidised form, Gla_2(15,20)N, was fully unfolded at 20 °C pH 7. The peptide folded upon the addition of 0.5 mM $LaCl_3$, the amount of coiled coil formation increasing from ∼3 to 100% to match the one of the native Asn.

Three-stranded coiled coils (3SCC). A few years later, Kashiwada and coworkers used the same Gla residue for Ln^{3+}-binding, but inserted it in a three-stranded coiled coil (3SCC) scaffold.[96] In their design, the Gla residue was placed in an *a* layer of Pep1 (Table 4) so that the Ln^{3+}-binding site would be buried in the hydrophobic core rather than placed at the helical interface. Due to the insertion of the Gla residue in the sequences, the resulting peptide Pep3 was unfolded at 20 °C, pH 7. Circular dichroism experiments showed that the addition of 1 equivalent of Ln^{3+} (Ce^{3+}, Eu^{3+}, Tb^{3+}) per trimer drove the assembly and folding of the coiled coil.

Ashkenazy and coworkers investigated an alternative strategy, by placing the Ln^{3+}-binding site at the N-terminal of the 3SCC (Fig. 8 and Table 4), which has the advantage of not perturbing the folding and assembly of 3SCC.[97] They coupled a hydroxyphenol oxazoline moiety (HPO) to the peptide through a triazole linker. HPO acted both as a chelating moiety and as a sensitizing antenna.

The group of Peacock contributed to the design of Ln^{3+}-binding 3SCCs and provided a detailed understanding of the influence of Ln^{3+}-binding site position, Ln^{3+}-binding residues, second sphere effects, and scaffold size on Ln^{3+}-affinity, selectivity, and hydration number (Table 5).[98–102,104] They also reported the design of a heterobimetallic 3SCC bearing an Ln^{3+}-binding site and a Hg-binding site.[92]

The first peptide designed by the Peacock group, MB1-2, was a parallel 3SCC made of the repetition of 5 heptads and with an $(Asn)_3(Asp)_3$ metal binding site with Asn residues in a *d* layer, and Asp residues in the following *a* layer (Table 5).[98] The peptide also contains Trp residues to sensitize Tb^{3+} emission (see 6.1 Luminescent tags and probes).

The positioning of the Ln^{3+}-binding site within the hydrophobic core of the 3SCC destabilised the peptide, which was unfolded in the apo-state but assembled and folded upon Ln^{3+}-binding (Fig. 9). The hydrophobic environment and the adequate coordination sphere ($(Asn)_3(Asp)_3$) provided a suitable CN to the Ln^{3+} ion, preventing water from binding directly to the metal ion (q = 0).

Building on this work, the group of Peacock investigated how the position of the binding site in the 3SCC scaffold and the type of binding site ($(Asn)_3(Asp)_3$ *vs.* $(Asp)_3$) would impact Ln^{3+} coordination and hydration number.[99] With this aim, they extended the MB1 series containing an $(Asn)_3(Asp)_3$ binding site with peptides MB1-1, MB1-3 and MB1-4, and designed the CS1 series containing an $(Asp)_3$ binding site with peptides CS1-1, CS1-2 and CS1-4 (Table 5). In the MB1 series, the position of the metal-binding site impacted differently the stability of the apo-peptides (Fig. 9). Whereas positioning the metal-binding

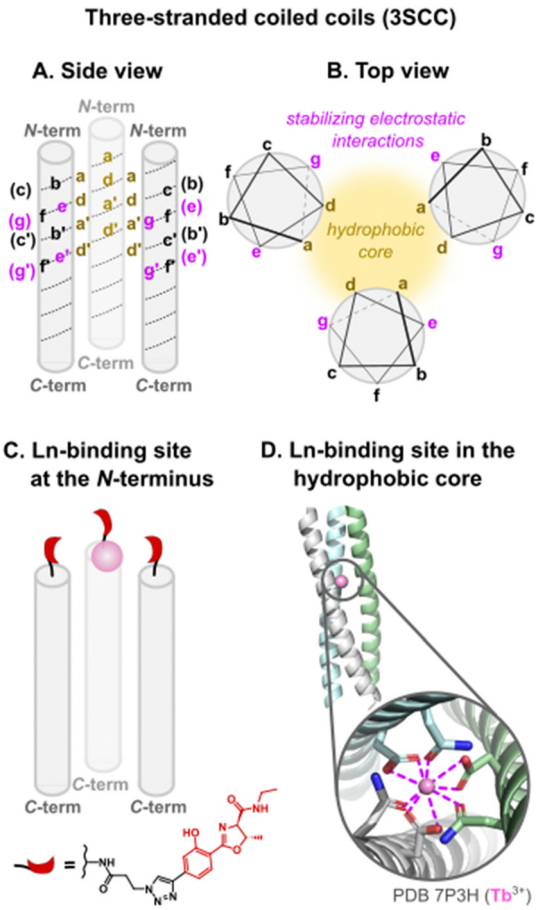

Fig. 8 Three-stranded coiled coils scaffolds: (A) side view, (B) top view, (C) Ln-binding site placed at the N-terminal with a hydroxyphenol oxazoline (HPO) ligand, (D) Ln-binding site in the hydrophobic core (*a* and *d* positions). In (B) stabilising non-covalent interactions responsible for the folding and assembly of coiled coils are highlighted.

Table 5 Three-stranded coiled coil sequences designed by Peacock and coworkers

Name	Peptide sequence	q	Ref.
	abcdefg abcdefg abcdefg abcdefg abcdefg	3	99,100
MB1-1	Ac-G IAANEWK DAAIEQK IAAIEQK IAAIEQK IAAIEQK G-$CONH_2$		
MB1-2	Ac-G IAAIEQK IAANEWK DAAIEQK IAAIEQK IAAIEQK G-$CONH_2$	0	98,99
MB1-3	Ac-G IAAIEQK IAAIEQK IAANEWK DAAIEQK IAAIEQK G-$CONH_2$	0	99
MB1-4	Ac-G IAAIEQK IAAIEQK IAAIEQK IAANEWK DAAIEQK G-$CONH_2$	2	99
MB1-1(2*A*)	Ac-G AAANEWK DAAIEQK IAAIEQK IAAIEQK IAAIEQK G-$CONH_2$	3	100
MB1-1(2*F*)	Ac-G FAANEWK DAAIEQK IAAIEQK IAAIEQK IAAIEQK G-$CONH_2$	2	
MB1-1(2*W*)	Ac-G WAANEWK DAAIEQK IAAIEQK IAAIEQK IAAIEQK G-$CONH_2$	0	
MB1-1(2*Y*)	Ac-G YAANEWK DAAIEQK IAAIEQK IAAIEQK IAAIEQK G-$CONH_2$	1	
MB1-4(37W)	Ac-G IAAIEQK IAAIEQK IAAIEQK IAANEQK DAAIEQK WG-$CONH_2$	0	
MB1-1S	Ac-G IAANEWK DAAIEQK IAAIEQK IAAIEQK G-$CONH_2$	nd	102
MB1-1L	Ac-G IAANEWK DAAIEQK IAAIEQK IAAIEQK IAAIEQK IAAIEQK G-$CONH_2$	4	
CS1-1	Ac-G IAAIEWK DAAIEQK IAAIEQK IAAIEQK IAAIEQK G-$CONH_2$	4	99
CS1-2	Ac-G IAAIEQK IAAIEWK DAAIEQK IAAIEQK IAAIEQK G-$CONH_2$	nd	
CS1-4	Ac-G IAAIEQK IAAIEQK IAAIEQK IAAIEWK DAAIEQK G-$CONH_2$	nd	
HC02	Ac-E WEAIEKK IAANESK DQAIEKK IQAIEKK IEAIEHG-$CONH_2$	0	101

Open Access Article. Published on 22 September 2025. Downloaded on 4/1/2026 8:13:17 PM.
This article is licensed under a Creative Commons Attribution-NonCommercial 3.0 Unported Licence.

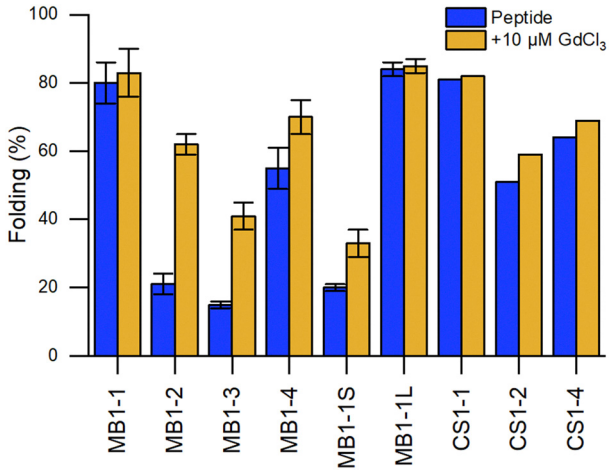

Fig. 9 Comparison of the percentage of folding of 3SCC.[99,102] Peptide sequences are given in Table 5. Experiments were performed in 5 mM HEPES, pH 7, 293 K, [pep] = 30 μM, without or with 10 μM $GdCl_3$. The percentage folding was calculated based on: $\%_{folded} = \frac{[\theta]_{222nm} - [\theta]_{coil}}{[\theta]_{max} - [\theta]_{coil}} \times 100$, with $[\theta]_{222nm}$ the molar ellipticity at 222 nm, $[\theta]_{coil}$ the molar ellipticity for a random coil, and $[\theta]_{max} = -42\,500 \times \left(1 - \left(\frac{3}{n}\right)\right)$ the theoretical maximum molar ellipticity, where n is the number of residues in the sequence.[105]

site in the middle of the scaffold destabilized the apo-peptides (21% and 15% folded for MB1-2 and MB1-3, respectively), positioning at the C-terminal was better tolerated (55% folded), and when placed close to the N-terminal the apo-peptide seemed almost unaffected (80% folded). For the CS1 series, in which there is no top $(Asn)_3$ layer, the apo-peptides were always more stable than their MB1 analogues (Fig. 9). As was previously observed for MB1-2,[98] Gd^{3+} stabilised the 3SCC assembly and led to the formation of 1 : 3 Ln^{3+} : peptide complex. However, the authors noted that for CS1-2 and CS1-4, there was only a small improvement of folding upon Tb^{3+}-binding compared to their MB analogues (Fig. 9), and only a small increase in Tb^{3+}-emission which suggested that these peptides may bind Tb^{3+} through non-specific interactions.

Depending on the position of the binding site, the number of Tb^{3+}-bound water molecules varied from 4 (CS1-1) and 3 (MB1-1) for the more solvent-exposed sites at the N-terminal, to 2 (MB1-4) for the site at the C-terminal, to 0 (MB1-2 and MB1-3) for sites more buried into the scaffold (Table 5). These results demonstrated that it is possible to control the number of Ln^{3+}-bound water molecules by controlling the position of the metal binding site in the 3SCC. The more solvent-exposed sites at the N- and C-termini had the higher hydration number, which suggested a change in Asp coordination mode (monodentate *vs.* bidentate) or that not all Asp and Asn were involved in Ln^{3+}-coordination. On the other hand, the sites that were more buried within the hydrophobic core of the 3SCC were shielded from the solvent. This is consistent with the $(Asn)_3(Asp)_3$ site fulfilling the preference of Ln^{3+} for a high coordination number. The recent publication of the crystal structure of HC02 (PDB 7P3H), a 3SCC similar to MB1-2, confirmed that Tb^{3+} is nona-coordinated by three Asn (monodentate) and three Asp (bidentate) as shown in Fig. 8.[101]

In later works, Peacock and coworkers investigated both the effect of the peptide length on the overall stability of the assembly[102] and of second-sphere effects on the hydration number (Table 5).[100] Whereas the shorter MB1-1S was too destabilised to bind $GdCl_3$, there was no marked difference in peptide folding or hydration number between MB1-1 and the longer MB1-1L (Fig. 9), and only a qualitative enhancement of stability for MB1-1L compared to MB1-1. One explanation proposed was that the binding site is too far (4–5 nm) from the sixth heptad to detect any positive effect on folding, Ln^{3+} affinity and hydration number.

In order to investigate 2nd sphere effects on the hydration number, core Ile (I) residues placed in the *a* layer above the metal-binding site of MB1-1 were mutated to Ala (A), Phe (F), Tyr (Y) or Trp (W) (MB1-1(2*X*) series, Table 5). Tuning of the steric hindrance provided control of the hydration number of Tb^{3+} that varied from q = 3 (MB1-1, MB1-1(2A)), to 2 (MB1-1(2F)), to 1 (MB1-1(2Y)), to 0 (MB1-1(2W)). This strategy was also successfully applied at the C-terminal for MB1-4 site, which was mutated to MB1-4(37W) in order to shield Tb^{3+} from the solvent, which decreased the hydration number from 2 to 0.

The results obtained by Peacock and coworkers highlight that with the same set of coordinating AAs, the number of Ln^{3+}-bound water molecules can be controlled either by controlling the position of the Ln^{3+}-binding site within the scaffold or by tuning second sphere residues thanks to steric effects. The replacement of core amino acids by Ln^{3+}-binding residues resulted in the destabilisation of peptide folding and assembly that depended on the position of the site within the scaffold and could be in part compensated for by Ln^{3+}-binding.

2.4.2 Ln fingers. A seminal work by Zondlo and coworkers described the rational design of lanthanide fingers (LF, Fig. 10 and Table 6).[103] Their goal was to obtain a peptide that adopts the same fold as the naturally occurring zinc fingers, whose structure is constituted of an α-helix placed above a β-hairpin.

The $(His)_2(Cys)_2$ Zn^{2+}-binding site of Zn-fingers was replaced by an $(Asp)_2(Glu)_2$ binding site, more suited for Ln^{3+}-binding. The LF scaffold was redesigned to favour the formation of secondary structures, leading to LF1. Modifications included notably the use of α-helix or β-sheet inducer amino acids and of

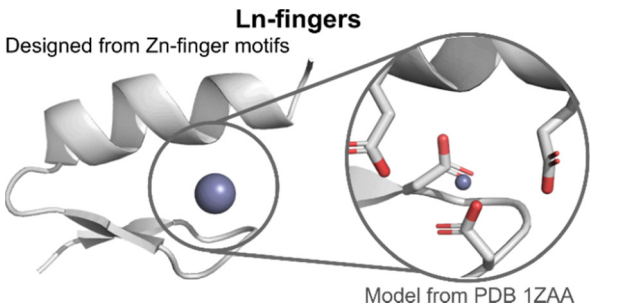

Fig. 10 Lanthanide fingers. A model of the hypothetic structure and binding site of Ln-fingers was generated from a closely related zinc finger structure (PDB 1ZAA) using Pymol. Zn is represented as a grey sphere.

Open Access Article. Published on 22 September 2025. Downloaded on 4/1/2026 8:13:17 PM.
This article is licensed under a Creative Commons Attribution-NonCommercial 3.0 Unported Licence.

Table 6 Ln fingers sequences designed by Zondlo and coworkers. ^{D}P = D-proline

Name	Peptide sequence
	β-hairpin α-helix
LF1	AYTD^{D}PSDTKTFSQSSALAKELKAEAG
LF2	AYTD^{D}PSDTKTFS**TPEQ**LAKELKAEAG
LF3	AYTD^{D}PSDTKTFSTPEQLAKEL**LQEHGI**
LF4	AYTD^{D}PSD__TFSTPEQLAKELLQEHGI
LF5	AYTD **TI**D__TFSTPEQLAKELLQEHGI
LF6	AYTD TID__T**W**STPEQLAKELLQEHGI
LF7	AYTD^{D}PS**N**__TFSTPEQLAKELLQEHGI

a type II′ β-turn (^{D}Pro-Ser) to favour the formation of the β-hairpin. The addition of an N-cap (LF2) and a C-cap (LF3), which are motifs favouring the formation of α-helices,[106–108] improved the folding. The extent of stabilisation of peptides fold following these modifications was qualitatively assessed by comparing CD spectra obtained for apo-peptides. The influence of the size of the binding site on Ln^{3+}-binding was investigated by opening up the site thanks to the deletion of two AAs in the sequence (LF4), as well as the type of Ln^{3+}-coordinating residues (LF7). Genetically encodable LFs were designed by replacing the type II′ β-turn (^{D}Pro-Ser) with Thr-Ile (LF5 and LF6).

A detailed NMR analysis of LF4 without and with Lu^{3+} showed rearrangements throughout the peptide upon Lu^{3+}-binding, which suggested that, as for Zn-fingers, Ln-fingers fold upon metal binding. For all the sequences, Ln^{3+} binding improved the folding of the peptides and the data obtained were consistent with a 1:1 peptide:Ln^{3+} ratio. Hydration numbers were not determined, but H_2O molecules are likely to participate in Ln^{3+} coordination sphere in addition to the Ln^{3+}-binding AAs.

2.5 Other Ln-binding protein scaffolds

2.5.1 Naturally occurring proteins

Ln-ADH. The discovery of Ln-utilizing bacteria has sparked a great interest in the identification of the lanthanome.[9–12] The first Ln-binding protein discovered in the 2010s was an enzyme: a pyrroloquinoline quinone (PQQ)-dependent methanol dehydrogenases (MDH) encoded by the gene *xoxF*, whose active site also contains an Ln^{3+} taking part in the catalysis.[4–7] A characteristic of this enzyme is that it is directly involved in the metabolism of the organisms that produce it, mostly methylotrophic bacteria, which are hence the sole organisms known so far for which Ln^{3+} can be essential elements.[9] Following this discovery, several Ln-MDH were isolated and their crystal structures were reported with either La^{3+},[109,110] Ce^{3+},[7] Nd^{3+},[111] or Eu^{3+}[112] in the active site (Fig. 11). In addition, the family of Ln-dependent enzymes was extended to ethanol dehydrogenases (EDH) following the identification of ExaF[113] and PedH[114] in methylotrophs and non-methylotrophs.[115] The crystal structure obtained for a Pr^{3+}-EDH showed that the active site of this enzyme shared a lot of similarities with the one of Ln-MDH, including conserved residues involved in Ln^{3+}- and PQQ-binding.[116] Due to these similarities, Ln-MDH and Ln-EDH are often grouped under the term Ln-alcohol dehydrogenases (Ln-ADH).

The active site of Ln-ADH is closely related to other PQQ-dependent alcohol dehydrogenases, whose active site contains a Ca^{2+} ion, but which are encoded by different genes (*mxaF* for Ca-MDH, *exaA* and *pedE* for Ca-EDH).[9] The main difference between the active sites of Ca- and Ln-ADH is the presence of an additional Asp residue in the Ln^{3+} coordination sphere. Crystal structures showed that in Ln-ADH, the Ln^{3+} ion is nona-coordinated by two Asp (one monodentate, one bidentate), a Glu (bidentate), an Asn (monodentate), and the PQQ cofactor (tridentate), as shown in Fig. 11. For some structures, an additional ligand (PEG,[7] MeOH[111]) is also found coordinated to the Ln^{3+}, which suggests that there is a free site for substrate coordination to the metal ion, giving a total coordination number of 10.

It is not clear how the mature Ln-ADHs are formed, especially how they acquire their two cofactors, PQQ and Ln^{3+}, and how these impact the stability of the scaffold. Based on the obtention of crystal structures with only Ln^{3+} (and not PQQ) in the active site,[110,111] it has been proposed that Ln^{3+} could be loaded independently of PQQ. However, it is also possible that PQQ leaks out of the enzyme pocket during the crystallization

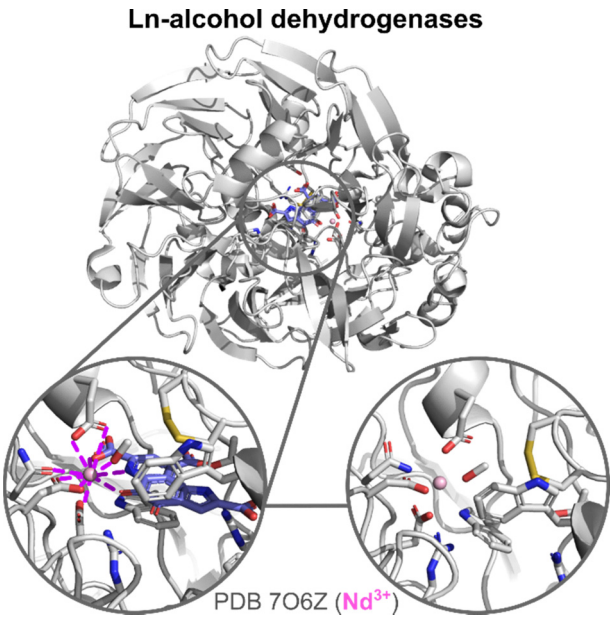

Fig. 11 Ln-ADH structure and active site. Zoom on the active site and Ln-coordination sphere of crystals obtained with the PQQ cofactor (blue) in the active site (left) and without it (right). In addition to Ln-binding AAs and PQQ, a methanol molecule is also bound to Nd^{3+}.

Open Access Article. Published on 22 September 2025. Downloaded on 4/1/2026 8:13:17 PM.
This article is licensed under a Creative Commons Attribution-NonCommercial 3.0 Unported Licence.

steps. The comparison of the holo-MDH (with Ln and PQQ) and Ln-only-MDH (no PQQ) shows nearly identical structures (Fig. 11).[110,111] Ln is coordinated by the same residues in both cases. Residues in interaction with PQQ show minimal rearrangement in the holo-MDH relative to the Ln-only MDH, which suggests that the MDH active site may be predisposed for PQQ binding.

On the other hand, ADH enzymes can also be obtained with PQQ-only in their active site. Indeed, several papers report on the purification of Ln-ADH with 0.4 to 1 equivalent of Ln per protein.[6,7,109–113,117,118] Moreover, Daumann and coworkers demonstrated that upon incubation of partially metallated MDH with Ln^{3+} the activity of the enzyme could be improved, which suggests the *in situ* reconstitution of a functional enzyme in which PQQ was already present.[112,119] Martinez-Gomez and coworkers also observed the partial metallation of a Nd-MDH, without change in the PQQ content of the enzyme.[117] However, with their conditions, the reconstitution of a holo-enzyme by incubation with Nd^{3+} was unsuccessful.

Working on a parent enzyme, the PQQ- and Ca^{2+}-dependent soluble glucose dehydrogenase (sGDH), Stines-Chaumeil, Limoges and coworkers demonstrated that reconstitution of the holo-enzyme could follow either a path where PQQ is added first to the active site or one where Ca^{2+} is bound first.[120] Their results evidenced that the kinetic of reconstitution depended on the order of addition of the two cofactors. The reconstitution was fast when the protein was metallated with Ca^{2+} before the binding of PQQ, and slow if PQQ binding happened first. Although little is known about the mechanism and kinetics of Ln-ADH reconstitution, the two reconstitution paths proposed for sGDH could also be considered for Ln-ADH.

The data on Ln-ADH stability are scarce. Some data show that Ln-MDHs are sensitive to temperature and denature at temperatures higher than 50 °C.[111,112] However, the exact value at which denaturation occurs may be influenced, among other factors, by the organism Ln-MDH is purified from, as the enzyme obtained from the extremophile *M. fumariolicum* SolV has an optimum temperature for catalytic activity at 60 °C.[7] In addition, the thermal stability of Ln-MDH could be Ln-sensitive, as suggested by Nakagawa and coworkers who compared the thermal stability of a La- and a Nd-MDH and found that the latter denatured at lower temperatures although it is not clear what could cause such a difference.[118]

Lanpepsy (LanP). Following the discovery of ADH, other Ln^{3+}-binding proteins were identified: lanmodulins (LanM, see above), lanpepsy (LanP), and landiscernin (LanD also referred to as LutD, see below).[121] LanP is composed of two PepSY domain.[122] Studies on deletion strains suggested that LanP function is not directly linked to Ln^{3+} sensing or uptake. The 3D structure predicted by AlphaFold suggested that the folded protein forms a cavity with several negatively charged residues. Competitive titration experiments determined that LanP could bind up to 3–4 Ln^{3+} ions, which was confirmed by ICP-MS, although a higher number of sites was determined by ITC titration (~6). The exact binding sites and coordination environments of Ln^{3+} in LanP still need to be uncovered.

Landiscernin (LanD). A role for LanD in the acquisition of Ln^{3+} ions was first suggested in 2019.[123,124] Following these preliminary works, the protein was isolated and crystallized by Cotruvo and coworkers.[125] It forms a three-helix bundle stabilised by a disulphide bridge and hydrophobic interactions at its core. Several negatively charged residues are found at its surface, close to the N-terminal. Crystal structures obtained with 0.5 equivalents of Ln^{3+} (La, Ce, Eu, and Ho) per protein showed the formation of a Ln^{3+}-binding site at the interface between two proteins made of three Glu residues from each protein (Glu70, Glu73, Glu75), which except for this coordination site do not interact with each other (Fig. 12). Interestingly, as the Ln^{3+} ionic radius decreases, the coordination number decreases from 9 (La^{3+}, Ce^{3+}) to 8 (Eu^{3+}, Ho^{3+}), due to the loss of a Ln^{3+}-bound water molecule for the latter (Fig. 12).

In solution, the protein was shown to be monomeric in the apo-state with a dissociation constant for the dimer of K_{dimer} = 610 μM but was differently influenced by metal ions. Whereas La^{3+}, Ce^{3+} and Nd^{3+} seemed to favour the dimerization of the protein (K_{dimer} = 117, 200 and 253 μM, respectively), this was not the case with Eu^{3+} and Ho^{3+} (K_{dimer} = 1400 and 700 μM, respectively). Based on the crystal structures obtained, the authors proposed that as the ionic radius of the metal ion decreases, electrostatic repulsions due to the presence of

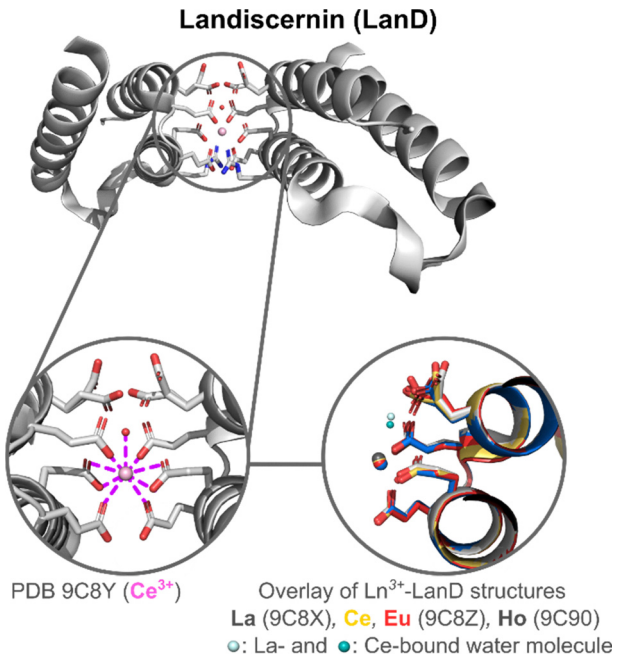

Fig. 12 Landiscernin (LanD) structure and active site. Zoom on the Ln^{3+} coordination sphere (left). Overlay of Ln^{3+}–LanD structures (Ln^{3+} = La, Ce, Eu, Ho) was generated with Pymol (right). A Ln^{3+}-bound water molecule is only present in the structure of La^{3+}–LanD and Ce^{3+}–LanD. Two glutamate residues adopt different orientations in the crystal structures and their rotamers are represented. They do not participate in Ln^{3+}-binding but are important for dimer formation.

Open Access Article. Published on 22 September 2025. Downloaded on 4/1/2026 8:13:17 PM.
This article is licensed under a Creative Commons Attribution-NonCommercial 3.0 Unported Licence.

negative charges on the surface of the proteins increase and disfavour the dimerization.

2.5.2 Proteins designed/engineered for Ln-binding

PqqT. The discovery of Ln-utilising bacteria has also inspired the field of artificial enzyme design, with two lead examples recently published. Olshansky and coworkers aimed at designing a Ln-ADH mimic, which could serve as a model to study the mechanism of the enzymes.[20] Analysis of the X-ray structure of PqqT, a PQQ-binding protein, showed that several residues near PQQ may be predisposed for Ln-binding, including Glu_{111}, Asp_{141} and Asn_{143} (Fig. 13). In addition, a lysine (Lys_{142}) interacts through electrostatic interactions with PQQ with its side chain positioned in the PQQ pocket where Ln^{3+} binds. Mutation of Lys_{142} (K_{142}) to an Asp afforded the mutant PqqT–K_{142}D that binds 1 PQQ (model structure in Fig. 13) and 1 Ln^{3+} ion. In the engineered active site, PQQ was required for the binding of La^{3+} and hence participated in its coordination sphere. In addition to Asp_{142}, other residues (Glu_{111}, Asp_{141}, Asn_{143}) may also participate in Ln-binding, which still needs to be confirmed. The mutant containing La^{3+} and PQQ, noted La^{3+}–PQQ⊂PqqT–K_{142}D, was able to oxidize benzyl alcohol under aqueous conditions (see 6.4 Catalysis).

TIM barrel. The second example of an Ln artificial enzyme came from Zeymer and coworkers. Starting from a computationally designed *de novo* TIM barrel scaffold,[126] they aimed to design an enzyme for Ce^{4+} photoredox catalysis (see 6.4 Catalysis).[19]

The initial scaffold was designed by combining a TIM domain made of eight parallel β-strands surrounded by eight α-helices, and a ferredoxin (FD) insert domain, either with a $(His)_2(Glu)_2$ or with a $(Glu)_4$ binding site.[126] The stability of the scaffolds with these two binding sites was assessed by thermal and chemical denaturation. The two scaffolds showed a high stability with temperature (T_m > 95 °C), and unfolded in two steps with increasing concentration of guanidinium chloride, each event corresponding to the unfolding of one domain (TIM and FD). X-ray structure of the apo-protein scaffold showed a pre-disposed $(Glu)_4$ binding site. The hydration number of Tb^{3+} was determined using a third mutant with a Trp for Tb^{3+} sensitisation. In this mutant, Tb^{3+} was bound by one water molecule. X-ray structure showed a CN = 9 for Tb^{3+}, with the four Glu acting as bidentate ligands (Fig. 14).

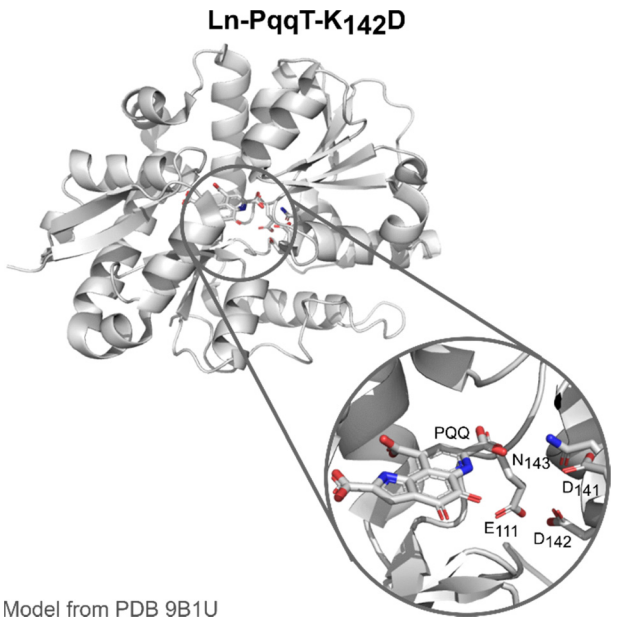

Fig. 13 Ln–PqqT–K_{142}D mutant bound to PQQ and its possible Ln^{3+}-binding site (zoom). Model structure was generated from the crystallographic structure of PQQ-bound PqqT (PDB 9B1U) using the mutagenesis tool in PyMOL.

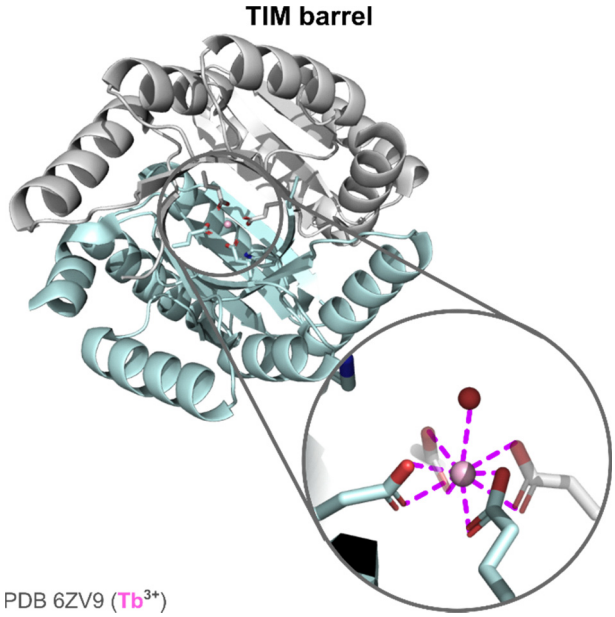

Fig. 14 TIM barrel structure and active site. Zoom on Ln-coordination sphere showing the presence of a Ln^{3+}-bound water molecule.

2.5.3 Ln-binding to other metalloproteins for specific applications. Investigation of Ln-binding was also conducted with other metalloproteins (RTX, PTE-R18) to exploit these scaffolds for specific applications.

RTX. RTX corresponds to the block V of the repeats-in-toxins (RTX) domain of adenylate cyclase.[127–129] It is a Ca^{2+}-binding protein that can bind up to eight Ca^{2+} ions. In the apo-state, the protein is intrinsically disordered and folds upon metal binding. The folded protein adopts a parallel β-helix structure. Ca^{2+}-binding sites are located between turns of successive layers and are composed of one Asp residue and other donor atoms from the main chain to provide CN = 7. Recently, the capacity of RTX to bind Ln^{3+} was investigated more thoroughly for potential applications in Ln^{3+} recycling (see 6.3 Ln recovery and separation).[129] Circular dichroism experiments demonstrated that Ln^{3+} induced the folding of the protein. However, it also suggested that the protein might adopt a different structure relative to the Ca^{2+}-induced folding, and the exact Ln-coordination sphere in this protein is still unknown.

PTE-R18. PTE-R18 is a mutant from a Zn^{2+}-dependent phosphotriesterase enzyme (PTE) designed for the hydrolysis of

Open Access Article. Published on 22 September 2025. Downloaded on 4/1/2026 8:13:17 PM.
This article is licensed under a Creative Commons Attribution-NonCommercial 3.0 Unported Licence.

2-naphthyl hexanoate. Jackson and coworkers investigated the use of this scaffold for Ln^{3+}-binding to design an Ln–enzyme and exploit the Lewis acid properties of Ln^{3+} (see Catalysis).[21] Crystal structures obtained by co-incubation of the apo-protein and Ln^{3+} (Eu, Gd) showed the positioning of the Ln^{3+} ion in the Zn^{2+}-binding site coordinated by two His, one Asp (bidentate), a water molecule and a chloride ion (CN = 6). This low CN is surprising given the preference of Ln^{3+} for a higher coordination number, and could explain the low occupancy ($\sim$20%) of the metal-site by Ln^{3+}.

2.6 Discussion and guidelines

A large variety of scaffolds were reported for Ln^{3+}-binding, which range from peptide sequences of a few AAs to proteins, that either fold upon metal-binding or that are pre-folded. For unfolded scaffolds or pre-folded scaffolds of intermediate size, additional stabilising interactions beyond the binding site are required to obtain a stable assembly, which in turn may improve Ln affinity (see Thermodynamic stability). In particular, the design of pre-folded scaffolds with a predisposed Ln^{3+}-binding site using short or intermediate-size peptides requires finding a balance between the stability of the structure, which relies mostly on hydrophobic interactions, and the introduction of metal-binding residues that can destabilise the scaffold. With this aim, two strategies were employed, sometimes in combination: (i) to put the metal binding site at a position that ensures a minimal perturbation of the scaffold (*e.g.* on the surface *vs.* inside the hydrophobic core of coiled coils, or at different positions within the hydrophobic core of coiled coils); (ii) to select amino acids known for their propensity to favour the formation of specific secondary structures. Overall, only a few studies investigated in detail the stability of their constructs and the impact of Ln^{3+}-binding site incorporation and Ln^{3+} binding. These data could be helpful to guide the optimisation of scaffolds and validate the strategies followed.

All Ln^{3+} coordination sites reported meet Ln^{3+} preference for a high coordination number (CN 8–10) and hard Lewis bases. This includes either natural (Asp, Glu, Gla) or unnatural (Ada_n, $Ed3a_2$) negatively charged AAs and other AAs with O-donor atoms either in their side chains (Asn, Gln) or main chain (carbonyl of peptide bond). When such high CN cannot be achieved solely by the peptide or protein residues, water molecules are found coordinated to Ln^{3+}.

Control over the hydration number is important for applications in imaging (see 6. Applications). A few general principles can be drawn upon the analysis of the CN and q of EF-hand motifs with distinct amino acid patterns (identity and position of residues 1, 3, 5, 9 and 12), which constitute the larger database on this topic. First, in EF-hand the presence of Glu_9 (rather than Asp_9) warrants a coordination sphere devoid of water molecules (q = 0), which, as mentioned above, can be sought to optimize luminescent emission (see 6.1 Luminescent tags and probes). Instead, Asp_9 is never directly involved in Ln^{3+}-binding, but instead hydrogen-bonded to an Ln^{3+}-bound water molecule. Furthermore, higher CN (9–10) are observed in LanM, which are proteins evolved by Nature to bind Ln^{3+} in physiological conditions, relative to Ca^{2+}-binding proteins or engineered LBTs (CN = 7–8). This does not stem merely from a change in the pattern of coordinating amino acids, but rather from second-sphere factors including a fine-tuning of backbone conformation and orientation of amino acid side chains. From the analysis of the data obtained with non-EF-hand scaffolds, two additional general principles can be underlined. First, the denticity of Ln-binding residues impacts q, as is seen with short peptides (*e.g.* Ada_n *vs.* $Ed3a_2$) and coiled coils (*e.g.* Glu *vs.* Gla). Second, the environment in which the Ln-binding site is placed participates in the tuning of q, as evidenced in 3SCC, for which Ln^{3+}-hydration state depends on the position of Ln^{3+}-binding site in different regions (*e.g.* the more solvent-exposed termini *vs.* the buried hydrophobic core of the coiled coils), and on second-sphere effects (*e.g.* tuning of steric hindrance of second sphere residues). Thus, to summarize, control over the hydration number can be achieved by tuning three key parameters: (i) the denticity of Ln-binding residues and the length of their side chain; (ii) the position of the binding site in the scaffold; and (iii) the steric hindrance of second sphere residues. In addition, works on EF-hand motifs underline the influence of a fourth key parameter, more difficult to control, which is the spatial positioning of AAs side chains that allows AAs to bind in a mono- or bi-dentate fashion, and so participate in the fine-tuning of Ln^{3+} hydration number.

3. Thermodynamic stability

3.1 Generalities

3.1.1 Stability constants. The thermodynamic stability, or affinity, of metal–ligand complexes ML_n can be expressed by the overall stability constant β_n, which is the product of stepwise stability constants K_n (eqn (3)):

$$\beta_n = K_1 K_2 \ldots K_n = \frac{[M(L)_n]}{[M][L]^n} \quad (3)$$

The measurement of such a pH-independent formation constant is accessible through, for instance, potentiometric measurements of both apo-ligand and metal–ligand complex pK_as, which represent the most accurate method to determine metal-binding affinities. However, for practical reasons (*e.g.* poor stability over a wide pH range and a large number of protonable sites), potentiometric titrations can be rarely performed on long peptides and proteins. Moreover, K and β values have poor significance under biological conditions, as they correspond to the affinity of a fully deprotonated ligand (*i.e.* at very high pH).

Nevertheless, conditional stability constants, ${}^cK$, at a given pH can be derived from the stability constant K taking into account the protonation constants ($K_{a,n}$) of the ligand (eqn (4)).

$${}^cK = \frac{K}{\left(1 + K_{a,1}[H^+] + K_{a,1}K_{a,2}[H^+]^2 + \ldots K_{a,1}K_{a,2}K_{a,n}[H^+]^n\right)} \quad (4)$$

Conditional stability constants can be also determined through either direct metal–ligand titrations or competition experiments

Open Access Article. Published on 22 September 2025. Downloaded on 4/1/2026 8:13:17 PM.
This article is licensed under a Creative Commons Attribution-NonCommercial 3.0 Unported Licence.

using a second chelator of known affinity in the conditions used.[130,131] In this case, an apparent stability constant, K_{app}, is measured in the presence of the competitor in a given buffer, from which ${}^{c}K$ can be derived by taking into account the concentrations (C) and the conditional stability constants of the competitor (comp) and the buffer (eqn (5)).

$$ {}^{c}K = K_{app}(1 + {}^{c}K_{comp}C_{comp} + {}^{c}K_{buffer}C_{buffer}) \quad (5) $$

The stability constants of peptide and protein scaffolds for Ln^{3+} ions found in the literature and reported in this review have not been corrected for the buffer contribution, and hence they are apparent (K_{app}). This is also due to the lack of reliable stability constants for Ln^{3+}–buffer systems (see Section 3.1.2). In addition, it is noteworthy that the buffer concentration has a considerable impact on the K_{app} of the complex under investigation: for instance, based on eqn (5), in the presence of a buffer with ${}^{c}K_{buffer} = 10^3$, the K_{app} will be ~10-fold or ~100-fold lower than ${}^{c}K$ when the buffer concentration is 10 or 100 mM, respectively.

Another important point to keep in mind is that when working with peptides and proteins, the techniques used to determine the apparent stability constant can monitor the metal binding and/or the induced folding of the scaffold. For instance, CD (circular dichroism) can only inform indirectly on metal binding, since this technique measures metal-induced changes in the scaffold folding. Variations of chemical shifts in NMR spectroscopy are due to both metal-binding and subsequent conformational changes; similarly, ITC (isothermal titration calorimetry) measures the heat exchanged for all events happening during the titration, including conformational changes and metal-binding. To some extent, luminescence titration is also dependent on folding and metal binding. Ln^{3+}–luminescence increases upon Ln^{3+}-binding due to the substitution of water molecules. Thus, in general, Ln^{3+}–luminescence is also sensitive to induced local folding events (*i.e.* the formation of the binding site), but not to conformational changes that are more distant.

It is important to underscore that K_{app} values should be compared only if they were determined in the same conditions (metal and ligand concentration, buffer, pH, *etc.*) and through the same technique, and refers to complexes with the same metal–ligand stoichiometry. For a more accurate comparison of complexes with different metal–ligand stoichiometry or different metal/ligand concentrations, the use of pM (eqn (6)) would be recommended.[132,133]

$$ \mathrm{pM} = -\log[\mathrm{M}] = \log\left({}^{c}K\frac{[\mathrm{L}]^{n}}{[\mathrm{ML}_{n}]}\right) \quad (6) $$

In the following, the thermodynamic stability of different Ln^{3+}-binding peptide and protein scaffolds is discussed. The reported apparent stability constants have been determined with a variety of methods and conditions, preventing rigorous comparisons but allowing discussion and speculation about trends and binding mechanisms.

3.1.2 Ln^{3+} coordination by pH buffers. As mentioned in the former paragraph, knowledge of the stability constant of Ln^{3+} complexes with pH buffers would be beneficial to take their contribution into account and derive buffer-independent binding constants. Only a few data are available in the literature on the affinity of the most common buffer for Ln^{3+} (Table 7). Azab and coworkers studied the thermodynamic stability and speciation of Ln^{3+}–buffers systems using potentiometry.[134–136] They suggested the formation of 1 : 1, 1 : 2 Ln^{3+}–buffer complexes as well as [Ln(buffer)$(OH)_n$] species. The stability constants ($\log\beta$) reported for 1 : 1 Ln^{3+}–buffer complexes range between 3 and 4, but contrasting and hence no reliable values have been reported for the same Ln^{3+}–buffer system.

More recently, the interaction of some buffers with Eu^{3+} was investigated employing NMR and time-resolved laser-induced fluorescence spectroscopy (TRLFS).[137] However, it is not clear how the values found in this study were determined. Overall, there is little agreement on the stability constants of Ln^{3+}–buffers systems, for which reliable values need to be determined. Notwithstanding, given the range of their stability constants, buffers could compete with peptides and proteins with low affinity for Ln^{3+} ions. Therefore, the choice of the pH buffer and its concentration should be considered carefully.

Furthermore, buffer molecules could replace loosely bound water in the coordination sphere of Ln^{3+} complexes, leading to the formation of ternary species, which has been investigated only in a few cases. For instance, Delangle and coworkers compared the number of Ln^{3+}-bound water molecules (hydration number, q) of a Tb^{3+}-cyclic decapeptide complex in HEPES buffer (10 mM, pH 7) and in the absence of buffer at pH 6.5.[41] In both cases, they obtained similar Tb^{3+} luminescence lifetimes and hydration numbers (τ_{H_2O} = 1.65 ms, τ_{D_2O} = 6.99 ms, and q = 2.0 in HEPES buffer; τ_{H_2O} = 1.68 ms, τ_{D_2O} = 6.28 ms and q = 1.9 in absence of buffer), suggesting the absence of buffer molecules in the first coordination sphere of Tb^{3+}.

3.1.3 Ln^{3+} coordination by peptides and proteins. The affinity of peptides and protein scaffolds for Ln^{3+} ions spans over a very wide range ($\log K_{app}$ ~ 2–13; Fig. 15). Table 8 gives some examples of $\log K_{app}$ for Tb^{3+} around neutral pH. Most of the scaffolds, regardless of their origin (natural or artificial) and size, have an affinity in the micro- to nanomolar range ($\log K_{app}$ = 5–9). The highest affinity is exhibited by large

Table 7 Stability constant ($\log\beta$) of 1 : 1 Ln^{3+}–buffers systems

	Buffer					
Ln^{3+}	MOPSO	MES	PIPES	HEPES	POPSO	MOPS
La^{3+}	3.34[a]	3.40[a]	n.d.	3.33[a]	n.d.	n.d.
Ce^{3+}	3.31[a]	3.36[a]	n.d.	3.40[a]	n.d.	n.d.
Pr^{3+}	3.36[a]	3.39[a]	4.11[b]	3.44[a]	n.d.	n.d.
	4.18[b]	4.26[b]				
Eu^{3+}	3.39[a]	3.38[a]	4.22[b]	3.43[a]	3.28[c]	3.68[d]
	4.24[b]	4.27[b]	2.51[c]	3.04[c]	3.68[d]	
		2.57[d]	3.04[d]	3.4[d]		
Gd^{3+}	3.27[b]	3.8[b]	3.57[b]	n.d.	n.d.	n.d.
Dy^{3+}	4.09[b]	4.19[b]	4.03[b]	n.d.	n.d.	n.d.

[a] Ref. 134. [b] Ref. 135. [c] Ref. 136. [d] Values have been calculated by correcting the $\log\beta$ reported in ref. 137 for the buffer pK_as ($\log\beta$ + pK_a): MES, 6.27; PIPES, 7.14; HEPES, 7.56; MOPS, 7.18.[138]

Open Access Article. Published on 22 September 2025. Downloaded on 4/1/2026 8:13:17 PM.
This article is licensed under a Creative Commons Attribution-NonCommercial 3.0 Unported Licence.

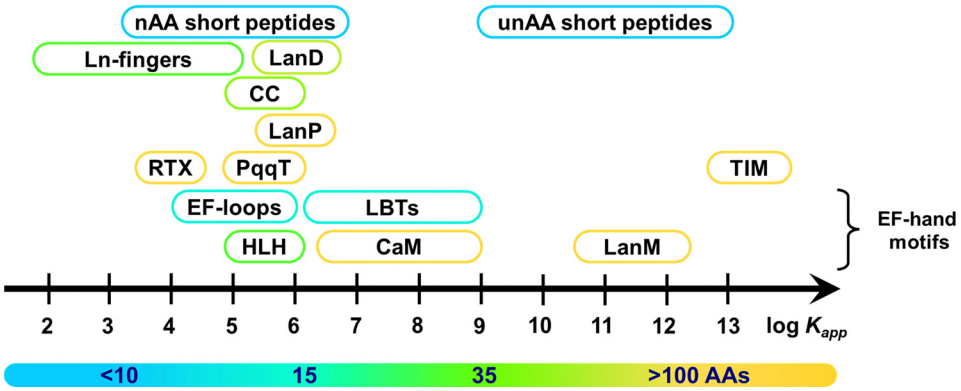

Fig. 15 Affinity range of different Ln^{3+}-binding peptide and protein scaffolds around neutral pH (6–7.5). Colour code is based on the scaffold size (as in Fig. 2). Abbreviations: nAA, natural amino acids; unAA, unnatural amino acids; CC, coiled coils; LBT: Ln-binding tag; HLH, helix-loop-helix.

Table 8 Apparent stability constants of different Tb^{3+} complexes with peptide and protein scaffolds

Scaffold (peptide/protein)	$\log K_{app}$ (Tb^{3+})	Ref.
RTX	4.6[a]	129
Ln-fingers (LF4)	4.9[b]	103
EF-hand (LBT1)	5.1[c]	139
3SCC (MB1-1)	5.3[d]	99
HLH (P3W)	5.4[e]	80
Cyclic decapeptide (PA)	6.3[f]	41
CaM (bovine, site I)	8.8[g]	82
LBT–protein conjugate (ILB1β-L3)	8.9[h]	65
LanM (*Mex*-LanM)	11.1[i]	63
unAA short peptides (P^{HD2})	12.7[j]	87
TIM barrel (TFD-EE N6W)	13.1[k]	126

[a] Bis-Tris 20 mM pH 6, NaCl 25 mM. [b] HEPES 10 mM pH 7.5, NaCl 10 mM. [c] HEPES 10 mM pH 7, NaCl 100 mM. [d] HEPES 10 mM pH 7. [e] HEPES 10 mM pH 6.9. [f] HEPES 10 mM pH 7. [g] PIPES 25 mM pH 6.8, KCl 100 mM. [h] HEPES 10 mM pH 7, NaCl 100 mM. [i] MOPS 30 mM pH 7.2, KCl 100 mM. [j] HEPES 10 mM pH 7, NaCl 100 mM. [k] HEPES 25 mM pH 7.5, NaCl 100 mM.

scaffolds, such as the natural LanM[81] and the *de novo* designed TIM barrel protein (TFD-EE N6W),[126] and by short peptides (6 amino acids) featuring multidentate unnatural amino acids.[87] In the following paragraphs, several factors influencing the affinity of each scaffold will be described and discussed.

3.2 EF-hand motifs

Thanks to the large variety of natural and engineered EF-hand motifs, it is possible to evaluate the effect of several structural factors influencing their affinity for Ln^{3+} ions.

3.2.1 Influence of the protein scaffold. All naturally-occurring 12-residue EF-hand motifs isolated from their either Ca^{2+}- or Ln^{3+}-binding native protein scaffolds show similar affinities in the high micromolar range ($\log K_{app} \approx 5$). Natural Ca^{2+}-binding proteins and LBT–protein conjugates bind Ln^{3+} ions with at best $\log K_{app} \approx 8$–9 at pH ~ 7. LanMs display the highest affinity ($\log K_{app} \approx 10$–12 at pH ~ 7) among naturally-occurring Ln^{3+}-binding scaffolds. The structural determinants of such enhanced affinity are not clear. Based on the current literature,[62,81,83] it seems that it results from second-sphere effects, including different loop backbone conformation and hydrogen bonding networks that ensure an optimal orientation of coordinating amino acids within the loop.

The loss of 5 orders of magnitude in Tb^{3+} affinity when EF1-3 loops are isolated from their native *Mex*-LanM scaffold ($\Delta\log K_{app} \approx 5$, see entries 1 and 2, Table 9) highlights the momentous impact of a suitably folded, but not necessarily predisposed (note the LanM is disordered in the apo-state) scaffold on the affinity.

The important role of the core helical bundle in LanM has been further underscored by the recent study of a *Mex*-LanM fragment encompassing the highest-affinity and cooperative EF2-3 domains devoid of flanking helices, which showed much weaker affinity ($\log K_{app} < 5$) than the whole protein.[140] Besides, another recent study has explored the impact of replacing EF-loops in CaM with those found in *Mex*-LanM.[141] Interestingly, this chimaera (LanM-GCaMP) showed a weak conformational response to Ln^{3+} (from the micro- to the milli-molar range, depending on the Ln^{3+}). Nevertheless, the authors were able to obtain a modified CaM scaffold (LanTERN) with a conformational transition similar to LanM ($\log K_{app} = 10.3$ for La^{3+}) by introducing key mutations in CaM loops that are considered responsible for enhanced Ln^{3+} selectivity in LanM (*i.e.* Pro_2 and Asp_9, see Section 3.2). Altogether, this evidence suggests that to further boost the Ln^{3+}-binding affinity of EF-hand proteins, the loop sequence, including non-coordinating amino acids, and the protein folding must be optimised simultaneously.

3.2.2 Influence of primary sequence and post-translational modifications. The primary sequences of LBT have been artificially evolved mainly to optimize Tb^{3+} luminescence and affinity. Hence, they represent an outstanding dataset to derive structure–affinity relationships. In particular, the impact of specific modification can be quantified by comparing structurally analogous peptides (Table 9). For instance, the incorporation of hydrophobic amino acids (Phe, Tyr, Ile) at both N- and C-terminal to constrain the loop contributes to almost 1 order of magnitude of affinity (entries 4 *vs.* 3 in Table 9).[72] A similar gain in affinity (about 1.5 order of magnitude) was accomplished by

Open Access Article. Published on 22 September 2025. Downloaded on 4/1/2026 8:13:17 PM.
This article is licensed under a Creative Commons Attribution-NonCommercial 3.0 Unported Licence.

Table 9 Apparent stability constants of Tb^{3+} complexes with distinct EF-hand motifs

Entry	Sequence	Peptide/Protein	log K_{app}	Ref.
1	DPDKDGTIDLKE DPDKDGTLDAKE DPDNDGTLDKKE NPDNDGTIDARE	Isolated EF1-4 from Mex-LanM	5.1 [a]	143
2	DPDKDGTIDLKE DPDKDGTLDAKE DPDNDGTLDKKE	LanM EF1-3	10.7 [b]	63
3	GDYNADGWIEFEEL	LBT precursor	5.1 [c]	139
4	YIDTNNDGWIDGDELLA	m-sSE3 (LBT)	5.9 [d]	60
5	YIDTDNDGWIDGDELLA	q-sSE3 (LBT)	7.5 [d]	60
6	YIDTNNDGWIEGDELLA	sSE3 (LBT)	7.4 [c]	68
7	GDYNKDGWYEELEL	LBT1	5.1 [c]	139
8	c(ACAGDYNKDGWYEELECAA)	LBTC2	6.6 [c]	139
9	…YIDTNNDGWIEGDEL…	ILB1β-S1 (LBT-protein)	8.1 [c]	65
10	…YIDTNNDGWIEGDEL…	ILB1β-L3 (LBT-protein)	8.9 [c]	65
11	…DKDGDGTIDERE…	P3W (HLH)	5.4 [e]	80

[a] MOPSO 10 mM pH 6.6, KCl 100 mM
[b] MOPS 30 mM pH 7.2, KCl 100 mM
[c] HEPES 10 mM pH 7, NaCl 100 mM
[d] HEPES 20 mM pH 7.5, NaCl 100 mM
[e] HEPES 10 mM pH 6.9

the cyclization of the EF-loop termini through the formation of disulfide bonds between Cys suitably located upstream and downstream of the loop (entries 8 *vs.* 7 in Table 9).[139,142]

Furthermore, as already mentioned for natural proteins, the insertion of LBT within a protein scaffold increases the affinity up to $\log K_{app} \approx 8$–9 (entries 8–9 in Table 9). Of note, the rigidity of the regions flanking the loops is also crucial to achieving such an enhancement of the affinity, which is not accomplished, for instance, in the chimeric helix-loop-helix domains ($\log K_{app} \approx 5$–6) likely due to the high flexibility of the flanking helices (entry 11 in Table 9).[80]

The pattern of coordinating amino acids in the EF loop also influences the affinity. Notably, the affinity increases of more than 1 order of magnitude (entries 5–6 *vs.* 4 in Table 9) when (i) Asn_3 is mutated to Asp (entries 5 *vs.* 4 in Table 9), likely due to the more negative charge of Asp relative to Asn, and (ii) Asp_9 is replaced by Glu (entries 6 *vs.* 4 in Table 9), which serves as bidentate ligands displacing the Ln^{3+}-bound water hydrogen-bonded to Asp_9.

In order to develop kinase/phosphatase- and nitration-responsive probes (see 6.1.5 Probe design and selected applications), the group of Zondlo has also widely explored EF-hand motifs featuring phosphorylated and nitrated amino acids, including phosphotyrosine (pTyr), phosphoserine (pSer), phosphothreonine (pThr) and 3-nitrotyrosine (nTyr). These studies have shown that Glu_9 can be replaced by pSer, pTyr and nTyr with minor impact ($\Delta\log K_{app} < \pm 1$) of the EF-loop affinity (entries 1–5 in Table 10).[144–146] A similar effect was also observed when Asp residues in positions 1, 3 or 5 were replaced by Cys sulfinic acid (entries 7–9 in Table 10).[147] Remarkably, an affinity gain of about 1 order of magnitude was reported when Asp_9 was replaced by pThr (entry 6 in Table 10).[148] Interestingly, a similar affinity gain was also observed for C-terminally truncated 9-residues loops bearing $pThr_9$ or $pSer_9$ (entries 10–12 in Table 10).[148] Unfortunately, the lack of structural studies prevents a detailed description of the Ln^{3+} coordination sphere in these modified EF-hand motifs. Noteworthy, the impact of phosphorylated or nitrated amino acids in natural EF-hand proteins has not been investigated yet.

With respect to Ln^{3+} binding to phosphorylated peptides, it is also worth pointing out that a micromolar affinity for Tb^{3+} ($\log K_{app} = 6.5$ at pH 7) has been reported for a fragment of the

Open Access Article. Published on 22 September 2025. Downloaded on 4/1/2026 8:13:17 PM.
This article is licensed under a Creative Commons Attribution-NonCommercial 3.0 Unported Licence.

Table 10 Apparent stability constants of Tb^{3+} complexes with different EF-hand motifs bearing modified amino acids (in red). pSer = phosphoserine; pTyr = phosphotyrosine; nTyr = 3-nitrotyrosine; pThr = phosphothreonine

Entry	Sequence	Peptide/Protein	Modified amino acid	log ᶜK	Ref.
1	DKNADGWIDAAEK	EF-E12	n/a	4.1 [a]	144
2	DKNADGWIDAASLK	phospho-pKID-PKC	$pSer_9$	3.7 [a]	145
3	DKNADGYIDAAYK	phospho-pKID-pTyr12	$pTyr_9$	3.7 [a]	144
4	DKDADGWISPAYAK	pNO2-Y(OPO3)12	$pTyr_9$	4.4 [a]	146
5	DKDADGWISPAYAK	pNO2-Y(NO2)12	$nTyr_9$	4.8 [a]	146
6	DLNADGWITAATAK	phospho-pKID-Min-pThr9	$pThr_9$	4.9 [b]	148
7	CKDADGWISPAEAK	pSO_2-C1-SO_2^-	$sCys_1$	5.0 [a]	147
8	DKCADGWISPAEAK	pSO_2-C3-SO_2^-	$sCys_3$	3.8 [a]	147
9	DKDACGWISPAEAK	pSO_2-C5-SO_2^-	$sCys_5$	3.9 [a]	147
10	DLNADGWIT	phospho-pKID-Min2	$pThr_9$	5.0 [b]	148
11	DLNADGWIS	phospho-pKID-Min1	$pSer_9$	4.8 [b]	148
12	DKDADGWIS	phospho-pKID-Min4	$pSer_9$	5.2 [b]	148

[a] HEPES 5 mM pH 7.8, NaCl 100 mM
[b] HEPES 10 mM pH 7.5, NaCl 100 mM, $MgCl_2$ 2 mM

protein α-synuclein (119–132) with an EF-hand-like amino acid pattern and bearing a pTyr residue (Asp_1, Asp_3, Glu_5, $pTyr_7$, Glu_{12}).[149]

3.3 Other scaffolds

3.3.1 Short and intermediate-size scaffolds. In short and intermediate-size peptides, three main parameters influenced the affinity for Ln^{3+}: (i) the set of coordinating amino acids; (ii) their denticity and (iii) scaffold stability.

Among the short peptides reported in the literature (cyclic or linear), the one with the best affinity was obtained when using unnatural amino acids for Ln^{3+}-binding (P^{HD2} with Ada_2 and $Ed3a_2$, $\log K_{app}$ = 12.7, Fig. 5).[87] Compared to Glu and Asp, these unnatural amino acids have a higher denticity, which is more favourable for Ln^{3+} binding. Furthermore, the peptide backbone designed to adopt a β-turn-fold upon metal binding provides additional stabilising interactions that make the peptide a better ligand than aminodiacetate groups separated by long alkyl chains ($n > 2$), but not as good as ligands such as EDTA for which the formation of 5- and 6-membered chelate rings result in a large stabilising chelate effect.[85]

The influence of the coordination sphere on the apparent affinity constants is evidenced for LF scaffolds, in which modification of the coordination sphere from $(Asp)_2(Glu)_2$ (LF4) to $AspAsn(Glu)_2$ (LF7) decreased the apparent affinity constant for Eu^{3+} from $\log K_{app}$ = 4.6 to $\log K_{app}$ = 4.0. It is also apparent in the 3SCC designed by Peacock and coworkers when comparing the affinity of MB1-1 and CS1-1 for Tb^{3+} ($\log K_{app}$ = 5.3 *vs.* 4.6, respectively).[99] The additional $(Asn)_3$ layer in MB1-1 contributes to the slightly higher affinity observed relative to CS1-1. However, a change of hydration number for a given coordination sphere does not impact the apparent affinity constant, as can be seen in the 3SCC MB1-*n* series (n = 1–4), which have comparable affinities for Tb^{3+} ($\log K_{app}$ = 5.2–5.5) and hydration number ranging from q = 0 (MB1-2 and MB1-3) to q = 3 (MB1-1).[99]

The influence of denticity on Ln-affinity is well illustrated by the 2SCC described by Hodges when using Gla instead of Glu.[95] The affinity of $E_2(15,20)_{ox}$ has a $\log K_{app} \approx 2$ for La^{3+}, whereas the one of $Gla_2(15,20)N_{ox}$ has a $\log K_{app}$ = 6.2 for La^{3+}, which can be linked to the higher denticity of the latter.

Finally, the link between scaffold stability and Ln-affinity was investigated in the design of the Ln-finger series. Changes in the sequence to improve the formation of secondary structures resulted in improved apparent affinity constants from $\log K_{app} < 2$ for Eu^{3+} of LF1, to $\log K_{app}$ = 3.7 of LF3.[103] Increasing the size of the binding site by deletion of two AAs (LF4) gave the best apparent affinity constant for Eu^{3+} with $\log K_{app}$ = 4.6. In the MB1 series shifting the position of the binding site within the 3SCC scaffold impacted the stability of the assembly (see 2.4.1 Coiled coils).[99] However, this did not significantly impact the apparent affinity constants for Tb^{3+}, which were all in the range $\log K_{app}$ = 5.2–5.5. The addition of an additional heptad in MB1-1L also did not impact the apparent affinity constant for Tb^{3+} ($\log K_{app}$ = 5.0).[102]

Open Access Article. Published on 22 September 2025. Downloaded on 4/1/2026 8:13:17 PM.
This article is licensed under a Creative Commons Attribution-NonCommercial 3.0 Unported Licence.

3.3.2 Proteins. Proteins without EF-hand motifs cover a wide range of affinities for Ln^{3+} with $\log K_{app}$ ranging from 4 to 13. This large range of affinities can be explained by Ln^{3+}-binding sites that are either not fully optimised for Ln^{3+}-binding (*e.g.* in Ca^{2+}–proteins), or found in natural proteins whose biological function may require affinity in an intermediate range (*e.g.* LanP, LanD).

The Ca^{2+}-binding protein RTX has an apparent affinity constant for Ln^{3+} in the range $\log K_{app}$ = 4.1–4.6 at pH 6, and may bind 4 to 7 Ln^{3+} per protein.[129] Note that these values were obtained for a fusion protein, in which RTX is fused with two fluorescent proteins for detection of folding upon metal binding by FRET. The affinity of LanP for Ln^{3+} is $\log K_{app}$ = 6.0 and this protein binds 3 to 4 Ln^{3+}.[122] It was identified in Ln-utilizing organisms and due to its Ln^{3+}-binding ability, it was hypothesized that LanP could be of importance in Ln-dependent methylotrophy. Similarly, the apparent affinity constant of the monomeric protein LanD for Ln^{3+} ranges from $\log K_{app}(La^{3+})$ = 5.7 to $\log K_{app}(Nd^{3+})$ = 6.6.[125] Because LanD and LanM are part of the same gene cluster involved in Ln^{3+} transport and utilisation, it was proposed that LanD could be responsible for transferring Ln^{3+} to LanM. This hypothesis was supported by the metalation of the modified fluorescent LaMP1[123] in the presence of La^{3+}–LanD, and by ITC titration experiments that showed a specific 1 : 1 interaction between apo-*Mex*-LanD and apo-*Mex*-LanM with a dissociation constant of 4 μM of physiological relevance. As of now, little is known about the coordination environment of Ln^{3+} in these proteins, except for LanD, and the stability of these scaffolds. This does not allow the identification of specific features that could explain the affinity range observed.

When the protein scaffold and Ln^{3+}-binding site are optimised, high affinity can be obtained by design, as is the case for the computationally designed TIM barrel that displayed the highest affinity for Ln^{3+}.[126,150] The affinity of the mutant with a $(Glu)_4$ binding site and Trp for Tb^{3+}-sensitisation (TFD-EE N6W) was first suggested to be $\log K_{app} \approx 15$ by competitive titration with EGTA.[126] However, when the same experiments were reproduced with a higher concentration of Tb^{3+}–EGTA relative to TFD-EE N6W and longer equilibration times, the apparent affinity constant for Tb^{3+} was rather found to be $\log K_{app}$ = 13.1.[150] Of note, this stressed the importance of taking into account kinetic considerations (see 5. Kinetic stability), since when protein metalation, or metal ion exchange with a given competitor, is slow, reaching the thermodynamic equilibrium may take days as it is the case for this example. Nevertheless, it also shows that in a rigid scaffold ($T_m > 95$ °C) with a predisposed binding site suitable for Ln^{3+}-binding, high affinity can be achieved by rational design.

Ln-ADH and its mimics stand apart since Ln-binding depends not only on the protein but also on the presence of the cofactor PQQ. Early work on Ln-ADH extrapolated apparent affinity constant based on activity assays and predicted an affinity in the low μM range for Ln^{3+} in the presence of PQQ ($\log K_{app} \sim 6$).[112,119] More recently, Zeymer and coworkers studied the affinity of a PedH mutant for Ln^{3+} in the absence of PQQ in the active site.[19] They determined an apparent affinity constant $\log K_{app}$ = 7.0 for Tb^{3+} by luminescence titration, and $\log K_{app}$ = 6.2 for Ce^{3+} based on competition with Tb^{3+}. Similarly, for the engineered PqqT scaffold, a $\log K_{app}$ = 6.2 was obtained for the mutant PqqT–K_{142}D containing PQQ (noted PQQ⊂PqqT–K_{142}D).[20] This represents a 10-fold improvement compared to the wild-type scaffold (PQQ⊂PqqT) and to the PQQ⊂PqqT–K_{142}A mutant. The presence of PQQ inside the protein was required for Ln^{3+}-binding, as demonstrated by controlled experiments performed with the apo-scaffolds (PqqT, PqqT–K_{142}A, and PqqT–K_{142}D).

3.4 Effect of the pH

Ln recovery requires ligands with high affinity and selectivity for Ln^{3+} ions at pH ranging from pH < 1 to pH = 5–6 depending on the source (see 6. Applications).[151,152] The capacity to bind Ln^{3+} ions in acidic conditions is an overlooked feature of peptides and proteins, mainly because (i) protein folding is generally sensitive to acidic pH and (ii) typical Ln^{3+}-binding residues (Asp, Glu) become protonated below pH 3–4, weakening Ln^{3+} binding.

Nonetheless, some works investigated the pH sensitivity of their scaffolds. 3SCC loose their Ln^{3+}-binding ability below pH ∼ 4–5.[92] CaM and LBTs start releasing Ln^{3+} below pH 6 and show no binding below pH 4.[153,154] Similarly to small chelators such as EDTA and DTPA, LanMs are able to bind Ln^{3+} ions down to pH ∼ 2.5, retaining approximately nanomolar affinity at pH 4 ($\log K_{app} \approx$ 8–9) and 5 ($\log K_{app} \approx$ 9–10).[155] The reason behind the higher pH stability of LanM relative to CaM and LBTs is not understood. Interestingly, the RTX scaffold has been recently reported to retain partial Ln^{3+}-binding below pH 2. The protein could recover up to 20% of Nd^{3+} from a synthetic NdFeB magnet solution containing Nd, Dy, Fe and Co at pH < 1.[129]

On the other end of the pH scale, studies on 3SCC scaffolds also showed that such moderate-affinity ligands undergo partial de-complexation of Ln^{3+} at basic pH (> ∼8.5), likely due to competing formation of lanthanide hydroxides.[92]

More systematic studies will be necessary to understand the different pH-dependence of Ln^{3+} binding to different peptide and protein scaffolds.

3.5 Discussion and guidelines

Among natural peptide and protein scaffolds, LanM stands out for its $\log K_{app} \approx$ 10–12. Although the structural factors for this remarkably high affinity have not been fully elucidated yet, the constraint imposed by the global protein scaffold, even if not pre-folded, is paramount. Indeed, isolated EF-loops with the same potential coordinating residues are much weaker ligands.

All rationally designed scaffolds with natural amino acids (*i.e.* short peptides, LFs and CCs), except for the TIM barrel ($\log K_{app}(Tb^{3+})$ = 13.1), have lower or at best comparable, affinity than natural scaffolds. As was noted earlier, these small to intermediate scaffolds are sensitive to the insertion of a metal-binding site, which destabilises the structure and in turn, may decrease Ln^{3+}-affinity. Peptides tend to be flexible and explore a large conformational space. Ln^{3+}-binding may improve the folding of the peptide; however, it is generally not sufficient

Open Access Article. Published on 22 September 2025. Downloaded on 4/1/2026 8:13:17 PM.
This article is licensed under a Creative Commons Attribution-NonCommercial 3.0 Unported Licence.

by itself to compensate for the entropic cost of restricting the peptide conformational space. Optimisations of the peptide sequence to improve the formation of secondary structures can help fold the peptide, and hence, increase the affinity for Ln^{3+}. This is observed qualitatively by the successive optimisations performed on Ln-fingers. It is also the case for the *de novo* designed TIM barrel, whose packing was optimised to rigidify the structure, and which displays a high stability ($T_m > 95$ °C) and affinity for Ln^{3+}. Similarly, even though LanMs are not pre-folded, their affinity for Ln^{3+} is coupled to the formation of a thermally stable ($T_m > 95$ °C) folded protein. Nonetheless, there seem to be limitations to this, as increasing the size and stability of 3SCC (MB1-1 *vs.* MB1-1L) did not result in an impact on Ln^{3+}-affinity.[102] This could be due to the position of the binding site at the N-terminal, whereas the elongation was at the C-terminal. Interestingly, the correlation between the stability of the scaffold and metal-binding affinity has been observed for other metal-binding peptides. Studies performed on β-sheet WW-domain-like metal binding mini-proteins showed an improved affinity for Zn^{2+}, Cu^{2+} and Ni^{2+} by improving the stability of the scaffold.[156] Moreover, a study on Hg- and Cd-binding coiled coils demonstrated a direct correlation between the stability of the coiled coil scaffold and metal ion affinity.[157] Altogether, these data validate the strategy of optimising the scaffold structure in order to improve Ln^{3+}-affinity.

An alternative strategy is to use unnatural amino acids. Indeed, affinities comparable to that of LanM or TIM barrel were achieved in very short peptides (6 AAs) by combining Ada_n and $Ed3a_2$ (P^{HD2}, $\log K_{app}(Tb^{3+}) = 12.7$). Even in this case, the primary sequence played an important part since residues that favour the formation of a β-turn upon metal-binding were chosen to bring additional stabilising interactions.

4. Selectivity

The selectivity of peptide and protein scaffolds for Ln^{3+} *vs.* other metal ions is a key aspect for their applications in both environmental and biological samples, as well as for understanding Ln biochemistry. In particular, the selectivity among Ln^{3+} and against actinides (An^{3+}) is of interest for Ln^{3+} mining and separation, while the selectivity for Ln^{3+} over Ca^{2+} and other physiological cations (*e.g.* Zn^{2+} and Cu^{2+}) is particularly relevant in the biological context.

The selectivity between two different metal ions can be quantified by calculating the selectivity factor, $\Delta\log K$ (or $\Delta\log\beta$), which corresponds to the difference between the affinities of a certain ligand for distinct metal ions. In the following, we will express the Ln^{3+}-selectivity, $\Delta\log K^{Ln}$ (or $\Delta\log\beta^{Ln}$) as the difference between the lowest and the highest $\log K^{Ln}$ along the series (eqn (7)).

$$\Delta\log K^{Ln} = \log K^{Ln}_{max} - \log K^{Ln}_{min} \quad (7)$$

Similarly, the selectivity for Ln^{3+} *vs.* Ca^{2+}, $\Delta\log K^{Ca}$ ($\Delta\log\beta^{Ca}$), is expressed as the difference between the $\log K^{Ln}$ for a certain Ln^{3+} and $\log K^{Ca}$ (eqn (8)).

$$\Delta\log K^{Ca} = \log K^{Ln} - \log K^{Ca} \quad (8)$$

4.1 Selectivity among Ln^{3+}

Prior to peptides and proteins, it is useful to discuss the selectivity of small chelators (Fig. 16 and 17A), which can be classified into four types.[158–161]

Most ligands, including EDTA (Fig. 16), show increasing stability constants across the Ln series (type I, black dots, Fig. 17A), commensurate with the increase of Ln^{3+} Lewis acidity. For other ligands, such as DTPA and DOTA (Fig. 16), the affinity increases along the first part of the series, reaches a maximum and then remains constant or even decreases for late Ln^{3+} ions (type II, red dots, Fig. 17A). This is the result of the ligand steric hindrance, which impairs to accommodate the smaller Ln^{3+} ions.[158,159,162]

An uncommon behaviour is shown by a few ligands, including Macropa (Fig. 16), for which a reverse-size selectivity is observed due to a fairly rigid scaffold better suited for larger than smaller Ln^{3+} ions (type III, blue dots, Fig. 17A).[160] Finally, a biphasic selectivity trend (type IV, green dots, Fig. 17A) has been recently reported with ligands such as Macrotripa (Fig. 16) that are better suited for both early and late Ln^{3+} due to a switch between a 10-coordinated conformation accommodating larger Ln^{3+} ions and an 8-coordinated conformation stabilizing smaller Ln^{3+} ions.[161,163]

Overall, the selectivity trend among Ln^{3+} ions results from a compromise between electronic and steric effects, whose

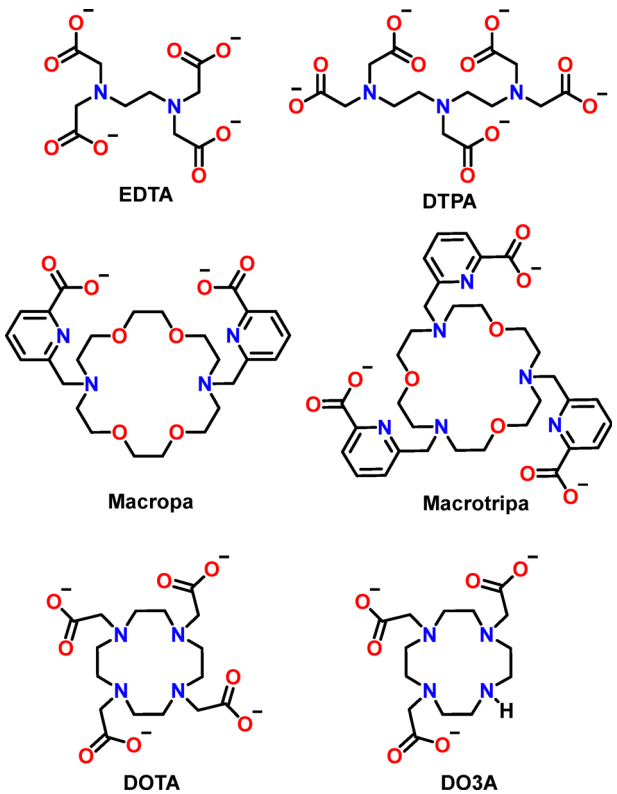

Fig. 16 Chemical structure of the Ln^{3+} chelators mentioned in the text.

Open Access Article. Published on 22 September 2025. Downloaded on 4/1/2026 8:13:17 PM.
This article is licensed under a Creative Commons Attribution-NonCommercial 3.0 Unported Licence.

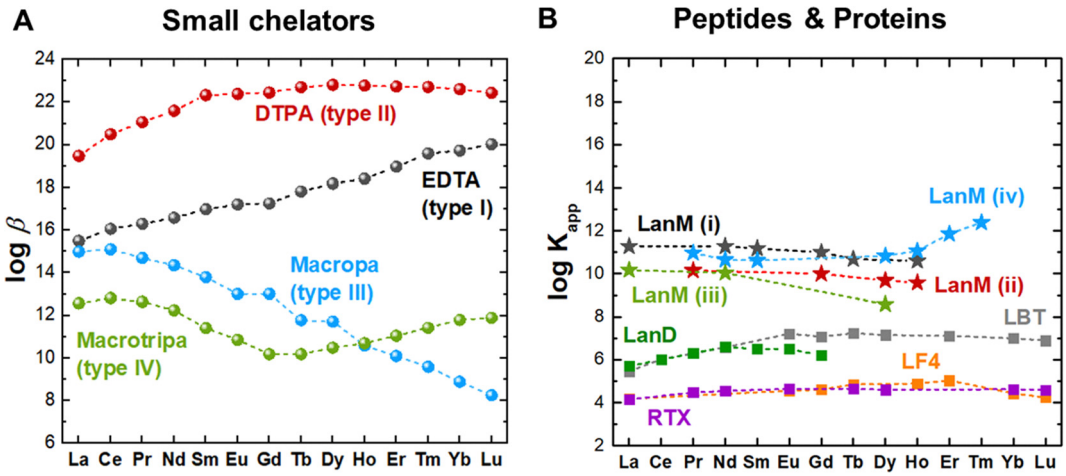

Fig. 17 Selectivity of different ligands across the Ln^{3+} series. (A) Small chelators and (B) peptides and protein scaffolds. Note that log β and log K_{app} are reported in (A) and (B), respectively. Values for LanM are referred to (i) *Mex*-LanM at pH 7.2 measured by CD spectroscopy; (ii) *Mex*-LanM at pH 5 measured by CD spectroscopy; (iii) *Hans*-LanM at pH 5 measured by CD spectroscopy; (iv) *Mex*-LanM at pH 5 measured by UV-vis spectroscopy. The values plotted are reported in Table 15.

balance varies depending on the properties of the ligand, such as its denticity and rigidity. Moreover, the behaviour of these small chelators points out a common misconception: Ln^{3+} are not all the same, especially when bound to a chelator. Indeed, a remarkable difference can be observed in the stability constants of certain ligands for distinct Ln^{3+} ions: for instance, EDTA and Macropa show selectivity for Lu^{3+} *vs.* La^{3+} ($\Delta\log\beta^{Ln}$) of ~5 and ~7 orders of magnitude, respectively.

The Ln^{3+}-selectivity of only a few peptides and protein scaffolds has been reported (Fig. 17B). LBTs, Ln-fingers, RTX and LanD display a type II selectivity (Fig. 17B). The affinity of LBTs increases by almost 2 orders of magnitude from La^{3+} up to Ln^{3+} in the middle of the series (Eu^{3+}–Tb^{3+}) and then slightly decreases towards the end of the series.[64] Since LBTs were derived from Ca^{2+}-binding loops, their preference for middle-sized Ln^{3+} ions (1.04–1.07 Å, CN = 8 in LBTs) could be explained by the closer similarity to Ca^{2+} ionic radius (1.06 Å, CN = 7 in EF loops).

Ishida and coworkers employed molecular dynamics simulations, as well as ITC and NMR measurements, in order to elucidate the selectivity trend of LBTs.[164] The authors found that one or two water molecules can be accommodated in the coordination sphere of large Ln^{3+} ions (La^{3+}–Nd^{3+}); this weakens the binding between the Ln^{3+} and Asn_5 and enhances the flexibility of the complex, resulting in reduced affinity. For Ln^{3+} from Sm^{3+} to Lu^{3+}, water binding is rarely observed, correlating with the higher affinity for these smaller ions.

For LF4, the affinity increases by nearly 1 order of magnitude from La^{3+} to Er^{3+}, then decreases back towards Lu^{3+}, which was found to have the same affinity as La^{3+}.[103] A similar trend is shown by RTX and LanD proteins, but in this case the $\Delta\log K^{Ln}$ measured is much lower (<1).[125,129]

The relative selectivity of 3SCC among Ln^{3+} has been also reported based on luminescence measurements of Tb^{3+} displacement by other Ln^{3+} ions.[101] A bell-shaped selectivity trend was found for several 3SCC scaffolds that differ for the location of the Ln^{3+}-binding site along the helices (MB1 series, Fig. 18 and Table 5). In particular, no significant discrimination was observed among medium-sized Ln^{3+} ions (Nd^{3+}–Tb^{3+}) for all scaffolds. For competing ions smaller than Tb^{3+}, size-dependent discrimination was observed with scaffolds where the binding site is located around the centre or the C-terminal of the coiled coil. The higher promiscuity of the N-terminal

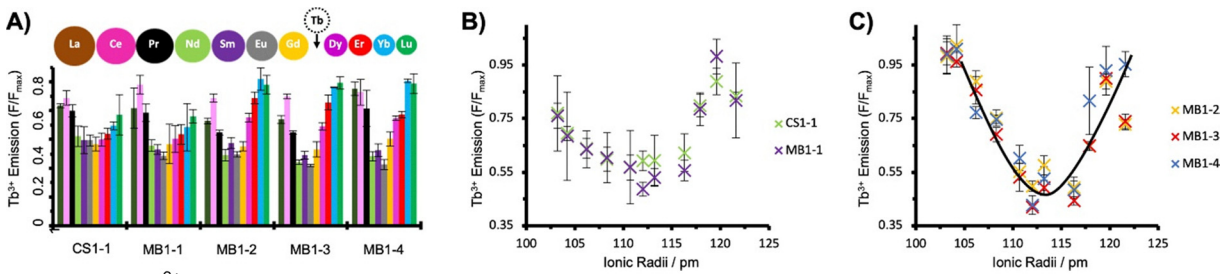

Fig. 18 Tb^{3+}–displacement experiments followed by luminescence in three-stranded coiled coils showing a bell-shape selectivity within the Ln^{3+} series (MB1 series, Table 5). (A) Luminescence displacement, (B) Comparison of CS1-1 and MB1-1, (C) Comparison of MB1-2, MB1-3, and MB1-4. Reproduced from ref. 101.

Open Access Article. Published on 22 September 2025. Downloaded on 4/1/2026 8:13:17 PM.
This article is licensed under a Creative Commons Attribution-NonCommercial 3.0 Unported Licence.

binding site was attributed by the authors to its greater flexibility, which hence allows it to better accommodate also smaller Ln^{3+} ions.[101]

LanP[122] and PqqT[20] do not display significant selectivity among early Ln^{3+} ions (La^{3+}–Gd^{3+}; late Ln^{3+} were not studied). The TIM barrel TDF-EE N6W binds Eu^{3+}, Gd^{3+}, and Tb^{3+} with comparable affinity, while ~10-fold weaker binding was observed with Ce^{3+}.[126]

Among Ln^{3+}-binding peptides and proteins, LanM represents a peculiar and controversial case. In most reports by the groups of Cotruvo and Daumann, an unusual preference of LanM for larger (La^{3+}–Eu^{3+}) over smaller Ln^{3+} ions has been underscored based on CD and luminescence measurements,[81,123,165] which are responsive to both Ln^{3+} binding and Ln^{3+}-induced conformational change (Fig. 17B, LanM(i) and LanM(ii)). It must be noted again, that similarly to RTX and 3SCC, *Mex*-LanM shows a very modest Ln^{3+}-discrimination ($\Delta\log K^{Ln} \sim 0.5$) relative to small chelators and LBTs (Fig. 17B). An enhanced selectivity ($\Delta\log K^{Ln} \approx 1.6$) for early ($La^{3+}$, Nd^{3+}) *vs.* late Ln^{3+} (Dy^{3+}) was found for *Hans*-LanM (Fig. 17B, LanM(iii)), thanks to a Ln^{3+} size-dependent dimerization.[62]

Curiously, the opposite trend, *i.e.* an affinity increase across the end of the Ln^{3+} series, was observed when the intrinsic Ln^{3+}-affinity of *Mex*-LanM was determined *via* UV-vis-NIR spectrophotometric competition experiments (Fig. 17B, LanM(iv)).[155] As suggested by the authors,[166] this could highlight a decoupling between Ln^{3+}-binding and conformational change in LanM, which warrants further investigations, and underscores the importance of the method and the conditions chosen to determine and compare affinity values. Nonetheless, higher retention of early *vs.* late Ln^{3+} ions was observed for immobilized LanM upon pH-induced desorption.[62,167,168] Such (at least apparent) inconsistency between the affinity values measured *via* different techniques and in different conditions is worth further systematic investigations.

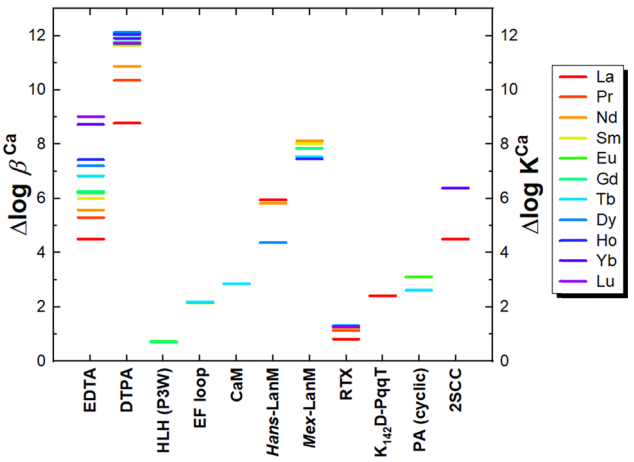

Fig. 19 Selectivity of small chelators and some peptide/protein scaffolds for Ln^{3+} over Ca^{2+}. $\Delta\log\beta$ and $\Delta\log K_{app}$ are reported for small chelators and peptide/protein scaffolds, respectively. Values plotted were calculated from values reported in Table 16.

Finally, it is also worth mentioning that LanM showed higher affinity for the rare-earth element Sc^{3+} relative to Ln^{3+} ions (3-fold higher relative to Nd^{3+}),[167] commensurate with its smaller ionic radius and higher Lewis acidity.

4.2 Selectivity over Ca^{2+}

Peptide and protein scaffolds generally show selectivity for Ln^{3+} relative to Ca^{2+} (and Mg^{2+}) which is classically attributed to their higher charge and coordination numbers (Fig. 19). In addition, as Ln^{3+} have higher CN than Ca^{2+} in water, Ln^{3+}-binding releases a higher number of water molecules, resulting in a more favourable entropic change.

Among the EF-hand motifs, LanMs show a remarkably higher conformational selectivity against Ca^{2+} ($\Delta\log K^{Ca} \approx 8$ for *Mex*-LanM)[81,155] relative to both natural and engineered EF loops ($\Delta\log K^{Ca} \approx 1$–3).[59,82,169] In this respect, it is worth noting that Ca^{2+} seems to bind to LanM with $\log K^{Ca} = 5.5$ without inducing a conformational change, which occurs upon further Ca^{2+} binding events with $\log K^{Ca} \approx 3$.[81]

The Pro_2 residue found in all EF loops of *Mex*-LanM is crucial for the conformational selectivity of LanM for Ln^{3+} over Ca^{2+}. Notably, mutation of all four Pro_2 residues to Ala reduces the selectivity of *Mex*-LanM for Ln^{3+} against Ca^{2+} by strengthening the conformational response of Ca^{2+}-binding to LanM of more than 2 order of magnitudes.[81] Moreover, Pro_2 also had a key role in the Ln^{3+}-specific conformational response of LanTERN chimera already discussed above (see 3.2.1 Influence of the protein scaffold).[141] However, it is noteworthy that high selectivity over Ca^{2+} ($\Delta\log K_a^{Ca} \approx 4$–6) is also observed in *Hans*-LanM, in which a Pro_2 residue is found only in one of the four EF-hand loops. Hence, it is likely that the unique selectivity of LanM for Ln^{3+} *vs.* Ca^{2+} stems from minor differences in the second coordination sphere and backbone conformation.[62]

The main difference between Ca-dependent and Ln-dependent alcohol dehydrogenases is the presence of an additional Asp in the coordination sphere of Ln^{3+}. This residue appears essential for Ln^{3+}-coordination and selectivity relative to Ca^{2+}. Indeed, mutation of this AA to Ala in MDH and EDH enzymes led to the production of enzymes metallated only with Ca^{2+}.[110] However, the mutation did not lead to catalytically competent Ca-enzymes, which underscores that differences between Ca-dependent and Ln-dependent ADH beyond the metal coordination sphere are important for catalysis.

Among the *de novo* designed Ln^{3+}-binding proteins, 2SCC scaffolds bearing non-canonical multidentate carboxyglutamic (Gla, Fig. 6) residues show a selectivity over Ca^{2+} comparable to that of small chelators and LanMs.[95]

4.3 Selectivity over An^{3+}

The groups of Deblonde and Daumann have explored the capacity of *Mex*-LanM to bind An^{3+} ions.[165,170–172] LanM exhibits a higher affinity for An^{3+} over Ln^{3+} ions and Y^{3+}. In particular, a ~5-fold stronger affinity was found for Am^{3+} and Cm^{3+} relative to Ln^{3+} of similar size (Pr^{3+}, Nd^{3+}, Sm^{3+}),[170] and for Ac^{3+} over Y^{3+}.[171] This trend is similar to that of small

Open Access Article. Published on 22 September 2025. Downloaded on 4/1/2026 8:13:17 PM.
This article is licensed under a Creative Commons Attribution-NonCommercial 3.0 Unported Licence.

chelators such as EDTA and DTPA, which show slightly higher selectivity for Am^{3+} over Nd^{3+} ($\Delta\log\beta \sim 1.5$).[173]

For small complexes, the non-negligible covalency of An^{3+}–ligand bonds has been generally considered accountable for the higher stability of An^{3+}-complexes over their Ln^{3+}-analogues, but this remains to be ascertained for An^{3+}–protein complexes.[170]

An improved selectivity for An^{3+} over Ln^{3+} ions at low pH ($\sim$3) was obtained by Deblonde and coworkers *via Mex*-LanM engineering with softer Asn ligands in place of native Asp_9 in each loop (LanM $3D_9N$).[174]

A slightly higher affinity for Cm^{3+} over Eu^{3+} has also been reported for the EF-hand loops isolated from *Mex*-LanM.[143] Am^{3+} binding to an LBT was shown to be $\sim$6-fold stronger than Nd^{3+} and comparable to smaller Ln^{3+} (Tb^{3+}, Eu^{3+}). A higher ($\sim$10-fold) selectivity for Am^{3+} over Nd^{3+} could be obtained by a modified LBT bearing a Cys_5 residue functionalized with a soft 2-methylene-pyridine group in place of Asp_5.[175]

Daumann and coworkers also demonstrated that An^{3+} ions such as Am^{3+} and Cm^{3+} can replace early Ln^{3+} ions in the catalytic activity of the Ln^{3+}-dependent MDH enzyme and ensure the growth of Ln^{3+}-dependent bacteria in the absence of Ln^{3+} ions.[176]

4.4 Selectivity over d-block metal ions

Despite its relevance for biomedical and bio-metallurgic applications, the selectivity of Ln^{3+}-binding peptides and proteins over d-block metal ions is a largely neglected aspect. Generally, a higher selectivity for Ln^{3+} over d-block metal ions is obtained by leveraging their preference towards O- (carboxylates, carbonyls) over N-donors (*e.g.* histidines), and higher coordination numbers (8–10 *vs.* 4–6). For instance, LanP displayed no binding to Fe^{2+}, Fe^{3+}, or Zn^{2+}.[122] A 3SCC scaffold (MB1-2) engineered with Asn and Asp residues for Ln^{3+} binding, shows $\sim$6-fold higher affinity for Tb^{3+} over Cu^{2+}.[98,177] A remarkably high selectivity for Nd^{3+} ions over Cu^{2+} ($\Delta\log K \sim 6$) and Zn^{2+} ($\Delta\log K \sim 8$) has been reported for *Mex*-LanM at pH 5.[155] On the contrary, EDTA shows higher selectivity for Cu^{2+} over Nd^{3+} (*i.e.* 100-fold higher affinity for Cu^{2+} over Nd^{2+}) and no selectivity between Nd^{3+} and Zn^{2+}, while DTPA has no selectivity between Nd^{3+} and Cu^{2+}, but a $\sim$1000-fold higher affinity for Nd^{3+} relative to Zn^{2+}.[155,173] It is worth noting that EDTA has a higher affinity for Cu^{2+} ($\log\beta^{Cu} = 18.8$) than most Ln^{3+} ions (La^{3+}–Ho^{3+}) and DTPA has a higher affinity for Cu^{2+} ($\log\beta^{Cu} = 21.4$) than the early Ln^{3+} (La^{3+}–Pr^{3+}). Altogether, these data point out that peptides and proteins benefit from a higher selectivity for the whole Ln^{3+} series against d-block metal ions relative to small chelators.

5. Kinetic stability

Beyond thermodynamic parameters, kinetic aspects are also important for a complete characterization of Ln^{3+}-binding peptides and proteins, especially for further applications, such as MRI or Ln recovery (see 6. Applications).

5.1 Lability and inertness: exchange reaction

Due to the shielding by 5s and 5p orbitals, 4f orbitals do not undergo strong ligand field stabilisation, making Ln^{3+} ions kinetically labile.

The lability/inertness is witnessed by the rate of the self-exchange reaction. Such a reaction can proceed according to two extreme pathways: associative or dissociative, corresponding to an increase or a decrease in the coordination number (CN) of the intermediate species, respectively. In turn, this depends on the CN of the starting complexes: for instance, Ln^{3+} complexes with low CN (CN $\leq$ 8, Gd^{3+}–Lu^{3+}) are expected to proceed through an associative pathway with a nine-coordinate intermediate, while those with high CN (CN $\geq$ 9, La^{3+}–Eu^{3+}) by a dissociative pathway with an eight-coordinated intermediate (Fig. 20A).[30] The rates of self-exchange for a certain Ln^{3+} ion depend on the relative stabilities of the eight- and nine-coordinated species for that Ln^{3+}.

Recently, Peacock and coworkers measured the activation parameters for water exchange in the Gd^{3+} complex with a 3SCC scaffold (MB1-1, q = 3) and proposed an associative mechanism.[102] Furthermore, key insight can be deduced from the comparative NMR study of La^{3+} *vs.* Lu^{3+} binding to the LBT3 peptide.[164] In particular, Ln^{3+} binding to LBT3 showed a fast

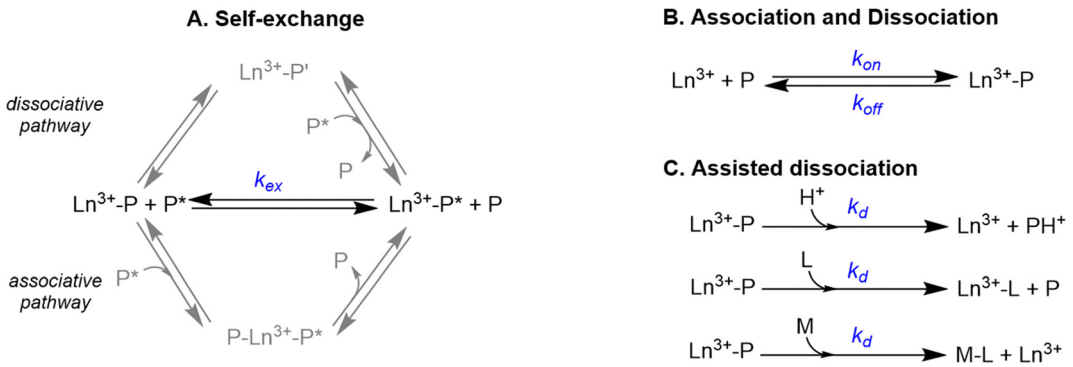

Fig. 20 (A) Self-exchange reaction characterized by the rate constant k_{ex} and related pathways. P and P* are two molecules of the same peptide. In the case of the dissociative pathway, P′ corresponds to peptide P which has some of its binding residues de-coordinated from the Ln. Hence, Ln^{3+} has a lower CN when bound to peptide P′ than P. (B) Association and dissociation reactions with their respective rate constants k_{on} and k_{off}. (C) Simplified scheme of proton-, ligand- and metal-assisted dissociation pathways (rate constants k_d).

Open Access Article. Published on 22 September 2025. Downloaded on 4/1/2026 8:13:17 PM.
This article is licensed under a Creative Commons Attribution-NonCommercial 3.0 Unported Licence.

and slow exchange regime for La^{3+} and Lu^{3+}, respectively,[164] which may be explained through the different structural features of the complexes. Indeed, the La^{3+}–LBT3 complex has CN = 9, with q = 1 and is structurally flexible, hence the decoordination of the weakly-bound (relative to the peptide ligands) H_2O molecule can promote the self-exchange reaction through a dissociative pathway. Instead, the Lu^{3+}–LBT3 complex has CN = 8, with q = 0, and poor solvent accessibility, hindering the possibility of undergoing an associative mechanism.

As a small number of data is available, it is difficult to generalize whether the exchange reaction proceeds *via* a dissociative or an associative mechanism in other Ln^{3+}-binding peptides and proteins, and which parameters would influence the preference between one or the other pathways.

Furthermore, the self-exchange rate k_{ex} can be easily inferred by NMR experiments. For most unfolded or poorly folded peptides, a fast exchange regime characterized by a broadening and shift of the signals was reported at sub-stoichiometric Ln^{3+} : P ratio[76,164,169,178] except for a 2SCC scaffold[95] and an HLH scaffold[18] for which a slow exchange regime was observed. This is in line with the intrinsic lability of Ln^{3+} ions and the absence of constraints induced by the peptide scaffolds.

5.2 Association and dissociation rates

Beyond the exchange rate k_{ex}, key parameters to be defined are the association and dissociation rates, noted k_{on} and k_{off}, respectively. These two parameters are related to the thermodynamic stability constants K according to eqn (9):

$$K = \frac{k_{on}}{k_{off}} \tag{9}$$

The k_{on} value can be measured experimentally by monitoring the appearance of spectroscopic signatures corresponding to the Ln^{3+} complex when formed within the right time scale (milliseconds to hours). Note that such k_{on} values reflect both Ln^{3+} binding to the protein and the induced folding unless the protein is pre-folded in the apo-state. Qualitative estimation of the k_{on} can be deduced for Ln-ADH[19] and TDF-EE N6W,[126,130] for which a long incubation time (hours) was required to load the protein with Ln^{3+}, indicating a slow association rate.

The k_{off} can be then calculated from the k_{on} and stability constant K values, using eqn (9). Indeed, the k_{off} cannot be directly determined experimentally since the release of the Ln^{3+} ion from a polydentate ligand, such as peptides and proteins, to form the fully solvated species is unlikely. Nevertheless, the complete dissociation of a Ln^{3+} from a polydentate ligand can be assisted by (i) protonation of the ligands (proton-assisted dissociation), (ii) capture by another ligand(s) (ligand-assisted dissociation), which can also be the buffer, (iii) trans-metalation by another metal ion (metal-assisted dissociation), or any combination of these three processes. It is worth noting that in these processes, the otherwise disfavoured Ln^{3+} release occurs through the alteration of the system thermodynamics, *e.g.* by weakening the ligand affinity (acid-assisted dissociation) or by inducing metal-transfer/exchange reaction with competing ligand or cations. Thus, although the concept of complex inertness is often equated with that of "assisted dissociation" by language abuse, they refer to intrinsically distinct processes.

Ligand-assisted dissociation rate constants (k_d), which differs from k_{off}, were reported by Falke and coworkers for the complex of Tb^{3+} with an EF-hand protein (galactose-binding protein, GBP) using excess EDTA as the competing ligand.[179] Interestingly, by measuring the dissociation rates of several mutants, these authors showed that the 9th residue of the EF-hand motif acts as a gateway that tunes the kinetics of Ln^{3+} dissociation. Notably, the Glu_9 mutant displayed the slowest dissociation rate ($\sim$0.006 s^{-1}) compared to Asp_9 ($\sim$0.002 s^{-1}) and Asn_9 ($\sim$1 s^{-1}).

The chelator-free k_{off} of Tb^{3+}-bound to *Mex*-LanM ($\sim$0.02–0.05 s^{-1}) was estimated by extrapolation from k_{obs} values obtained by stopped-flow spectrofluorimetry in the presence of different concentrations of EGTA.[63] However, this approach is questionable, since the k_{off} value relative to a dissociative mechanism is inferred from ligand-assisted dissociation rates, for which a different, namely associative, mechanism is at play. Moreover, it is worth noting that, as mentioned for k_{on} values, dissociation rates may also take into account the contribution of protein unfolding induced by Ln^{3+} release.

Daumann and coworkers monitored over time the metal exchange reactions between a pre-formed Eu^{3+}–LanM complex and the other Ln^{3+} ions. Interestingly, equilibration times varied from minutes for the late Ln^{3+} to hours for the early Ln^{3+}, correlating with the size and Lewis acidity of the competing ions.[165]

5.3 Discussion and guidelines

The kinetic aspects of Ln^{3+} coordination by peptides and proteins have been largely neglected and overlooked even though they are important in applications for imaging and Ln recovery. NMR is the method of choice to get a better picture of the dynamics of the system. A simple ^{1}H NMR titration experiment can help gain qualitative insights into the exchange rates using the diamagnetic La^{3+} and Lu^{3+}, and thus determine the exchange regime on the NMR timescale. Comparison with paramagnetic Ln^{3+} can bring additional information on Ln^{3+} coordination site, and even peptides/protein solution structure.

Although it is difficult to predict the kinetic behaviour, based on the results and concepts described above, it is anticipated that the spontaneous dissociation of Ln^{3+} ions from polydentate peptides and proteins is negligible, especially in the case of buried sites within well-folded scaffolds. Notwithstanding, Ln^{3+} dissociation can be triggered upon acidification or the addition of competing ligands or cations. In the case of ligand-assisted dissociation, the presence of weakly bound water molecules in the Ln^{3+} coordination sphere is expected to promote dissociation since its replacement facilitates the formation of ternary intermediate complexes with the competing ligand.

6. Applications

Ln^{3+}-binding peptides and proteins have been employed for a number of applications spanning from luminescence sensing

Open Access Article. Published on 22 September 2025. Downloaded on 4/1/2026 8:13:17 PM.
This article is licensed under a Creative Commons Attribution-NonCommercial 3.0 Unported Licence.

Table 11 Non-exhaustive overview of applications reported for the main types of Ln^{3+}-binding peptide and protein scaffolds

	Scaffold	Luminescence imaging/sensing	MRI	Metal ion separation	Catalysis (reaction)
EF-hand motifs	LBT	X	X	X	
	HLH		X		X (hydrolysis)
	LanM	X	X	X	
Other Ln-binding sites	Cyclic decapeptide		X		
	3SCC		X		
	LanD			X	
	RTX			X	
	TIM barrel				X (alcohols photooxidation)
	ADH or ADH mimics				X (alcohols oxidation)

and magnetic resonance imaging to metal ion separation and catalysis (Table 11). In the following paragraphs, applications in these four major fields will be discussed with respect to the peculiar properties of each type of Ln^{3+}–peptide and protein scaffold.

6.1 Luminescent tags and probes

6.1.1 Ln^{3+} luminescence. Most Ln^{3+} ions display luminescent emission with several advantageous features relative to organic fluorophores and have hence gained interest for applications in optical bioassays, bioimaging and luminescence-guided surgery, as reviewed in ref. 180–185. In particular, they benefit from narrow emission bands and long luminescence lifetimes (μs–ms) at relatively invariant wavelengths, in a range spanning from the visible to the near-infrared (NIR) depending on each Ln^{3+}, and they are not sensitive to photobleaching. Nevertheless, due to the low extinction coefficients (ε = 1–10 M^{-1} cm^{-1}) of Laporte-forbidden f–f transitions, the direct excitation of Ln^{3+} emission is quite inefficient.[30,186,187] This downside is generally circumvented through the so-called antenna effect (Fig. 21).[30,186,187] This is the indirect sensitization of Ln^{3+} *via* (i) the excitation of a suited chromophore – the antenna – to an excited singlet state (S_1), (ii) the energy transfer to an excited triplet state (T_1) *via* intersystem crossing, (iii) the energy transfer to an excited state of Ln^{3+}, from which emission takes place. Even if it is common to observe sensitisation from T_1, the S_1 state can also be the sensitising level.[188] The use of an antenna also warrants larger pseudo-Stokes shifts (difference between the antenna absorption and Ln^{3+} emission wavelengths) than accessible with organic fluorophores.

The efficiency of the energy transfer from the antenna to the Ln^{3+} depends on (i) the energy gap between an antenna triplet state and the Ln^{3+} excited acceptor state, which depends on the antenna–Ln^{3+} couple, and (ii) the antenna–Ln^{3+} distance. Several non-radiative pathways compete with Ln^{3+} luminescence:[189] (i) the antenna fluorescence and phosphorescence emissions, (ii) quenching of the antenna T_1 state by $^3O_2$, (iii) back energy transfer from Ln^{3+} excited state to the antenna triplet state when the energy levels are close, (iv) photo-induced electron transfer (PeT) from the excited antenna to the Ln^{3+}, to which the most reducible Ln^{3+} (Eu^{3+}, Yb^{3+}, Sm^{3+}) are particularly sensitive,[190] (v) non-radiative vibrational de-excitation of Ln^{3+} excited state by high-energy oscillators such as O–H, N–H and C–H groups.[39,40] As a result, Ln^{3+}-bound H_2O molecules quench Ln^{3+} emission. Thus, the type and position of the antenna as well as the hydration number are key parameters influencing the luminescence of Ln^{3+} complexes, including those with peptide and protein ligands.

6.1.2 Type of antenna. Early studies using Tb^{3+} luminescence to investigate Ca^{2+}-binding sites in proteins[54,191] have established that the amino acid tryptophan (Trp) is a suitable antenna for this Ln^{3+}, also showing its superiority relative to Phe and Tyr. Since then, Trp has been by far the most common antenna incorporated in peptide and protein scaffolds to

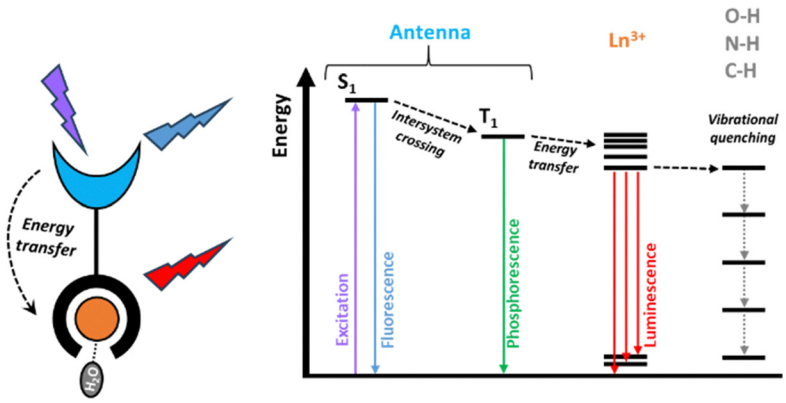

Fig. 21 Scheme of the "antenna" effect: upon irradiation, a chromophore called "antenna" (blue, which can be part of or conjugated to a Ln-chelator, black) is excited to a singlet state (S_1); then, the energy is transferred to an excited triplet state (T_1) *via* intersystem crossing and finally transferred to an excited level of the Ln^{3+} (orange) from which emission takes place. Vibrational de-excitation by high-energy oscillators such as O–H groups is also depicted.

Open Access Article. Published on 22 September 2025. Downloaded on 4/1/2026 8:13:17 PM.
This article is licensed under a Creative Commons Attribution-NonCommercial 3.0 Unported Licence.

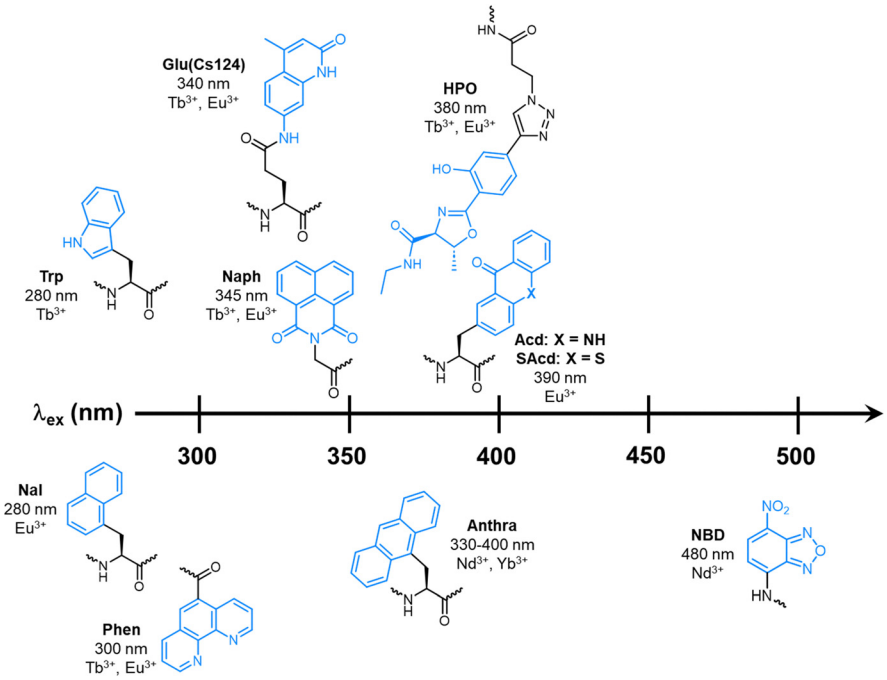

Fig. 22 Antenna amino acids found in Ln^{3+}-binding peptide scaffolds discussed in this review (top) and in peptides with appended polydentate Ln^{3+}-chelators (bottom). The excitation wavelength and the Ln^{3+} ions that each antenna is able to sensitize are indicated. The antenna moieties are highlighted in blue. Abbreviations: Trp, tryptophan; Glu, glutamate; Cs124, carbostyryl-124; Naph, 1,8-naphthalimide; HPO, hydroxyphenol oxazoline; Acd, acridone; Nal, naphthyl-alanine; Phen, phenanthroline; Anthra, anthryl-alanine; NBD, nitrobenzodiazole.

sensitize Tb^{3+} luminescence. Indeed, Trp (λ_{ex} = 280–290 nm) is characterized by a triplet state located 3700 cm^{-1} above the emissive $^5D_4$ state of Tb^{3+}, which makes it an efficient antenna for this Ln^{3+} ion.[192] Trp could also be suitable for Eu^{3+}-sensitisation; however, PeT from Trp quenches Eu^{3+}-emission. PeT has also been described by Horrocks between Trp and Yb^{3+} in the EF-hand protein parvalbumin.[193] While for Eu^{3+} this process competes with Eu^{3+}-emission, it was hypothesized that PeT could be in part responsible for the population of Yb^{3+} excited state and its subsequent emission.

Despite its straightforward incorporation in peptide and protein sequences, Trp is not an ideal antenna for applications in bioimaging, as its excitation wavelength in the UV spectral region challenges applications in samples with high absorption and fluorescence background, such as biological media.[194]

To overcome such limitations, different unnatural antenna amino acids have been introduced. Gunnlaugsson and coworkers incorporated at the N-terminal of an EF-loop isolated from parvalbumin a 1,8-naphthalimide chromophore (λ_{ex} = 345 nm) able to sensitise Tb^{3+} and Eu^{3+} emission (Fig. 22).[169,178] The HPO ligand introduced into 3SCCs scaffolds (see 2.4.1 Coiled coils) was able to sensitize Tb^{3+} and Eu^{3+} upon excitation at 380 nm. Imperiali and co-workers have developed LBTs with unnatural amino acids featuring a carbostyryl-124 (Cs124) or an acridone (Acd) antenna able to sensitize Tb^{3+} (Cs124) and Eu^{3+} (Cs124 and Acd) at longer wavelengths, namely ~340 and 390 nm, respectively (Fig. 22).[195] In particular, the Cs124 antenna was able to sensitise Tb^{3+} better than Trp, while Acd sensitised Eu^{3+} better than Cs124 (Fig. 22).

Lately, Acd and its sulfur-substituted SAcd (Fig. 22) were incorporated into *Mex*-LanM *via* genetic code expansion, achieving long-lived sensitized Eu^{3+} emission upon excitation at 390 nm.[196] Interestingly, SAcd showed to be a more efficient antenna than Acd due to a prolonged triplet state lifetime.

These unnatural antenna amino acids were not able to sensitise the emission from other Ln^{3+} ions including Nd^{3+}, Er^{3+}, Tm^{3+} and Yb^{3+}, which are NIR emitters. Actually, no Ln^{3+}-binding peptide or protein scaffolds have been reported bearing suitable antenna amino acids for NIR-emitting Ln^{3+} ions, which are particularly sensitive to quenching by O–H, N–H and even C–H oscillators. Thus, in addition to a suitable antenna, the design of Ln–peptides and Ln–proteins as NIR emitters will also require avoiding O–H oscillators in their first coordination sphere, and likely also N–H oscillators. To the best of our knowledge, these antenna amino acids are the sole used in Ln^{3+}-binding peptide and protein scaffolds.[8] Other antennae were described in peptide and proteins functionalised with polydentate Ln^{3+}-chelators such as EDTA and DOTA as reviewed in part in ref. 23. In these cases, the antenna has been introduced through either (i) ligand derivatization, often with conjugated pyridine or picolinate groups,[197–199] or (ii) unnaturall amino acids (Fig. 22), including naphthalene (for Eu^{3+}, λ_{ex} = 280 nm),[200] NBD (for Nd^{3+}, λ_{ex} = 480 nm),[201,202] anthracene (for Nd^{3+} and Yb^{3+}, λ_{ex} = 330–400 nm)[203] and phenanthroline (for Tb^{3+} and Eu^{3+}, λ_{ex} = 300 nm).[204] Similarly to HPO, phenanthroline served as both Ln^{3+} ligand and antenna. Such an Ln^{3+}-coordinating antenna is generally preferable because its proximity to the ion enhances the energy transfer efficiency.

Open Access Article. Published on 22 September 2025. Downloaded on 4/1/2026 8:13:17 PM.
This article is licensed under a Creative Commons Attribution-NonCommercial 3.0 Unported Licence.

6.1.3 Position of the antenna. As the Ln^{3+}–antenna distance is critical to achieve efficient sensitization, antennas are introduced in close proximity to the metal-binding site. For instance, in 3SCC scaffolds (Table 5) Trp has been mostly introduced within the two Ln^{3+} binding Asn and Asp residues of each strand (–NEWKD–).[98]

Szabo and coworkers have thoroughly investigated how the position of aromatic amino acids (Trp, Phe or Tyr) within the EF-hand motif sequence influences Tb^{3+} emission.[66] In particular, they compared the excitation and emission spectra of Tb^{3+} bound to EF-hand peptides containing aromatic amino acids in positions 2, 4, 7 or 10. Very interestingly, they found that, regardless of which amino acid occupied positions 2, 4 and 10, the amino acid in the 7th position is responsible for Tb^{3+} sensitization due to its closer distance to the ion (~5 Å). For instance, despite Phe and Tyr having a lower extinction coefficient than Trp, Tb^{3+} was mainly sensitized by either Phe or Tyr in the 7th position even when Trp was simultaneously present in the 2nd position. Moreover, the authors reported a favourable impact of Tyr in the 2nd and 4th, but not 10th, position on the Tb^{3+} emission in peptides having Trp in the 7th position. In particular, the results suggested that this occurs thanks to an energy transfer between excited Tyr and Trp, which in turn sensitises Tb^{3+} emission. Based on these studies, Trp_7 has been incorporated as the Tb^{3+} sensitizer in many EF-hand motif scaffolds, including LBTs[72,73] and *Mex*-LanM mutants.[63] The 7th loop position has also been used to incorporate unnatural Cs124 and Acd antenna amino acids in LBTs[195] and *Mex*-LanM (in the latter case after screening of 42 incorporation sites).[196] Zondlo and coworkers also showed that Tb^{3+} emission can be sensitized using Trp at the 8th position of EF-loop-like peptides.[148]

6.1.4 Hydration number. As already mentioned, Ln^{3+}-bound water molecules quench Ln^{3+}–luminescence, which is used to determine Ln^{3+} hydration number. This is why, for instance, the coordination sphere of luminescent Tb^{3+}–LBT complexes was optimized to achieve q = 0 (see 2.2.2 Lanthanide-binding tags). The effect of the hydration number is also proven by the correlation between the emission intensity of Ln^{3+} bound to different 3SCC scaffolds (MB1-n series, n = 1–4) and their q values (0, 2 or 3) (see 2.4.1 Coiled coils).[99]

6.1.5 Probe design and selected applications. A simple application of emissive Ln^{3+}-complexes is as luminescent tags attached to a (bio)molecule or receptor. In this regard, LBTs have been developed as encodable luminescent tags that can be easily conjugated to proteins *via* recombinant expression and applied, for instance, to the study of protein–protein interactions by luminescence resonance energy transfer (LRET).[139,205] Recently, LanM-Acd mutants conjugated with Affibodies and complexed with Eu^{3+} were used as a secondary antibody reagent for immunofluorescence staining.[196]

Besides, peptide and protein scaffolds with suitable antennae may serve as luminescent probes for Ln^{3+} ions. For instance, a *Mex*-LanM Trp mutant (T90W) has been successfully employed to measure Tb^{3+} in acid mine drainage at very low pH (~3),[63] while LanM-Acd mutants were applied for Eu^{3+} detection in cell culture.[196]

Alternatively, Walker and coworkers reported on the design of fluorescent proteins with a high concentration of negative charges at their surface for the detection of Ln^{3+} (Ln = Sm, Eu, Tb, Dy, Tm, Yb) by LRET in the micro- to millimolar concentration range.[206] Instead of exciting an antenna, it is the Ln^{3+} that is excited and transfers its energy to the fluorescent proteins, which resulted in a twofold higher fluorescence intensity and longer emission lifetimes.

As reviewed in ref. 23 and 180, Ln^{3+}-based responsive probes, whose luminescent signal changes upon the interaction with a given target, can be conceived based on the above-mentioned factors influencing Ln^{3+} luminescence, such as (i) chemical modifications of the antenna, (ii) variation of the Ln^{3+}–antenna distance, for instance through conformational changes induced upon target-binding or *via* proteolytic cleavage, and (iii) modification of the Ln^{3+} coordination sphere and hydration number.

These principles have been used to develop several responsive probes based on peptides with appended Ln^{3+}–chelator complexes.[23] For instance, Vazquez and coworkers designed a peptide probe that folds upon RNA binding, inducing the coordination of a phenanthroline antenna to an appended Tb^{3+}–EDTA complex.[204] Similarly, Sénèque and coworkers developed Zn^{2+}-[201] and RNA-responsive[207] peptide probes based on conformational changes that decrease the distance between the antenna and a Ln^{3+}–DOTA complex attached to the peptide. Exploiting the distinct emission bands of Ln^{3+} couples such as Tb^{3+}–Eu^{3+} in the visible and Nd^{3+}–Yb^{3+} in the NIR, the group of Sénèque also developed ratiometric probes (*i.e.* based on the ratio between two signals) introducing two suitably positioned Ln^{3+}–chelator complexes.[200,203] In order to synthesize such regio-selectively hetero-metallated complexes, they used native chemical ligation to assemble two peptides functionalized with different Ln^{3+} complexes. Of note, this strategy relies on the kinetic inertness of the Ln^{3+}-complexes grafted on the peptides and has never been applied so far on peptide scaffolds with "intrinsic" Ln^{3+}–binding sites.

Lately, LanM-Acd mutants have been developed as protease sensors based on the impairment of the antenna effect upon protein cleavage. To this end, protease recognitions sequences were incorporated in suited position with the LanM scaffold.[196]

Pazos and coworkers developed peptides with appended Tb^{3+}–DO3A complex (Fig. 15) responsive to (i) Ser phosphorylation, based on a decrease of the hydration number,[208] and (ii) to Tyr nitration, relying on the quenching of Tb^{3+} emission by 3-nitro-Tyr.[209] Quenching of Tb^{3+} emission was also exploited in the design of Cu^{2+}-selective peptide probes.[194,210]

Zondlo and coworkers also developed Tb^{3+} complexes with EF-hand-like peptides (Table 10) responsive to (de)phosphorylation of Tyr, Ser and Thr,[144,145,148] Tyr nitration[146] and Cys oxidation.[147,211] In particular, Cys, Tyr, Ser or Thr residues were introduced in place of Asp or Glu residues within EF-loops (Table 10), drastically reducing Tb^{3+}-binding ($\log K_{app} < 4$), while their derivatization with phosphate or sulphinyl groups restored a $\log K_{app} \approx 4$–5. Hence, in this case, the response was mainly due to a change in the metallopeptide affinity upon amino acid modification.

Open Access Article. Published on 22 September 2025. Downloaded on 4/1/2026 8:13:17 PM.
This article is licensed under a Creative Commons Attribution-NonCommercial 3.0 Unported Licence.

Table 12 Properties of Gd^{3+}-complexes relevant for MRI applications

Scaffold	Peptide/protein	MW (kDa)	q^a	τ_R (ns)	$\tau_m{}^b$ (ns)	r_1 (mM^{-1} s^{-1})	r_2 (mM^{-1} s^{-1})	Magnetic field (T)	Ref.
DOTA	n/a	~0.5	1	~0.08	244	4.3	5.7	7	215
				n/a	n/a	4.7	n/a	0.47	216
DTPA	n/a	~0.5	1	~0.06	300	n/a	n/a	n/a	215
				n/a	n/a	4.7	n/a	0.47	216
				n/a	n/a	3.5	n/a	1.4	77
				n/a	n/a	5.4	8	1.5	217
				n/a	n/a	4.2	6.8	3	217
				n/a	n/a	5.1	9.4	7	218
HLH	P3W	~4	2	n/a	n/a	16.2	n/a	0.47	77
						21.2	n/a	1.4	
LBT	m-sSE3	~2	1	n/a	n/a	5.5	n/a	11.75	60
	sSE3		0	n/a	n/a	1.2	n/a	11.75	60
dLBT	dSE3	~4	0.08	n/a	n/a	5.9	n/a	11.75	60
dLBT–protein	dSE3-Ubiquitin	~12	0.08	n/a	n/a	2.3	n/a	11.75	60
	q-dSE3-Ubiquitin		1	n/a	n/a	4.2	n/a	11.75	60
	xq-dSE3-Ubiquitin		0; 1	n/a	n/a	5.0	n/a	11.75	60
Cyclic decapeptide	PA	~1.3	2	0.4	n/a	~30	~40	4.7	41 and 219
						~20	~35	9.4	
						~20	~35	11.75	
3SCC	MB1-1	~12	3.1	7	1.56	10	89.3	7	102
						64.3	87.9	1	
	MB1-1 (2W)		0	n/a	n/a	3.9	24.2	7	100
	MB1-2		0	n/a	n/a	4.2	21.3	7	99 and 100
	MB1-3		0	n/a	n/a	4	20.9	7	99
	MB1-4		2	n/a	n/a	7.5	37.9	7	99 and 100
	MB1-1L	~15	3.7	10	n/a	10.9	81.8	7	102
						67.4	96.5	1	
Proteins	CA1.CA2	~12	2	9.1	n/a	117	129	1.5	217
						48	88	3	
						6	50	9.4	
	ProCA32	~12	0.5	n/a	n/a	33.4	44.6	1.4	218
						21.9	56.9	4.7	
						18.9	48.6	7	
	LanM	~12	2	n/a	n/a	12.1	17	3	220
	LanND	~12	2	n/a	n/a	13.2	25.1	3	
						6.9	31.2	7	

[a] Values obtained by the measurement of Tb^{3+} or Eu^{3+} luminescence lifetimes. [b] Values measured at 298 K.

6.2 Magnetic resonance imaging

Clinical contrast agents (CAs) for magnetic resonance imaging (MRI), reviewed by Caravan and coworkers in ref. 212, are mostly Gd^{3+}-complexes with polyaminocarboxylate chelators, such as DOTA and DTPA (Fig. 16). Gd^{3+}-based CAs (GBCAs) enhance image contrast by shortening the longitudinal (T_1) and transverse (T_2) relaxation time of proximal water protons, to an extent that depends on their longitudinal (r_1) and transverse (r_2) relaxivity, as defined by eqn (10):

$$\frac{1}{T_i^{\text{obs}}} = \frac{1}{T_i^0} + r_i[\text{Gd}] \quad i = 1, 2 \tag{10}$$

where $1/T_i^0$ is the inherent relaxation rate of the tissue and $1/T_i^{\text{obs}}$ is the relaxation rate in the presence of the GBCA. Of note, the relaxivity (r) depends on the external magnetic field strength (Table 12). Clinical MRI scanners currently use low magnetic fields (~0.5–3 T), while higher fields (up to ~11.7 T) are used for research purposes. Nevertheless, in order to improve signal-to-noise ratio and spatial resolution, clinical MRI is progressively moving towards higher field strength.[213]

In order to increase MRI sensitivity, reduce the injected GBCA dose and hence limit toxic side-effects, GBCAs with higher relaxivity are currently sought.[212] The approaches developed to achieve this goal have been reviewed in ref. 214. The main molecular factors affecting the inner-sphere relaxivity of GBCAs are the hydration number q, the mean residency time τ_m of Gd-bound water and the rotational correlation time τ_R (Fig. 23).[212] Hereafter, these factors are discussed with respect to the Gd^{3+} complexes with peptides and proteins that have been investigated as GBCAs (Table 12).

6.2.1 Hydration number. Inner-sphere relaxivity is directly proportional to the hydration number q, and indeed commercial GBCAs feature one or two water molecules in the coordination sphere. To meet this requisite, Imperiali and coworkers developed LBTs with q = 1 (m-sSE3 and q-dSE3-Ubiquitin, Table 12), which showed similar relaxivity relative to commercial GBCAs at high magnetic field (11.75 T).[60] As already mentioned above (2.2.2 Lanthanide-binding tags), the increase of q from 0 to 1 was accomplished by mutating Glu_9 to Asp_9, and it was accompanied by a nearly 5-fold increase in longitudinal relaxivity (Table 12).

Peacock and co-workers have investigated the relaxivity of Gd^{3+}–3SCC scaffolds, showing a significant dependence on the

Open Access Article. Published on 22 September 2025. Downloaded on 4/1/2026 8:13:17 PM.
This article is licensed under a Creative Commons Attribution-NonCommercial 3.0 Unported Licence.

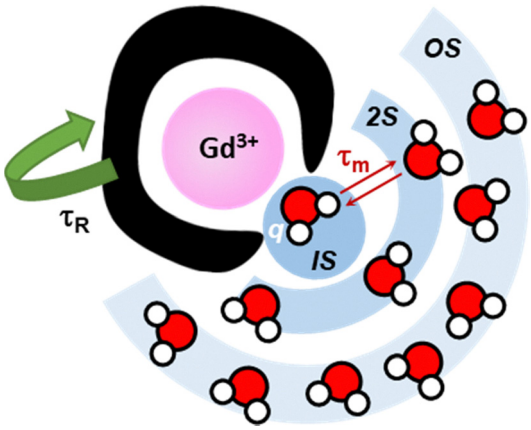

Fig. 23 Scheme of a GBCA and graphical description of the parameters that influence its relaxivity, including inner-sphere (IS) contributions (hydration number, q; water residency time, τ_m; rotational correlation time, τ_R) as well as second (2S) and outer (OS) sphere effects.

location of the Ln^{3+}-binding site along the coiled coil and the second sphere layer, which both affect the hydration number (see 2.4.1 Coiled coils).[98–100,102,104] Remarkably, scaffolds with high hydration numbers, such as MB1-1 (q = 3), MB1-4 and the recently reported LanM derivative LanND (q = 2), display significantly higher relaxivity compared to clinical GBCAs, especially at low clinical field (1 T, Table 12).

6.2.2 Rotational correlation time. The rotational correlation time, τ_R, reflects the rate of molecular tumbling. Of note, the impact of τ_R on the relaxivity depends on the strength of the magnetic field, as illustrated in Fig. 24 by the nuclear magnetic relaxation dispersion (NMRD) profiles (*i.e.* relaxivity profiles as a function of the magnetic field strength) for different τ_R values (A) short ~0.1 ns; B) intermediate; C) long, ~10 ns).[212] In general, the relaxivity increases with increasing τ_R at low magnetic fields (< ~1 T in Fig. 24), whereas at higher fields, the relaxivity increases with increasing τ_R up to a threshold beyond which the relaxivity decreases upon further τ_R increase.

To improve the relaxivity, a τ_R increase can obtained by increasing the molecular weight and the rigidity of GBCAs.[214]

For instance, the Gd^{3+} complex with the rigid cyclodecapeptide scaffold PA (see 2.3.1 Cyclic decapeptide) showed remarkably high relaxivity (20–40 mM^{-1} s^{-1}, Table 12) at high magnetic fields (4.7–11.75 T) thanks to a medium-range molecular weight (~1.3 kDa) implying an optimal $\tau_R \approx 0.4$ ns.[41]

Besides, Yang and co-workers have developed protein-based CAs by engineering protein scaffolds with Gd^{3+}-binding sites, achieving much higher relaxivity relative to small GBCAs at both low and high fields (Table 12).[217,218] In CA1.CD2 (~12 kDa), where a *de novo* designed rigid Gd^{3+}-binding site was engineered into a compact CD2 (a cell adhesion protein) domain, the enhanced relaxivity relative to small GBCAs is mainly the result of a higher hydration number (q = 2) and a remarkably longer τ_R (~9 ns) relative to commercial GBCAs.[217] It is worth noting that the local rigidity of the Gd^{3+} complex, and not only the molecular weight, is crucial to achieving high relaxivity. As an example, Yang and coworkers also showed that Gd^{3+} bound to a CD2 domain engineered with a flexibly conjugated EF-loop from CaM showed a relaxivity comparable to that of small commercial GBCAs (~3.4 mM^{-1} s^{-1} at 3 T).[217] Analogously, the mere conjugation of double LBT (dLBT) on a protein scaffold (ubiquitin) did not improve their relaxivity (Table 12).[60]

A long τ_R (7–10 ns) was also reported for Gd^{3+}–3SCC complexes;[102] however, it is noteworthy that lengthening the coiled coil from five (MB1-1, ~12 kDa) to six heptads (MB1-1L, ~15 kDa) and the consequent τ_R increase had negligible impact on the relaxivity (Table 12), suggesting that the tumbling rate is not a limiting factor for such scaffolds.

6.2.3 Water residency time. The relaxivity has roughly a bell-shaped dependence on the water residency time (τ_m), as the water exchange must be neither too fast nor too slow to maximize the relaxation of bulk water molecules. Similarly to the case of τ_R, the impact of τ_m on the relaxivity also depends on the strength of the magnetic field: at the higher fields, the optimal relaxivity can be attained by a broad range of τ_m, while at low fields the optimal relaxivity can be obtained only for a narrow range of τ_m.[212] Of note,

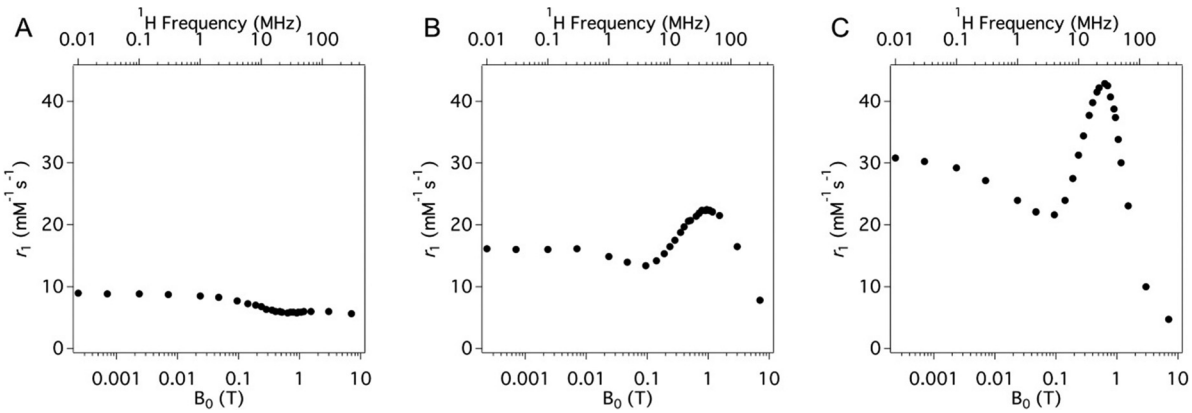

Fig. 24 Experimental ^{1}H NMRD profiles showing the dependence of the relaxivity (per Gd^{3+} ion) as a function of the magnetic field strength for Gd-DTPA derivatives with short (A, ~0.1 ns), intermediate (B), and long (C, ~10 ns) rotational correlation times. Reprinted with permission from ref. 212. Copyright 2019 American Chemical Society.

Open Access Article. Published on 22 September 2025. Downloaded on 4/1/2026 8:13:17 PM.
This article is licensed under a Creative Commons Attribution-NonCommercial 3.0 Unported Licence.

the impact of τ_m on the relaxivity tends to be negligible for small molecules with fast tumbling, but it can be important for complexes with slow tumbling such as bigger peptides and proteins.[212] Peacock and coworkers have recently demonstrated that a short water residency time is the predominant factor by which Gd^{3+}–3SCC complexes achieve high relaxivity.[102,104] In particular, the authors measured an extremely fast water exchange rate (τ_m = 1.56 ns), comparable to that of free Gd^{3+} in water (τ_m = 1.02 ns) and much faster relative to that of small GBCAs ($\tau_m \approx$ 240–300 ns, Table 12).[102]

6.2.4 Outer-sphere relaxivity. Besides the inner-sphere (IS) relaxivity, second- (2S) and outer-sphere (OS) contributions exist involving hydrogen-bonded water or exchangeable protons in the second coordination sphere, and water molecules that diffuse close to the Gd^{3+} centre, respectively. Remarkably, such OS effects account for about 40% of the overall relaxivity of commercial GBCAs.[212] Moreover, note that the relaxivity of Gd^{3+}-complexes with no inner-sphere water molecules (q = 0) basically stems from 2S/OS contributions.

This is the case, for instance, of some Gd^{3+}–3SCC scaffolds (*e.g.* MB1-2 and MB1-3) that showed a relaxivity comparable to that of commercial GBCAs at high field (7 T), despite having q = 0 (Table 11). Indeed, the authors hypothesized that this could be mainly related to an OS mechanism involving hydrogen bonding and proton exchange networks between the peptide surface and bulk water.[99]

Delangle and coworkers measured the IS and OS relaxivities of the Gd^{3+}–PA complex and indirectly determined the 2S contribution, which accounts for about 25% of the total relaxivity.[41,219] By means of MD simulations and the fit of the experimental data with appropriate models, the authors provided a molecular interpretation of the 2S contribution, identifying three 2S water molecules with a high residence time ($\approx$1 ns).

Important 2S and OS contributions were also evidenced for the protein-based GBCAs reported by Yang and coworkers.[218]

6.2.5 Discussion and perspectives. Although an exhaustive comparison among the magnetic properties of different Ln^{3+}-binding peptide and protein scaffolds is prevented by the different conditions in which relaxivity data were collected, the highest relaxivity is observed (i) at low fields (0.47–3 T), for large and compact protein scaffolds with long τ_R ($\sim$10 ns), such as some 3SCCs and CA1.CA2, and (ii) at high fields (7–11.75 T), for small rigid scaffolds with intermediate τ_R ($\sim$0.5–2 ns) and important 2S/OS contributions, such as PA. This trend, which is consistent with the dependence of relaxivity on τ_R and the magnetic field strength (Fig. 22), points to the fact that, while large protein scaffolds could be suitable for current clinical (low-field) MRI settings, smaller scaffolds will meet the future need (see above) for GCBAs applicable at higher field. The analysis of the relaxivity data reported indicates that GBCAs based on peptide and protein scaffolds can benefit from higher relaxivity than current clinical GBCAs. This is due to their longer τ_R (related to higher molecular weight and/or rigidity) as well as important second- and outer-sphere contributions mediated by the peptide surface (*e.g.* hydrogen bonding networks). It is also worth noting that protein-based GBCAs such as ProCA32 and LanND have enhanced molecular relaxivity ($\sim$40–50 mM^{-1} s^{-1} at 7 T), as they bind two and four Gd^{3+} ions, respectively.

However, most peptide and protein scaffolds display a lower affinity for Gd^{3+} ($\log K_{app} \leq \sim 13$, see 3. Thermodynamic stability) than currently used GBCAs ($\log {}^{c}K \approx$ 15–19 at pH 7.4[212]) and their kinetic inertness has been poorly explored, challenging their *in vivo* applications. Nevertheless, some protein-based GBCAs, including ProCA32 and LanND-Gd benefit from higher selectivity against physiological metal ions (*e.g.* Ca^{2+}, Cu^{2+}, Zn^{2+}) than small chelators (see 4.4 Selectivity over d-block metal ions), and showed good biocompatibility, resulting as a promising alternative as next-generation GBCAs. Indeed, ProCA32 showed a half-life of $\sim$4 hours in the blood plasma of mice, which increased to $\sim$10 hours upon PEGylation. At 14 days postinjection of ProCA32, a 3- to 10-fold lower amount of Gd^{3+} was detected in different organs compared to the administration of Gd bound to a DTPA derivative.[221] Hence, ProCA32 has been conjugated with different targeting moieties, including PSMA (prostate-specific membrane-associated antigen), CXCR4 (chemokine receptor 4) and a collagen-targeting peptide, to selectively target prostate cancer, liver metastasis or lung fibrosis.[222–226] Similarly to clinical GBCAs, LanND concentration in mice blood dropped below detection level within 1 hour, and renal clearance was observed within 3 hours after LanND injection. Moreover, LanND did not show cellular and neural toxicity and did not elicit an evident immune response. Based on these favourable properties, LanND allowed the high-resolution visualization of brain vessels and the monitoring of kidney dysfunction in mice.[220]

Beyond the research of safer and more sensitive GBCAs, there is a growing interest in the development of responsive GBCAs, which have been reviewed in ref. 227–231. For instance, GBCAs responsive to the pH, molecular targets (cations, anions, metabolites, nucleic

	La	Ce	Pr	Nd	Pm	Sm	Eu	Gd	Tb	Dy	Ho	Er	Tm	Yb	Lu
Batteries	X	X													
NdFeB and SmCo Magnets			X	X		X		X		X					
Phosphors/fluorescent lamps	X						X	X	X						
Catalysis, refinery	X	X													
Medecine								X							X

Fig. 25 Overview of the most developed Industrial uses of Ln: rechargeable batteries, permanent magnets, lightings, catalysis and refinery, and medicine. Pm is a radioactive element and does not occur in Nature.

Open Access Article. Published on 22 September 2025. Downloaded on 4/1/2026 8:13:17 PM.
This article is licensed under a Creative Commons Attribution-NonCommercial 3.0 Unported Licence.

acids), biomarkers, or enzyme activity can be designed based on a change of the relaxivity, that is on the variation of hydration number (q-based) or the tumbling rate (τ_R-based), or both.

In the early 2000s, the HLH scaffold P3W (see 2.2.3 Chimeric helix-loop-helix motifs) was the first, and currently unique, Ln^{3+}-binding peptide investigated as a responsive GBCA. Gd^{3+}–P3W showed a 4- to 6-fold higher relaxivity than Gd^{3+}–DTPA at low clinical magnetic fields (Table 11), as a result of higher hydration number (q = 2) and slower tumbling rate, whose further decrease upon DNA binding yielded a ~100% relaxivity increase.[77] Lately, Sénèque and coworkers have also developed Zn^{2+}-responsive peptides with appended Gd^{3+}–DOTA/DO3A derivatives that show a Zn^{2+}-dependent relaxivity increase based on a change of the system rigidity and/or hydration number upon Zn^{2+} binding.[232,233] These examples illustrate how responsive peptide/protein-based GBCAs could be designed.

6.3 Ln recovery and separation using Ln-binding peptides and proteins

6.3.1 Challenges in REE separation. Rare earth elements, which include Ln, Y, and Sc, have become indispensable for medicine (Gd, Lu), and green energies as they are essential elements of permanent magnets and rechargeable batteries (La, Ce, Pr, Nd, Sm, Gd, Dy), lightings (La, Eu, Gd, Tb, Y), and catalysis and refinery (La, Ce) as reviewed in ref. 234 and 235 (Fig. 25). Even Er, Tm and Yb, which are not used on a large scale, find industrial applications. Er is used in silica-glass fibres for communications and in laser for medical applications; Tm is also used in laser for laser surgery, ^{170}Tm radionuclide is used in portable X-ray sources, and so is ^{169}Yb.[235]

The REE market is dominated by China, which supplies 98% of REE used in the EU.[2] Due to the expected increasing demand for REE in the coming years and to the lack of high concentrated REE mining sites in Europe, REEs have been identified as critical elements by the EU.[2,235] Thus, there is a strong interest in developing REE recovery technologies from secondary sources, such as the enormous amounts of waste from electrical and electronic equipment generated each year (WEEE 1–30% wt REE).[234] Additionally, sources with low concentrations of REE such as phosphogypsum (0.01–2% wt REE), red mud (500–2500 ppm REE), mine tailings (3–5% wt REE), coal ashes (0.1–1% wt REE), or acid mine drainages (200–900 μg L^{-1} REE) are available in such amounts that the total content of REE they contained could be worth exploiting. The industrial and economic feasibility of the valorisation of such wastes was discussed in ref. 236.

Beyond economic and geopolitical aspects, it is urgent to develop new and more sustainable REE recovery technologies to limit damages caused by mining and reduce the greenhouse gas emissions and the detrimental impact on the environment of actual processes that rely heavily on pyrometallurgy (high energy consumption, release of toxic gases, volatile metals and dust) and hydrometallurgy (use of strong acids such as HCl, HNO_3, or H_2SO_4; solvents such as kerosene or hexane; large amount of liquid wastes and sludges; risk of heavy metal pollution, including by radionuclides).[3] The separation of REE is an additional challenge, which is performed by multiple separation cycles involving liquid/liquid extraction, or precipitation, and relying on the use of organic ligands.[14,237]

In this context, biometallurgy is emerging as a sustainable alternative that could reduce the energy consumption, waste production, and volumes of strong acids and solvents used, even though it has not yet been translated at the industrial scale.[14,238–243] This approach relies on the use of micro-organisms or biomaterials for the (selective) recovery of critical metal ions and is particularly suited for low-grade REE feedstocks with low REE concentrations.

Several bio-inspired strategies have been investigated for the recovery of REE from secondary sources which were discussed in recent reviews: *(i) non-modified microorganisms:* microorganisms were used either for biosorption of REE on their surface, or for their (active) bioaccumulation as reviewed in ref. 239–243. Notably, the Ln-dependent methylotrophic strain *M. fumariolicum* SolV was recently described for its ability to recover REE from various low-grade sources;[244] *(ii) display of REE-binding motifs:* micro-organisms were also modified to display Ln^{3+}-binding peptides on their surface in order to improve REE biosorption, which was recently reviewed.[15,242] Examples include LBT displayed on phages,[245,246] or *E. coli*,[154,247–251] and LanM displayed on *Y. lipolytica* and *E. coli*;[252,253] *(iii) Ln-binding peptides and proteins:* Ln^{3+}-binding peptides and proteins were also used directly for recycling (Table 13) as reviewed in ref. 15, 241, 242 and 254 and discussed in more detail below.

6.3.2 REE recovery strategies. The development of recovery strategies based on Ln-binding peptides and proteins has been done using EF-hand scaffolds, as well as other types of scaffolds.

Joshi and coworkers used LBT to develop filters for REE recovery from dilute acid wash.[255] They genetically engineered a Curli fibre produced in *E. coli* biofilm and known to form amyloid fibres extracellularly, to fuse it with two or four repeats of an LBT sequence. Following a similar strategy, Kaplan and co-workers developed filters based on silk nanofibrils (SNF) functionalized with LBT peptides (Fig. 26), either by chemical coupling or by genetically fusing LBT to a silk-elastin-like protein (SELPS).[256]

Following the discovery of LanM, their potential for the recovery of REE (including Y^{3+} and Sc^{3+}) was investigated mostly with *Mex*-LanM, and more recently with *Hans*-LanM (Table 13). The strategies employed relied on size-exclusion filtration, on LanM-functionalised agarose beads,[257] on functionalized magnetic nanoparticles (MNP-LanM, Fig. 27),[260] on polymeric membranes functionalized with LanM-derived peptides,[261] and on liquid–liquid phase separation made by fusing LanM to a thermo-responsive genetically encoded polypeptide RELP.[258]

Cotruvo and coworkers investigated the use of LanD for large Ln-separation.[125] They hypothesized that by combining mutations of LanD to lower the affinity of its monomer for Ln^{3+} (E75Q) and favour the dimer formation by removing repulsive electrostatic interactions (E78A), they could obtain a dimer that preferentially binds Pr^{3+} and Nd^{3+} over La^{3+} and Ce^{3+}.

Open Access Article. Published on 22 September 2025. Downloaded on 4/1/2026 8:13:17 PM.
This article is licensed under a Creative Commons Attribution-NonCommercial 3.0 Unported Licence.

Table 13 Strategies based on Ln-binding peptides and proteins for REE recovery. Details are given regarding the scaffolds used, the pH range in which REE^{3+}-binding was performed, the composition and pH of the solutions from which REE were recovered, the sorption/desorption strategies employed, and if intra-REE selectivity was achieved. n.d.: not determined; n/a: not applicable

Scaffold	pH range	REE^{3+} Competing metal ions (source, pH)	Sorption (S) Desorption (D)	Intra-REE selectivity	Ref.
LBT	> 5	Ln Al, Ca, Cu, Fe, Ni (mine tailings, pH 7)	S: filtration on functionalised fibres D: HNO_3, pH 2	Yes	255
	~4	Tb Ca or Cu or Fe or Zn —	S: filtration on functionalised fibres D: HCl, pH 1.7	n.d.	256
RTX	> 0.5	Nd, Dy Fe, Co (NdFeB magnet solution, pH 6)	S: filtration on 3 kDa cutoff ultrafilter D: n/a	n.d.	129
LanM	> 2.5	Sc, Y, Ln Li, Be, Na, Mg, Ca, Sr, Al, Si, Mn, Fe, Co, Ni, Cu, Zn, U (lignite leachate, pH 3.7)	S: filtration on 3 kDa cutoff ultrafilter (*Mex*-LanM) D: n/a	no	155
	> 2.4	Sc, Y, Ln Li, Na, K, Rb, Mg, Ca, Sr, Ba, Al, Si, Pb, V, Mn, Fe, Co, Ni, Cu, Zn, Se, Th, U (coal fly ash leachate, pH 5)	S: filtration on functionalized agarose beads (*Mex*-LanM) D: pH steps (HCl, pH 2.3, then pH 1.5)	Yes	257
	—	Sc, Y, Ln — (coal combustion, mine tailings, pH 3)	S: filtration on functionalized agarose beads (*Mex*-LanM) D: two-cycle process: 1. Malonate, then pH ramp (2.3-2.1-1.9), 2. Citrate, then pH 1.5	Yes	167
	> 2	Y, Ln Mg, Na, Ca (coal fly ash leachate, pH 4.5)	S: liquid–liquid phase separation (*Mex*-LanM) D: phosphate-citrate buffer, pH 2.2	Yes	258 and 259
	> 3	Sc, Y, Ln Li, Na, K, Rb, Mg, Ca, Ba, Al, Si, Pb, V, Mn, Fe, Co, Ni, Cu, Zn, As, Se, Cs (coal fly ash leachate, pH 5)	S: functionalised magnetic nanoparticles (*Mex*-LanM) D: HCl, pH 1.7	n.d.	260
	—	Dy, Nd — (pH 5)	S: filtration on functionalized agarose beads (*Hans*-LanM, *Hans*-LanM-R100K) D: 1. Malonate, 2. HCl, pH 1.5	Yes	62
LanD	n.d.	La, Ce, Pr, Nd — (pH 6)	S: filtration on 10 kDa cutoff ultrafilter (LanD-E75Q/E78A) D: n/a	Yes	125

Still with the aim of developing a method for REE recovery, Banta and coworkers proposed to use the RTX protein, which can bind up to 8 lanthanides at pH 5.5.[129]

6.3.3 pH sensitivity. As stressed above (see 3.4 Effect of the pH), the impact of pH on Ln^{3+}-binding is generally an overlooked feature. Nonetheless, because applications for recovery require working with acidic REE sources, the pH sensitivity of some of the peptides/proteins used or their derived materials has been investigated.

LBT-based fibres displayed a similar pH-sensitivity than observed in solution.[255] The fibres could bind Tb^{3+} down to pH 5, and their Tb^{3+}-sorption capacity was decreased to the level of non-functionalized fibres at pH 3. Park and Cotruvo showed that *Mex*-LanM functionalised agarose beads retained their ability to bind REE at pH 3,[257] which was consistent with *Mex*-LanM capacity to bind Ln^{3+} down to pH 2.5 in solution.[155] RTX is the protein that seems to be the more tolerant to pH as it retains some Ln^{3+}-binding capacity at pH < 1.5. However, the proteins precipitate at low pH, which complicated the analysis.

Although the different scaffolds described to date present various pH-sensitivity, most of them were assayed for their ability to bind Ln on slightly acidic solutions (pH 4–7, Table 12) corresponding to REE sources obtained from mine tailings, or leachates. Desorption of REE was only investigated for LBT- and LanM-based materials and could be achieved with acidic solutions (HCl, HNO_3) at pH < 2. This is a consequence of the protonation of Ln^{3+}-binding amino acids (*e.g.* Asp, Glu), which results in a lower affinity for Ln^{3+}.

Open Access Article. Published on 22 September 2025. Downloaded on 4/1/2026 8:13:17 PM.
This article is licensed under a Creative Commons Attribution-NonCommercial 3.0 Unported Licence.

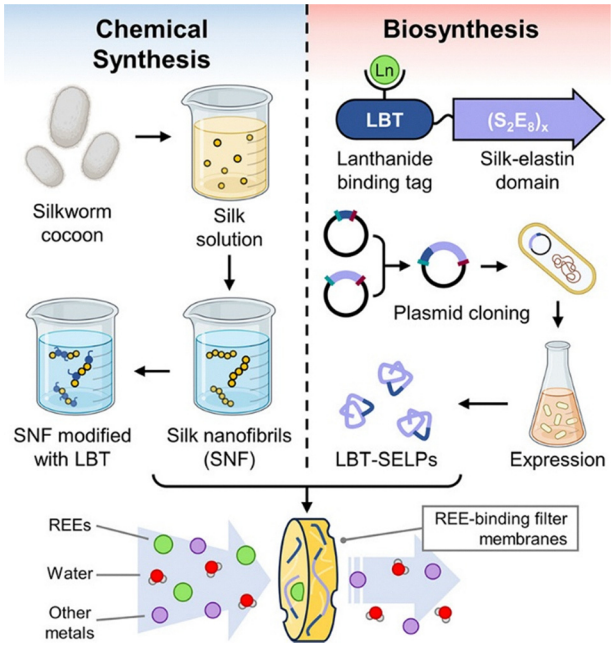

Fig. 26 Overview of the two approaches used to fabricate biobased filter membranes. Reprinted with permission from ref. 256. Copyright 2024 American Chemical Society.

6.3.4 Selectivity

REE vs. non-REE. Working with low-grade, secondary sources of REE that have a low content in REE (WEEE, phosphogypsum, bauxite, mine tailings, coal ashes, mine drainages) requires a good selectivity for REE *vs.* non-REE in order to minimize the purification steps. Usual competing metal ions consist notably of alkaline-earth (Ca, Mg), and d-block (Mn, Fe, Co, Ni, Cu, Zn) elements (Table 12). The ability of the different scaffolds or derived materials to retain selectively REE *vs.* non-REE has been assessed in most studies.

For the LBT-based fibres described by Joshi and coworkers,[255] REE sorption fell in the presence of 10 to 100 times more concentrated non-REE metal ions (Al, Cu, Fe, Ni), whereas Ca only had a small impact. Similarly, Kaplan and coworkers reported that the Tb^{3+}-binding capacity of silk nanofibrils functionalised with LBT was decreased in the presence of 10 to 100 times more concentrated Cu or Fe, but not by Ca and Zn.[256] LBT has a selectivity against Ca^{2+} of $\Delta\log K^{Ca} \approx 2$–3 (see 4. Selectivity), which appears sufficient to compensate for the difference in concentrations. However, from the observations made in these two studies, it is anticipated that LBT selectivity against d-block elements is quite low.

LanMs display a very high selectivity against Ca ($\Delta\log K^{Ca} \approx 8$ for *Mex*-LanM,[81,155] $\Delta\log K_a^{Ca} \approx 4$–6 for *Hans*-LanM[62]) and d-block elements ($\Delta\log K^{Cu} \approx 6$ and $\Delta\log K^{Zn} \approx 8$ for *Mex*-LanM[155]) (see 4. Selectivity). This can explain the impressive ability of LanM to selectively recover REE among other metal ions in complex solutions (Table 12) with high recovery yields and purity when using size-exclusion separation,[155] functionalised agarose beads,[257] or liquid–liquid phase separation.[258,259] Moreover, Gao, Wei and coworkers demonstrated that even with concentrations of non-REE 10 to 1000 times higher than of REE, LanM-functionalized magnetic nanoparticles could selectively bind REE over competing metal ions and achieve a REE purity of 31% wt (compared to the 0.03% wt of the initial solution) corresponding to a 967-fold improvement.[260]

RTX is interesting due to its ability to bind several Ln per protein over a broad pH range.[129] However, one limitation to its use is the precipitation of the protein at low pH. To overcome precipitation issues, Banta and coworkers coupled the RTX protein to a maltose-binding protein (MBP). Working at pH 6, they showed that RTX-MBP could selectively recover up to ~85% of Nd^{3+} and Dy^{3+} in a solution containing also Fe^{2+} and Co^{2+}, which suggests a good selectivity of this modified protein for Ln over d-block metal ions.

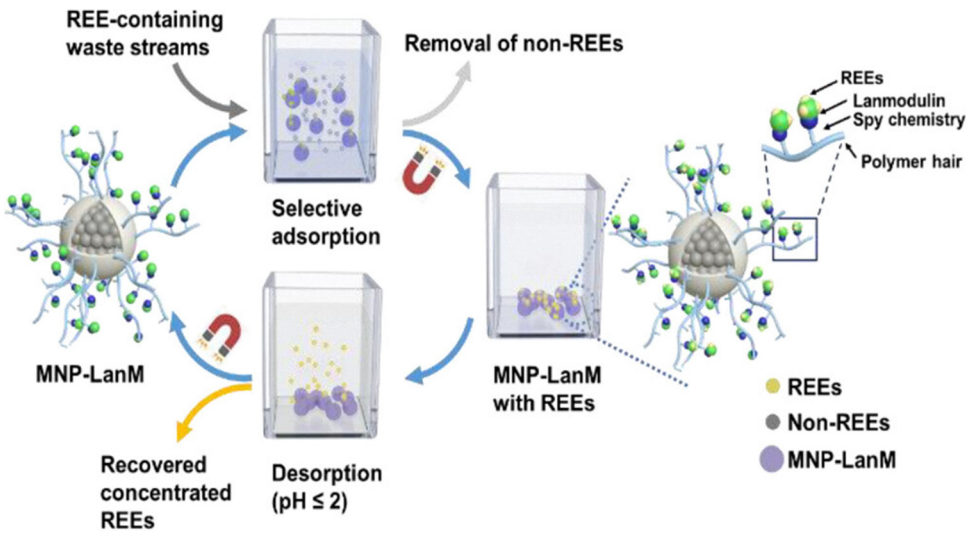

Fig. 27 Use of LanM-functionalized magnetic nanoparticles for REE recovery.[258,259] Reprinted with permission from ref. 260. Copyright 2023 American Chemical Society.

Open Access Article. Published on 22 September 2025. Downloaded on 4/1/2026 8:13:17 PM.
This article is licensed under a Creative Commons Attribution-NonCommercial 3.0 Unported Licence.

Intra-REE. The design of Ln-binding peptides and proteins with good intra-REE selectivity would be highly appealing with the aim to reduce the number of steps required to obtain pure and isolated REE, but it is an outstanding challenge given the similarities of REE (see 1. Introduction) and the moderate intra-REE selectivity displayed so far by Ln-binding peptides and proteins (see 4. Selectivity). The LBT-fibers reported by Joshi and coworkers showed a moderate preference for the binding of Eu^{3+}, Tb^{3+}, and Dy^{3+} relative to other Ln^{3+}.[255] Cotruvo and coworkers noted an intra-REE selectivity between heavy (HREE: Tb^{3+}–Lu^{3+}, Y^{3+}) and light (LREE: La^{3+}–Gd^{3+}) when using LanM-functionalised on agarose beads similar to the one observed in solution.[257]

To overcome the moderate intra-REE selectivity of Ln-binding peptides and proteins, some studies have proposed innovative strategies. The separation process based on LanM-functionalised on agarose beads was optimised by using mild competitors for Ln desorption (malonate, citrate).[167] A two-cycle process was proposed in order to recover five distinct fractions: Sc^{3+}, Y^{3+}, HREE (Gd^{3+}–Lu^{3+}), middle REE (MREE: Pr^{3+}–Eu^{3+}), and LREE (La^{3+}, Ce^{3+}). A solution reproducing metal ions concentrations found in coal combustion products or mine tailings was adsorbed onto the column. The first desorption cycle used malonate in order to desorb up to 99% of Sc with >99% purity. Next, pH desorption was performed by decreasing the pH successively to 2.3, 2.1 and 1.9, which enabled a first separation of REE into HREE and Y^{3+}, LREE, and MREE. These fractions were further purified using citrate desorption, which led to the recovery of HREE with 88–100% purity, >95% recovery of Y^{3+} with 92% purity, recovery of MREE with ~80% purity, and recovery of LREE with 98% purity.

As an alternative strategy, Cotruvo and coworkers investigated how intra-REE selectivity could be improved by controlling the dimerization state of *Hans*-LanM to separate Dy^{3+} from Nd^{3+} working with a synthetic leachate solution of NdFeB magnets.[62] With *Hans*-LanM functionalised agarose beads, Dy^{3+} could be desorbed from the column with malonate and obtained with 83% purity without significant desorption of Nd^{3+}, which was then desorbed at pH 1.5 and obtained at 99.8% purity. In a similar approach, the LanD-E75Q/E78A mutant optimised to form dimer with medium REE, was able to retain Pr^{3+} and Nd^{3+} better than the larger Ce^{3+} and La^{3+}.

6.3.5 Concluding note. The development of biomaterials based on Ln-binding peptides and proteins is well suited to exploit secondary REE sources, which are more dilute and of lower grade. As such, it represents a complementary approach to the development of chemical strategies that aim to improve the extraction and separation processes used on primary REE sources.[14,237]

REE recovery using Ln-binding peptides and proteins requires to meet several criteria. The first is the selectivity of the peptides and proteins for REE *vs.* non-REE, and ideally also for intra-REE separation. The discovery of LanM, which has a high selectivity *vs.* non-REE has represented a breakthrough compared to LBT-based strategies that are more sensitive to high concentrations of d-block metal ions. Nonetheless, Ln-binding peptides and proteins still present a moderate intra-REE selectivity

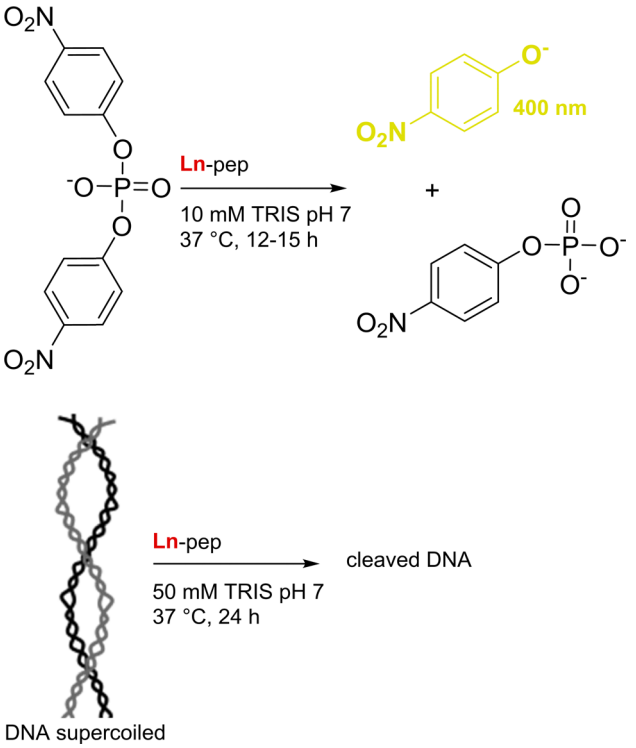

Fig. 28 Phosphate ester and DNA cleavage activities of Ln-pep (Ln = Eu^{3+}, Ce^{4+}).

(see 4. Selectivity) that will need to be improved. The second criterion is to improve the pH range in which the scaffold is stable and retains Ln-binding capacity. Last, different strategies were proposed for the sorption and recovery of REE. Scaling up to meet industrial needs will require a facile and low-cost production of the scaffold and its derived material. The strategy employed for functionalizing magnetic nanoparticles with LanM using Spy chemistry is interesting for this purpose, as it enabled the selective coupling of the protein directly from cell lysates, thus avoiding protein purification steps.[262]

Importantly, despite the considerable efforts made to develop innovative, more sustainable technologies to exploit secondary REE sources, the main challenge to their industrial implementation remains their economic viability. The economic feasibility of the biosorption process for the recovery of REE from different low-grade sources was evaluated and strongly depends on REE market prices. Only an increase of REE prices back to their level of 2011 would make actual biosorption processes profitable.[263] The fluctuating demands in REE and its impact on the development at the industrial scale of more environmentally friendly technologies have been discussed in ref. 235.

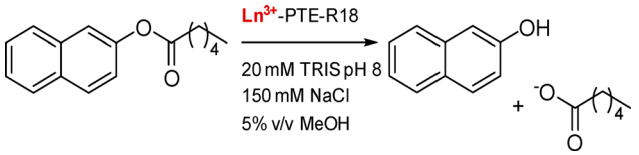

Fig. 29 Hydrolysis of 2-naphthyl hexanoate by Ln-PTE-R18.

Open Access Article. Published on 22 September 2025. Downloaded on 4/1/2026 8:13:17 PM.
This article is licensed under a Creative Commons Attribution-NonCommercial 3.0 Unported Licence.

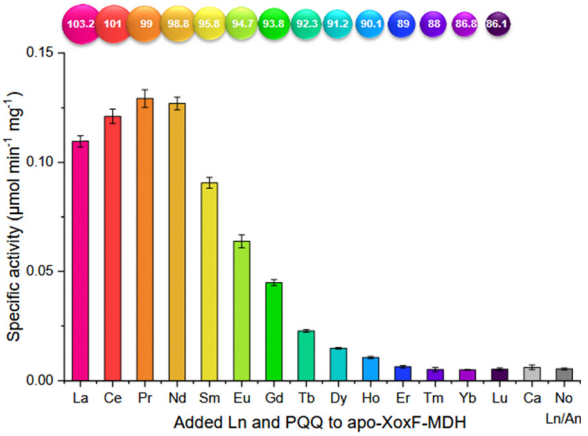

Fig. 30 Ln-dependent activity of XoxF-MDH. The enzyme was reconstituted from the apo-enzyme by incubation with PQQ and metal ion for 72 h at 4 °C. Reproduced from ref. 176 (Creative Commons Attribution Non-Commercial License 2023).

6.4 Catalysis

The field of Ln–proteins and Ln–peptides catalysis is emerging, and a few examples have been published. Ln^{3+} Lewis acidity has been exploited for hydrolysis reactions and in alcohol dehydrogenase (ADH)-like reactions (Section 6.2.1). Ln^{3+} photoredox properties have been exploited for the homolytic cleavage and oxidation of diols (Section 6.2.2).

6.4.1 Lewis acidity. Before the discovery of Ln–enzymes, Franklin and coworkers used Ln^{3+} Lewis acidic properties for the design of Ln–peptides as chimeric nucleases.[17,18] Helix-turn-helix peptides (HTH) combined an Ln^{3+}-binding loop and helices from engrailed homeodomain, the latter offering the possibility to recognize a specific DNA sequence. The resulting Ln–peptides (Ln = Eu^{3+}, Ce^{4+}) displayed DNA- and phosphate esters cleavage activities (Fig. 28).[264,265]

The Ce^{4+}–peptides were more active than their Eu^{3+} counterparts, consistent with the increased Lewis acidity and nucleophilicity of the Ln^{3+}-bound water molecules.[16] The effect of the pH on Ln–peptides reactivity was evaluated in the range 6.9–9.0.[266] The rate increased at pH 8.2, which is close to the pK_a of Ln^{3+}-bound water molecule (Fig. 1), indicating that it is involved in DNA hydrolytic cleavage. In addition, the cleavage catalysed by Ln–peptides was site-selective, suggesting that DNA sequences could be recognized and cleaved preferentially.[16]

Ln^{3+} Lewis acidic properties were also used for the catalysis of the hydrolysis of 2-naphthyl hexanoate (Fig. 29). Jackson and coworkers used the PTE-R18 protein, which has a Zn^{2+}-binding site, and showed that the demetallated protein could bind Ln^{3+}.[21] The activity of the resulting Ln–protein was pH-dependent, which was linked to the deprotonation of a Ln-bound water molecule.

The first and sole known Ln–enzymes, Ln-alcohol dehydrogenases (Ln-ADH), are an example of how the fine-tuning of Ln^{3+} Lewis acid properties along the series may impact reactivity. In the enzyme, Ln^{3+} is essential for catalysis because it tunes the redox potential of the redox cofactor, the pyrroloquinoline quinone (PQQ). Interestingly, the activity of the XoxF-methanol dehydrogenase (MDH) is strongly dependent on the Ln^{3+} in the active site, the lighter and less Lewis acidic Ln^{3+} giving the higher activity while no activity is detected for Ln^{3+} heavier than Er^{3+} (Fig. 30).[176] A similar trend has been also recently observed for an Ln-ADH from *Pseudomonas putida* KT2440 (PedH).[267] Several hypotheses have been proposed and are still under investigation to explain this dramatic impact on Ln-ADH reactivity. They consider not only PQQ redox properties, but also changes in the coordination number, or exchange rate constants of Ln^{3+}-bound substrate/product.

Working towards bringing new insights into Ln-MDH mechanism, Olshansky and coworkers built a structural mimic of the enzyme.[20] Starting from the PQQ-binding protein PqqT, they engineered the binding site with a single mutation ($K_{142}D$) in order to introduce a Ln^{3+}-binding site. They tested the ability of this structural mimic of Ln-MDH to oxidize benzyl alcohol, using a chemical trap (*O*-((perfluorophenyl)methyl)hydroxylamine (PFBHA)) to capture the benzaldehyde formed and identify it by LC-MS (Fig. 31). Only the La^{3+}–PQQ⊂$K_{142}D$–PqqT mutant was able to perform this reaction, and not the WT protein or $K_{142}A$ mutant both lacking an Ln^{3+}-binding site, nor the mutants lacking La^{3+}, or PQQ.

The ability of ADH to oxidize alcohols has been exploited further by Bange, Klebensberger and coworkers for foreseen application in bio-based plastic production.[116] Starting from the Pr-PedH from

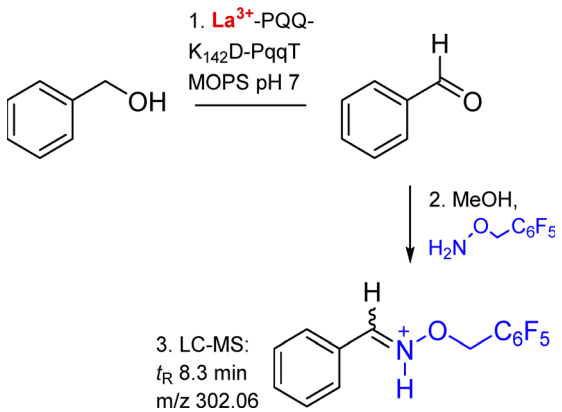

Fig. 31 Benzyl alcohol oxidation by La^{3+}-bound PQQ⊂$K_{142}D$–PqqT.

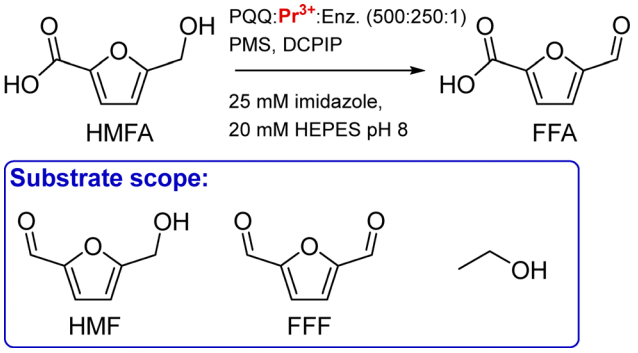

Fig. 32 Oxidation of 5-(hydroxymethyl)furoic acid (HMFA) and derivatives by mutants of PedH. FFA: 5-formylfuroic acid; HMF: 5-(hydroxymethyl)-furfural; FFF: 5-formylfurfural; PMS: phenazine methosulfate; DCPIP: 2,6-dichlorophenol indophenol.

Open Access Article. Published on 22 September 2025. Downloaded on 4/1/2026 8:13:17 PM.
This article is licensed under a Creative Commons Attribution-NonCommercial 3.0 Unported Licence.

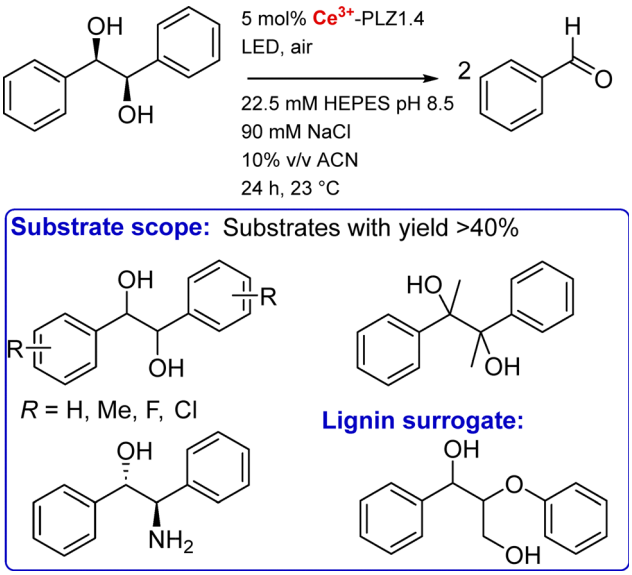

Fig. 33 Photoredox catalysis of aromatic diols homolytic cleavage by Ce-artificial enzymes.

P. putida KT2440, they constructed libraries of mutants of the enzyme expressed in *E. coli* and screened each colony for *in vivo* enzymatic activity towards the oxidation of HMFA (Fig. 32). This compound is an important intermediate for the obtention of furan-2,5-dicarboxylic acid (FDCA), a synthon that could serve as a plant-based alternative in the production of polymers. Out of 30 000 clones, 3 mutants were identified and their activity was confirmed by testing the purified enzymes. They shared mutations of the same residues, F412 and W561, positioned in the substrate channel and on a lid loop, respectively. These mutations enable bulkier substrates, such as HMFA, to access the active site. The mutant with the best catalytic activity for HMFA oxidation, PedH$^{F412V/W561A}$, could also successfully oxidize ethanol, HMF and FFF (Fig. 32), which opens up the route to the whole-cell biocatalytic production of FDCA.

6.4.2 Photoredox properties. So far, only a single example reported on the use of Ln photoredox properties in artificial enzymes for catalysis. Zeymer and co-workers designed an Ln-binding protein based on a TIM-barrel scaffold with the aim of exploiting the photocatalytic properties of Ce.[19]

The scaffold TFD-EE N6W was the starting point for the following catalysis study (Fig. 33).[19] Changes were made to the scaffold in order to introduce asymmetry in the binding site (single chain variant), to limit photodamage (removal of Trp residues), and to prevent non-specific metal binding to the protein surface (removal of clusters of negatively charged residues by mutating Asp to Asn and Glu to Gln), leading to the optimised scaffold PLZ1.4.

Upon irradiation, the artificial enzyme Ce-PLZ1.4 was able to catalyse the homolytic cleavage of homobenzoin into benzaldehyde (Fig. 33). Compared to molecular catalysts, the interest of the protein scaffold is to be able to control the stereoselectivity of the reaction. The authors showed that Ce-PLZ1.4 catalysed better the cleavage of (*R*,*R*)- and (*S*,*S*)-hydrobenzoin compared to the *meso*-isomer, and so displayed some diastereoselectivity. Investigation of the substrate scope of the enzyme also evidenced chemoselectivity, with aromatic diols being better cleaved than aliphatic ones. Last, the PLZ1.1 protein was expressed at the surface of *E. coli* cells, which were subsequently treated with $CeCl_3$ and light and were able to cleave a lignin surrogate (2-phenoxy-1-phenylpropane-1,3-diol) opening the way to photocontrolled whole-cell catalysis.

6.4.3 Concluding note. Lanthanides have versatile properties ranging from their Lewis acidity which offers a fine-tuning of the reactivity, to their redox properties that cover a broad range of potentials, and to their photochemical properties, which open the way to photocatalytic reactions. The similarities of Ln allow, with a single ligand, to modulate the reactivity of the catalyst simply by choosing the adequate Ln^{3+} ion, which is not possible with any other family of metal ions.

To date, the scope of Ln–peptides and Ln–proteins catalysts has been limited mainly to reactions exploiting Ln^{3+} Lewis acidity properties, with the exception of an original work demonstrating that photoredox catalysis is also achievable.[19] In addition, the peptide scaffold of the catalysts has been used to select the substrate, whether by using DNA recognition sequence, or by engineering the catalytic pocket,[116] or by favouring one stereoisomer over others.[19]

In the medium term, recent advances obtained with molecular catalysts should be transposable to Ln artificial enzymes. Ln-complexes have been used as Lewis acids catalysts,[268,269] in particular for C–C bond formation in aqueous media.[268] Ln-complexes are also powerful photocatalysts, that can be used for photo-reduction or photo-oxidation.[270–274] Notably, the reduction of CO_2, N_2 and NO_x was achieved in mild aqueous conditions.[273,274] Similar reactions could be implemented in artificial Ln–enzymes, which operate in aqueous media and whose peptide scaffold allows modulation of the hydrophilicity of the active site. Combining the chemical properties of Ln with the modularity of the peptide scaffold will help control the reactivity of the metal centre, the selectivity of the reaction and fine-tuning of second sphere interactions, and is expected to broaden the reactivities accessible with artificial enzyme.[275]

7. Conclusions & perspectives

In the last decade, significant progress has been made in the study of natural Ln-dependent proteins as well as in the design and engineering of Ln-binding peptides and proteins for a variety of relevant applications. Notwithstanding, numerous challenges remain to be addressed for the advancement of this flourishing field, starting with a sound and quantitative understanding of Ln coordination by pH buffers to refine the accuracy of available data and allow reliable comparisons.

The current limitations in designing Ln-binding systems with high affinity, selectivity, and inertness underscore the complexity of controlling key factors such as the coordination sphere (*i.e.* coordination and hydration number), scaffold stability, and the influence of long-range effects.

The control over the hydration number q is well understood and achievable for EF-hand motifs, and it can be tuned for other scaffolds by adjusting the denticity and positioning of the binding site within a hydrophobic environment. However, certain long-range outer-sphere factors, such as the local

Open Access Article. Published on 22 September 2025. Downloaded on 4/1/2026 8:13:17 PM.
This article is licensed under a Creative Commons Attribution-NonCommercial 3.0 Unported Licence.

conformation of the main chain and the orientation of amino acids can influence q in ways that are not yet fully controllable.

The majority of peptide and protein scaffolds exhibit an Ln-binding affinity in the micro- to nanomolar range ($\log K_{app} \sim 6$–9), with only a limited number extending to the picomolar range ($\log K_{app} \sim 12$), which is significantly lower than the affinity achievable with small chelators. Similarly to the tuning of the hydration number q, long-range outer-sphere factors, which are not yet understood, strongly influence the Ln affinity, as in the case of LanM compared to its isolated EF-hand motifs. It is worth noting that this gap between the Ln-affinity of peptide/proteins and small organic chelators is not observed for d-block metal ions, for which proteins and chelators of similar affinity, up to $\log K_{app} \sim 21$, are known. The underlying reason for this remains to be elucidated. One possible explanation is that, considering that we are at the dawn of lanthanome research, the tightest Ln-binding proteins have yet to be discovered. Besides, due to the ionic nature of Ln bonding and their preference for higher CN than d-block metal ions, peptides and proteins might need more demanding constraints to bind Ln^{3+} as efficiently as d-block metal ions.

Achieving higher affinities requires careful optimisation of both the Ln-binding site and scaffold stability by fine-tuning key parameters such as the type and denticity of the coordinating amino acids, as well as local and long-range structural constraints in the scaffold. To this end, computational design appears as a powerful tool to obtain a well-structured and stable protein scaffold, as is the case for the Ln-binding TIM barrel. In addition, the pH-dependency of Ln-binding by peptides and proteins has only been seldom looked at but is an important parameter for applications in REE recovery.

The selectivity relative to Ca^{2+} is generally favourable due to the higher coordination number and higher charge of Ln^{3+}. Nevertheless, the remarkable selectivity exhibited by LanM remains to be fully elucidated. Again, this is likely attributable to the influence of outer sphere effects.

With respect to d-block elements, the selectivity of peptides and proteins for Ln^{3+} often surpasses that of small chelators, a phenomenon attributable to distinct preferences for ligand types, coordination number and geometry.

In comparison to Ln^{3+}, peptide and protein scaffolds demonstrate a slightly higher affinity for An^{3+}, presumably due to enhanced covalency. However, further investigation is warranted to fully elucidate the underlying mechanisms and to boost the selectivity between Ln^{3+} and An^{3+}. Since An^{3+} can be (radioactive) contaminants of common Ln^{3+} sources, this will be crucial in the context of Ln recovery and radioactive decontamination.

The intra-Ln selectivity remains an outstanding challenge due to their similar ionic radii and Lewis acidity. The intra-Ln selectivity exhibited by peptide and protein scaffolds is not yet comparable to that observed for small chelators. This discrepancy may be attributed to the greater flexibility of peptides, which consequently enables a higher degree of adaptability to Ln^{3+} ions differences in ionic radius and coordination number. Further studies are required to ascertain whether size discrimination can be enhanced based on both electronic and steric considerations, for instance by modulating the rigidity of the coordination site and its position (buried or surface-exposed) within the scaffold.

The kinetic inertness of Ln coordinated to peptides and proteins is a largely neglected aspect that merits greater attention and research focus in the upcoming years, especially with respect to the development of efficient imaging agents and tools for Ln separation. In order to understand how to control the kinetic inertness of Ln–peptide and protein complexes, it is also essential to accumulate a substantial body of experimental data, which is currently lacking.

Overall, it appears that the elusive contributions beyond the first coordination sphere are of paramount importance in tuning properties like affinity, selectivity, and inertness, and must be studied further to achieve optimized designs. It is expected that emerging technologies based on machine learning and artificial intelligence will soon be beneficial in unravelling the influence of such long-range interactions, provided that solid experimental knowledge is established.[276–278] In this context, significant contributions are also expected from approaches beyond rational design, such as directed evolution.[279]

By deepening our understanding of these long-range effects and their impact on the coordination environment, we will be able to address the key challenges in the field: (i) developing high-affinity, intra-Ln selective peptides and proteins for enhanced Ln-recovery; (ii) achieving kinetically inert Ln-binding scaffolds for medical imaging and therapy; and (iii) optimizing the design of Ln-based (photo)catalysts. These advancements hold the potential to revolutionize a wide range of applications, from environmental sustainability to cutting-edge medical technologies.

Conflicts of interest

There are no conflicts to declare.

Data availability

No primary research results, software or code have been included and no new data were generated or analysed as part of this review.

Appendices

Table 14 Values from Fig. 1: trends of key parameters along the Ln series

Ln^{3+}	$E^{3+/2+}$ (V)[26]	$E^{4+/3+}$ (V)[26]	r (Å)[27]	pK_a[28]	$\log K_{sp}$[29]
La^{3+}	−3.1		1.216	8.89	−22.3
Ce^{3+}	−3.2	1.7	1.196	8.31	−23.5
Pr^{3+}	−2.7	3.4	1.179	8.3	−23.4
Nd^{3+}	−2.6	4.6	1.163	8.13	−24.1
Pm^{3+}	−2.6	4.9	1.144	n/a	n/a
Sm^{3+}	−1.55	5.2	1.132	7.84	−24.8
Eu^{3+}	−0.34	6.4	1.12	7.66	−25.5
Gd^{3+}	−3.9	7.9	1.107	7.87	−24.8
Tb^{3+}	−3.7	3.3	1.095	7.6	−25.7
Dy^{3+}	−2.5	5	1.083	7.53	−25.7
Ho^{3+}	−2.9	6.2	1.072	7.43	−26.4
Er^{3+}	−3.1	6.1	1.062	7.46	−26.2
Tm^{3+}	−2.3	6.1	1.052	7.34	−26.4
Yb^{3+}	−1.05	7.1	1.042	7.31	−26.7
Lu^{3+}		8.5	1.032	7.33	−26.6

Open Access Article. Published on 22 September 2025. Downloaded on 4/1/2026 8:13:17 PM.
This article is licensed under a Creative Commons Attribution-NonCommercial 3.0 Unported Licence.

Table 15 Values from Fig. 17: selectivity of different ligands across the Ln^{3+} series

Ln^{3+}	EDTA[a]	DTPA[a]	Macropa[b]	Macrotripa[c]	LBT12[d]	LF4[e]	RTX[f]	LanD[g]	LanM[h]	LanM[i]	LanM[j]	LanM[k]
La^{3+}	15.5	19.5	15.0	12.6	5.5	4.2	4.1	5.7	11.3		10.2	
Ce^{3+}	16.1	20.5	15.1	12.8	6.0			6.0				
Pr^{3+}	16.3	21.1	14.7	12.7			4.5	6.3		10.2		11.0
Nd^{3+}	16.6	21.6	14.4	12.3	6.6		4.5	6.6	11.3		10.0	10.7
Sm^{3+}	17.0	22.3	13.8	11.4				6.5	11.2			10.6
Eu^{3+}	17.2	22.4	13.0	10.9	7.2	4.6	4.6	6.5				
Gd^{3+}	17.3	22.5	13.0	10.2	7.1	4.6		6.2	11.0	10.0		
Tb^{3+}	17.8	22.7	11.8	10.2	7.2	4.9	4.6		10.7			
Dy^{3+}	18.2	22.8	11.7	10.5	7.2		4.6			9.7	8.6	10.8
Ho^{3+}	18.4	22.8	10.6	10.7		4.9			10.6	9.6		11.1
Er^{3+}	18.9	22.7	10.1	11.1	7.1	5.0						11.9
Tm^{3+}	19.6	22.7	9.6	11.4								12.4
Yb^{3+}	19.7	22.6	8.9	11.8	7.0	4.4	4.6					
Lu^{3+}	20.0	22.4	8.3	11.9	6.9	4.2	4.6					

[a] $\log \beta_{ML}$ from ref. 173. [b] $\log \beta_{ML}$ from ref. 160. [c] $\log \beta_{ML}$ from ref. 161. [d] $\log K_{app}$ in HEPES 10 mM pH 7, NaCl 100 mM, ref. 64. [e] $\log K_{app}$ in HEPES 10 mM pH 7.5, NaCl 10 mM, ref. 103. [f] $\log K_{app}$ in bis-Tris 20 mM pH 6, NaCl 25 mM, ref. 129. [g] $\log K_{app}$ in MOPS 30 mM pH 7, KCl 100 mM, ref. —. [h] $\log K_{app}$ for *Mex*-LanM in MOPS 30 mM pH 7.2, KCl 100 mM, measured by CD spectroscopy, ref. 81. [i] $\log K_{app}$ for *Mex*-LanM in acetate buffer 20 mM pH 5, KCl 100 mM, measured by CD spectroscopy, ref. 155. [j] $\log K_{app}$ for *Hans*-LanM acetate buffer 20 mM pH 5, KCl 100 mM, measured by CD spectroscopy, ref. 280. [k] $\log K_{app}$ for *Mex*-LanM KCl/KCH_3COO^- buffer 100 mM pH 5.0, measured by UV-vis spectroscopy, ref. 155.

Table 16 Values from Fig. 19: selectivity of small chelators and some peptide/protein scaffolds for Ln^{3+} over Ca^{2+}

Ln^{3+}	EDTA[a]	DTPA[a]	P3W[b]	EF loop[c]	CaM[d]	*Hans*-LanM[e]	*Mex*-LanM[f]	RTX[g]	PqqT[h]	PA[i]	2SCC[j]
La^{3+}	15.5	19.5	5.20			10.2	11.3	4.1	6.2		6.2
Ce^{3+}	16.1	20.5									
Pr^{3+}	16.3	21.1						4.5			
Nd^{3+}	16.6	21.6				10.0	11.3	4.5			
Sm^{3+}	17.0	22.3					11.2				
Eu^{3+}	17.2	22.4	5.2	6.8	8.00			4.6		6.8	
Gd^{3+}	17.3	22.5	5.2				11.0				
Tb^{3+}	17.8	22.7		6.8	8.8		10.7	4.6		6.3	
Dy^{3+}	18.2	22.8				8.6		4.6			
Ho^{3+}	18.4	22.8					10.6				
Er^{3+}	18.9	22.7									
Tm^{3+}	19.6	22.7									
Yb^{3+}	19.7	22.6						4.6			6.4
Lu^{3+}	20.0	22.4						4.6			
Ca^{2+}	11.0	10.7	4.5	4.6	6	4.2	3.2	3.3	3.8	3.7	1.7

[a] $\log \beta_{ML}$ from ref. 173. [b] $\log K_{app}$ in TRIS 5 mM pH 7.8, from ref. 76. [c] $\log K_{app}$ in HEPES 10 mM pH 7, NaCl 100 mM, from ref. 169. [d] $\log K_{app}$ in PIPES 25 mM pH 6.8, KCl 100 mM, from ref. 82. [e] $\log K_{app}$ for *Hans*-LanM acetate buffer 20 mM pH 5, KCl 100 mM, measured by CD spectroscopy, ref. 280. [f] $\log K_{app}$ for *Mex*-LanM in MOPS 30 mM pH 7.2, KCl 100 mM, measured by CD spectroscopy, ref. 81. [g] $\log K_{app}$ in bis-Tris 20 mM pH 6, NaCl 25 mM, ref. 129. [h] $\log K_{app}$ in HEPES 30 mM pH 7, NaCl 100 mM, from ref. 20. [i] $\log K_{app}$ in HEPES 10 mM pH 7, from ref. 41. [j] $\log K_{app}$ in Imidazole 30 mM pH 6.9, KCl 50 mM, from ref. 95.

Acknowledgements

The authors acknowledge financial support from the French National Research Agency (ANR) through the ANR-23-CE07-0002 (LnZYME) and ANR-22-CE29-0026 (DREAMY) projects.

References

1 S. V. Eliseeva and J.-C. G. Bünzli, *New J. Chem.*, 2011, **35**, 1165–1176.
2 Directorate-General for Internal Market, Industry, Entrepreneurship and SMEs (European Commission), M. Grohol and C. Veeh, *Study on the critical raw materials for the EU 2023: final report*, Publications Office of the European Union, 2023.
3 V. Balaram, *Geosci. Front.*, 2019, **10**, 1285–1303.
4 N. A. Fitriyanto, M. Fushimi, M. Matsunaga, A. Pertiwiningrum, T. Iwama and K. Kawai, *J. Biosci. Bioeng.*, 2011, **111**, 613–617.
5 Y. Hibi, K. Asai, H. Arafuka, M. Hamajima, T. Iwama and K. Kawai, *J. Biosci. Bioeng.*, 2011, **111**, 547–549.
6 T. Nakagawa, R. Mitsui, A. Tani, K. Sasa, S. Tashiro, T. Iwama, T. Hayakawa and K. Kawai, *PLoS One*, 2012, **7**, e50480.
7 A. Pol, T. R. M. Barends, A. Dietl, A. F. Khadem, J. Eygensteyn, M. S. M. Jetten and H. J. M. O. den Camp, *Environ. Microbiol.*, 2014, **16**, 255–264.
8 L. Ancel, A. Niedźwiecka, C. Lebrun, C. Gateau and P. Delangle, *C. R. Chim.*, 2013, **16**, 515–523.
9 E. Skovran, C. Raghuraman and N. C. Martinez-Gomez, *Curr. Issues Mol. Biol.*, 2019, 101–116.

Open Access Article. Published on 22 September 2025. Downloaded on 4/1/2026 8:13:17 PM.
This article is licensed under a Creative Commons Attribution-NonCommercial 3.0 Unported Licence.

10 L. J. Daumann, *Angew. Chem., Int. Ed.*, 2019, **58**, 12795–12802.
11 E. R. Featherston and J. A. Cotruvo, *Biochim. Biophys. Acta, Mol. Cell Res.*, 2021, **1868**, 118864.
12 L. J. Daumann, A. Pol, H. J. M. Op Den Camp and N. C. Martinez-Gomez, *Advances in Microbial Physiology*, Elsevier, 2022, vol. 81, pp. 1–24.
13 A. M. Webster and A. F. A. Peacock, *Chem. Commun.*, 2021, **57**, 6851–6862.
14 J. A. Mattocks and J. A. Cotruvo, *Chem. Soc. Rev.*, 2020, **49**, 8315–8334.
15 Q. Ye, D. Wang and N. Wei, *Trends Biotechnol.*, 2024, **42**, 575–590.
16 R. T. Kovacic, J. T. Welch and S. J. Franklin, *J. Am. Chem. Soc.*, 2003, **125**, 6656–6662.
17 S. Lim and S. J. Franklin, *Cell. Mol. Life Sci.*, 2004, **61**, 2184–2188.
18 S. J. Franklin and J. T. Welch, *Comments Inorg. Chem.*, 2005, **26**, 127–164.
19 A. S. Klein, F. Leiss-Maier, R. Mühlhofer, B. Boesen, G. Mustafa, H. Kugler and C. Zeymer, *J. Am. Chem. Soc.*, 2024, **146**(38), 25976–25985.
20 P. J. Thompson, D. G. Boggs, C. A. Wilson, A. T. Bruchs, U. Velidandla, J. Bridwell-Rabb and L. Olshansky, *Proc. Natl. Acad. Sci. U. S. A.*, 2024, **121**, e2405836121.
21 C. W. Breeze, Y. Nakano, E. C. Campbell, R. L. Frkic, D. W. Lupton and C. J. Jackson, *Acta Crystallogr., Sect. D:Struct. Biol.*, 2024, **80**, 289–298.
22 L. Götzke, G. Schaper, J. März, P. Kaden, N. Huittinen, T. Stumpf, K. K. K. Kammerlander, E. Brunner, P. Hahn, A. Mehnert, B. Kersting, T. Henle, L. F. Lindoy, G. Zanoni and J. J. Weigand, *Coord. Chem. Rev.*, 2019, **386**, 267–309.
23 R. Sánchez-Fernández, I. Obregon-Gomez, A. Sarmiento, M. E. Vázquez and E. Pazos, *Chem. Commun.*, 2024, **60**, 12650–12661.
24 M. A. Hay and C. Boskovic, *Chem. – Eur. J.*, 2021, **27**, 3608–3637.
25 R. G. Pearson, *J. Am. Chem. Soc.*, 1963, **85**, 3533–3539.
26 L. R. Morss, *Chem. Rev.*, 1976, **76**, 827–841.
27 P. D'Angelo, A. Zitolo, V. Migliorati, G. Chillemi, M. Duvail, P. Vitorge, S. Abadie and R. Spezia, *Inorg. Chem.*, 2011, **50**, 4572–4579.
28 R. D. Shannon, *Acta Crystallogr., Sect. A*, 1976, **32**, 751–767.
29 C. Ekberg and P. L. Brown, *Hydrolysis of Metal Ions*, John Wiley & Sons, Ltd, 2016.
30 H. C. Aspinall, *f-Block Chemistry*, Oxford University Press, 2020.
31 L. Ruckthong, M. L. Zastrow, J. A. Stuckey and V. L. Pecoraro, *J. Am. Chem. Soc.*, 2016, **138**, 11979–11988.
32 S. C. Edington, S. Liu and C. R. Baiz, in *Methods in Enzymology*, ed. J. A. Cotruvo, Academic Press, 2021, vol. 651, pp. 157–191.
33 S. Liu, E. R. Featherston, J. A. Cotruvo and C. R. Baiz, *Phys. Chem. Chem. Phys.*, 2021, **23**, 21690–21700.
34 S. A. Cotton, *C. R. Chim.*, 2005, **8**, 129–145.
35 A. Smerigan, S. Biswas, F. D. Vila, J. Hong, J. Perez-Aguilar, A. S. Hoffman, L. Greenlee, R. B. Getman and S. R. Bare, *Inorg. Chem.*, 2023, **62**, 14523–14532.
36 T. Summers, D. Zhang, J. Sobrinho, A. de Bettencourt-Dias, R. Rousseau, V.-A. Glezakou and D. Cantu, *ChemRxiv*, 2024, preprint, DOI: **10.26434/chemrxiv-2024-lgkjh**.
37 H. Lumpe, A. Menke, C. Haisch, P. Mayer, A. Kabelitz, K. V. Yusenko, A. Guilherme Buzanich, T. Block, R. Pöttgen, F. Emmerling and L. J. Daumann, *Chem. – Eur. J.*, 2020, **26**, 10133–10139.
38 K. Binnemans, *Coord. Chem. Rev.*, 2015, **295**, 1–45.
39 A. Beeby, I. M. Clarkson, R. S. Dickins, S. Faulkner, D. Parker, L. Royle, A. S. de Sousa, J. A. G. Williams and M. Woods, *J. Chem. Soc., Perkin Trans. 2*, 1999, 493–504.
40 R. M. Supkowski and W. D. W. Horrocks, *Inorg. Chim. Acta*, 2002, **340**, 44–48.
41 C. S. Bonnet, P. H. Fries, S. Crouzy, O. Sénèque, F. Cisnetti, D. Boturyn, P. Dumy and P. Delangle, *Chem. – Eur. J.*, 2009, **15**, 7083–7093.
42 G. Pintacuda, M. John, X.-C. Su and G. Otting, *Acc. Chem. Res.*, 2007, **40**, 206–212.
43 K. N. Allen and B. Imperiali, *Curr. Opin. Chem. Biol.*, 2010, **14**, 247–254.
44 W.-M. Liu, M. Overhand and M. Ubbink, *Coord. Chem. Rev.*, 2014, **273–274**, 2–12.
45 C. Nitsche and G. Otting, *Prog. Nucl. Magn. Reson. Spectrosc.*, 2017, **98–99**, 20–49.
46 D. Joss and D. Häussinger, *Prog. Nucl. Magn. Reson. Spectrosc.*, 2019, **114–115**, 284–312.
47 I. Baig, I. Bertini, C. Del Bianco, Y. K. Gupta, Y.-M. Lee, C. Luchinat and A. Quattrone, *Biochemistry*, 2004, **43**, 5562–5573.
48 I. Bertini, C. Del Bianco, I. Gelis, N. Katsaros, C. Luchinat, G. Parigi, M. Peana, A. Provenzani and M. A. Zoroddu, *Proc. Natl. Acad. Sci. U. S. A.*, 2004, **101**, 6841–6846.
49 N. C. J. Strynadka and M. N. G. James, *Annu. Rev. Biochem.*, 1989, **58**, 951–999.
50 A. Lewit-Bentley and S. Réty, *Curr. Opin. Struct. Biol.*, 2000, **10**, 637–643.
51 Z. Grabarek, *J. Mol. Biol.*, 2006, **359**, 509–525.
52 J. L. Gifford, M. P. Walsh and H. J. Vogel, *Biochem. J.*, 2007, **405**, 199–221.
53 D. B. Halling, B. J. Liebeskind, A. W. Hall and R. W. Aldrich, *Proc. Natl. Acad. Sci. U. S. A.*, 2016, **113**(9), 1216–1225.
54 H. G. Brittain, F. S. Richardson and R. B. Martin, *J. Am. Chem. Soc.*, 1976, **98**, 8255–8260.
55 B. Martin and F. S. Richardson, *Q. Rev. Biophys.*, 1979, **12**, 181–209.
56 W. D. Horrocks and D. R. Sudnick, *Acc. Chem. Res.*, 1981, **14**, 384–392.
57 M. A. Valentini and J. C. Wright, *Anal. Biochem.*, 1985, **150**, 47–57.
58 C.-L. A. Wang, P. C. Leavis, W. D. Horrocks and J. Gergely, *Biochemistry*, 1981, **20**, 2439–2444.
59 J. Gariepy, B. D. Sykes and R. S. Hodges, *Biochemistry*, 1983, **22**, 1765–1772.

Open Access Article. Published on 22 September 2025. Downloaded on 4/1/2026 8:13:17 PM.
This article is licensed under a Creative Commons Attribution-NonCommercial 3.0 Unported Licence.

60 K. D. Daughtry, L. J. Martin, A. Sarraju, B. Imperiali and K. N. Allen, *ChemBioChem*, 2012, **13**, 2567–2574.
61 S. Jain, J. T. Welch, W. D. Horrocks and S. J. Franklin, *Inorg. Chem.*, 2003, **42**, 8098–8104.
62 J. A. Mattocks, J. J. Jung, C.-Y. Lin, Z. Dong, N. H. Yennawar, E. R. Featherston, C. S. Kang-Yun, T. A. Hamilton, D. M. Park, A. K. Boal and J. A. Cotruvo, *Nature*, 2023, **618**, 87–93.
63 E. R. Featherston, E. J. Issertell and J. A. Cotruvo, *J. Am. Chem. Soc.*, 2021, **143**, 14287–14299.
64 M. Nitz, M. Sherawat, K. J. Franz, E. Peisach, K. N. Allen and B. Imperiali, *Angew. Chem., Int. Ed.*, 2004, **43**, 3682–3685.
65 K. Barthelmes, A. M. Reynolds, E. Peisach, H. R. A. Jonker, N. J. DeNunzio, K. N. Allen, B. Imperiali and H. Schwalbe, *J. Am. Chem. Soc.*, 2011, **133**, 808–819.
66 J. P. MacManus, C. W. Hogue, B. J. Marsden, M. Sikorska and A. G. Szabo, *J. Biol. Chem.*, 1990, **265**, 10358–10366.
67 J. Wöhnert, K. J. Franz, M. Nitz, B. Imperiali and H. Schwalbe, *J. Am. Chem. Soc.*, 2003, **125**, 13338–13339.
68 L. J. Martin, M. J. Hähnke, M. Nitz, J. Wöhnert, N. R. Silvaggi, K. N. Allen, H. Schwalbe and B. Imperiali, *J. Am. Chem. Soc.*, 2007, **129**, 7106–7113.
69 N. R. Silvaggi, L. J. Martin, H. Schwalbe, B. Imperiali and K. N. Allen, *J. Am. Chem. Soc.*, 2007, **129**, 7114–7120.
70 D. Barthelmes, M. Gränz, K. Barthelmes, K. N. Allen, B. Imperiali, T. Prisner and H. Schwalbe, *J. Biomol. NMR*, 2015, **63**, 275–282.
71 T. W. Victor, K. H. O'Toole, L. M. Easthon, M. Ge, R. J. Smith, X. Huang, H. Yan, Y. S. Chu, S. Chen, D. Gursoy, M. Ralle, B. Imperiali, K. N. Allen and L. M. Miller, *J. Am. Chem. Soc.*, 2020, **142**, 2145–2149.
72 M. Nitz, K. J. Franz, R. L. Maglathlin and B. Imperiali, *ChemBioChem*, 2003, **4**, 272–276.
73 L. J. Martin, B. R. Sculimbrene, M. Nitz and B. Imperiali, *QSAR Comb. Sci.*, 2005, **24**, 1149–1157.
74 L. J. Martin and B. Imperiali, in *Peptide Libraries: Methods and Protocols*, ed. R. Derda, Springer, New York, NY, 2015, pp. 201–220.
75 Y. Kim, J. T. Welch, K. M. Lindstrom and S. J. Franklin, *JBIC, J. Biol. Inorg. Chem.*, 2001, **6**, 173–181.
76 J. T. Welch, W. R. Kearney and S. J. Franklin, *Proc. Natl. Acad. Sci. U. S. A.*, 2003, **100**, 3725–3730.
77 P. Caravan, J. M. Greenwood, J. T. Welch and S. J. Franklin, *Chem. Commun.*, 2003, 2574–2575.
78 S. Lim and S. J. Franklin, *Protein Sci.*, 2006, **15**, 2159–2165.
79 S. W. Wong-Deyrup, Y. Kim and S. J. Franklin, *JBIC, J. Biol. Inorg. Chem.*, 2006, **11**, 17–25.
80 K. L. Harris, S. Lim and S. J. Franklin, *Inorg. Chem.*, 2006, **45**, 10002–10012.
81 J. A. Cotruvo, E. R. Featherston, J. A. Mattocks, J. V. Ho and T. N. Laremore, *J. Am. Chem. Soc.*, 2018, **140**, 15056–15061.
82 C.-L. A. Wang, R. R. Aquaron, P. C. Leavis and J. Gergely, *Eur. J. Biochem.*, 1982, **124**, 7–12.
83 E. C. Cook, E. R. Featherston, S. A. Showalter and J. A. Cotruvo, *Biochemistry*, 2019, **58**, 120–125.
84 F. Cisnetti, C. Lebrun and P. Delangle, *Dalton Trans.*, 2010, **39**, 3560–3562.
85 F. Cisnetti, C. Gateau, C. Lebrun and P. Delangle, *Chem. – Eur. J.*, 2009, **15**, 7456–7469.
86 A. Niedźwiecka, F. Cisnetti, C. Lebrun, C. Gateau and P. Delangle, *Dalton Trans.*, 2012, **41**, 3239–3247.
87 A. Niedźwiecka, F. Cisnetti, C. Lebrun and P. Delangle, *Inorg. Chem.*, 2012, **51**, 5458–5464.
88 J. Veliscek-Carolan, T. L. Hanley and K. A. Jolliffe, *RSC Adv.*, 2016, **6**, 75336–75346.
89 S. Safi, A. Jeanson, J. Roques, P. L. Solari, F. Charnay-Pouget, C. Den Auwer, G. Creff, D. J. Aitken and E. Simoni, *Inorg. Chem.*, 2016, **55**, 877–886.
90 I. V. Korendovych and W. F. DeGrado, *Q. Rev. Biophys.*, 2020, **53**, e3.
91 K. J. Koebke, T. B. J. Pinter, W. C. Pitts and V. L. Pecoraro, *Chem. Rev.*, 2022, **122**, 12046–12109.
92 P. Teare, C. F. Smith, S. J. Adams, S. Anbu, B. Ciani, L. J. C. Jeuken and A. F. A. Peacock, *Dalton Trans.*, 2018, **47**, 10784–10790.
93 D. N. Woolfson, *Advances in Protein Chemistry*, Academic Press, 2005, vol. 70, pp. 79–112.
94 W. D. Kohn, C. M. Kay and R. S. Hodges, *J. Pept. Res.*, 1998, **51**, 9–18.
95 W. D. Kohn, C. M. Kay, B. D. Sykes and R. S. Hodges, *J. Am. Chem. Soc.*, 1998, **120**, 1124–1132.
96 A. Kashiwada, K. Ishida and K. Matsuda, *Bull. Chem. Soc. Jpn.*, 2007, **80**, 2203–2207.
97 M. Samiappan, S. Alasibi, R. Cohen-Luria, A. Shanzer and G. Ashkenasy, *Chem. Commun.*, 2012, **48**, 9577–9579.
98 M. R. Berwick, D. J. Lewis, A. W. Jones, R. A. Parslow, T. R. Dafforn, H. J. Cooper, J. Wilkie, Z. Pikramenou, M. M. Britton and A. F. A. Peacock, *J. Am. Chem. Soc.*, 2014, **136**, 1166–1169.
99 M. R. Berwick, L. N. Slope, C. F. Smith, S. M. King, S. L. Newton, R. B. Gillis, G. G. Adams, A. J. Rowe, S. E. Harding, M. M. Britton and A. F. A. Peacock, *Chem. Sci.*, 2016, **7**, 2207–2216.
100 L. N. Slope, M. G. Hill, C. F. Smith, P. Teare, F. J. de Cogan, M. M. Britton and A. F. A. Peacock, *Chem. Commun.*, 2020, **56**, 3729–3732.
101 L. N. Slope, O. J. Daubney, H. Campbell, S. A. White and A. F. A. Peacock, *Angew. Chem., Int. Ed.*, 2021, **60**, 24473–24477.
102 S. L. Newton, A. Franke, A. Zahl, G. Molinaro, A. Kenwright, D. J. Smith, I. Ivanovic-Burmazovic, M. M. Britton and A. F. A. Peacock, *Dalton Trans.*, 2023, **52**, 15665–15668.
103 C. W. A. Ende, H. Y. Meng, M. Ye, A. K. Pandey and N. J. Zondlo, *ChemBioChem*, 2010, **11**, 1738–1747.
104 A. F. A. Peacock, *J. Inorg. Biochem.*, 2025, **268**, 112903.
105 J. K. Myers, C. N. Pace and J. M. Scholtz, *Proc. Natl. Acad. Sci. U. S. A.*, 1997, **94**, 2833–2837.
106 J. S. Richardson and D. C. Richardson, *Science*, 1988, **240**, 1648–1652.
107 L. G. Presta and G. D. Rose, *Science*, 1988, **240**, 1632–1641.
108 L. Serrano and A. R. Fersht, *Nature*, 1989, **342**, 296–299.
109 Y. W. Deng, S. Y. Ro and A. C. Rosenzweig, *JBIC, J. Biol. Inorg. Chem.*, 2018, **23**, 1037–1047.

 This journal is © The Royal Society of Chemistry 2025

Open Access Article. Published on 22 September 2025. Downloaded on 4/1/2026 8:13:17 PM.
This article is licensed under a Creative Commons Attribution-NonCommercial 3.0 Unported Licence.

110 N. M. Good, M. Fellner, K. Demirer, J. Hu, R. P. Hausinger and N. C. Martinez-Gomez, *J. Biol. Chem.*, 2020, **295**, 8272–8284.
111 R. A. Schmitz, N. Picone, H. Singer, A. Dietl, K.-A. Seifert, A. Pol, M. S. M. Jetten, T. R. M. Barends, L. J. Daumann and H. J. M. Op den Camp, *mBio*, 2021, **12**, e01708–21.
112 B. Jahn, A. Pol, H. Lumpe, T. R. M. Barends, A. Dietl, C. Hogendoorn, H. J. M. Op den Camp and L. J. Daumann, *ChemBioChem*, 2018, **19**, 1147–1153.
113 N. M. Good, H. N. Vu, C. J. Suriano, G. A. Subuyuj, E. Skovran and N. C. Martinez-Gomez, *J. Bacteriol.*, 2016, **198**, 3109–3118.
114 M. Wehrmann, P. Billard, A. Martin-Meriadec, A. Zegeye and J. Klebensberger, *mBio*, 2017, **8**, e00570–17.
115 J. Huang, Z. Yu, J. Groom, J.-F. Cheng, A. Tarver, Y. Yoshikuni and L. Chistoserdova, *ISME J.*, 2019, **13**, 2005–2017.
116 M. Wehrmann, E. M. Elsayed, S. Köbbing, L. Bendz, A. Lepak, J. Schwabe, N. Wierckx, G. Bange and J. Klebensberger, *ACS Catal.*, 2020, **10**, 7836–7842.
117 N. M. Good, R. S. Moore, C. J. Suriano and N. C. Martinez-Gomez, *Sci. Rep.*, 2019, **9**, 1–12.
118 L. Wang, A. Hibino, S. Suganuma, A. Ebihara, S. Iwamoto, R. Mitsui, A. Tani, M. Shimada, T. Hayakawa and T. Nakagawa, *Enzyme Microb. Technol.*, 2020, **136**, 109518.
119 H. Lumpe, A. Pol, H. J. M. Op den Camp and L. J. Daumann, *Dalton Trans.*, 2018, **47**, 10463–10472.
120 C. Stines-Chaumeil, F. Mavré, B. Kauffmann, N. Mano and B. Limoges, *ACS Omega*, 2020, **5**, 2015–2026.
121 P. Roszczenko-Jasińska, H. N. Vu, G. A. Subuyuj, R. V. Crisostomo, J. Cai, N. F. Lien, E. J. Clippard, E. M. Ayala, R. T. Ngo, F. Yarza, J. P. Wingett, C. Raghuraman, C. A. Hoeber, N. C. Martinez-Gomez and E. Skovran, *Sci. Rep.*, 2020, **10**, 12663.
122 J. L. Hemmann, P. Keller, L. Hemmerle, T. Vonderach, A. M. Ochsner, M. Bortfeld-Miller, D. Günther and J. A. Vorholt, *J. Biol. Chem.*, 2023, **299**, 102940.
123 J. A. Mattocks, J. V. Ho and J. A. Cotruvo, *J. Am. Chem. Soc.*, 2019, **141**, 2857–2861.
124 A. M. Ochsner, L. Hemmerle, T. Vonderach, R. Nüssli, M. Bortfeld-Miller, B. Hattendorf and J. A. Vorholt, *Mol. Microbiol.*, 2019, **111**, 1152–1166.
125 W. B. Larrinaga, J. J. Jung, C.-Y. Lin, A. K. Boal and J. A. Cotruvo, *Proc. Natl. Acad. Sci. U. S. A.*, 2024, **121**, e2410926121.
126 S. J. Caldwell, I. C. Haydon, N. Piperidou, P.-S. Huang, M. J. Bick, H. S. Sjöström, D. Hilvert, D. Baker and C. Zeymer, *Proc. Natl. Acad. Sci. U. S. A.*, 2020, **117**, 30362–30369.
127 M. A. Blenner, O. Shur, G. R. Szilvay, D. M. Cropek and S. Banta, *J. Mol. Biol.*, 2010, **400**, 244–256.
128 W. Abdallah, K. Solanki and S. Banta, *ACS Catal.*, 2018, **8**, 1602–1613.
129 F. Khoury, Z. Su and S. Banta, *Inorg. Chem.*, 2024, **63**(29), 13223–13230.
130 J. A. Mattocks, J. L. Tirsch and J. A. Cotruvo, in *Methods in Enzymology*, ed. J. A. Cotruvo, Academic Press, 2021, vol. 651, pp. 23–61.
131 G. Deblonde, *Methods in Enzymology*, Academic Press, 2021, vol. 651, pp. 1–22.
132 W. R. Harris, C. J. Carrano and K. N. Raymond, *J. Am. Chem. Soc.*, 1979, **101**, 2722–2727.
133 E. Falcone and P. Faller, *Dalton Trans.*, 2023, **52**, 2197–2208.
134 Z. M. Anwar and H. A. Azab, *J. Chem. Eng. Data*, 2001, **46**, 613–618.
135 H. A. Azab, S. S. Al-Deyab, Z. M. Anwar, I. I. Abd El-Gawad and R. M. Kamel, *J. Chem. Eng. Data*, 2011, **56**, 2613–2625.
136 H. A. Azab, Z. M. Anwar and R. M. Kamel, *J. Solution Chem.*, 2016, **45**, 1516–1528.
137 P. Mandal, J. Kretzschmar and B. Drobot, *JBIC, J. Biol. Inorg. Chem.*, 2022, **27**, 249–260.
138 R. N. Goldberg, N. Kishore and R. M. Lennen, *J. Phys. Chem. Ref. Data*, 2002, **31**, 231–370.
139 K. J. Franz, M. Nitz and B. Imperiali, *ChemBioChem*, 2003, **4**, 265–271.
140 E. A. Alasadi, W. Choi, X. Chen, J. A. J. Cotruvo and C. R. Baiz, *ACS Chem. Biol.*, 2024, **19**, 1056–1065.
141 E. M. Jones, Y. Su, C. Sander, Q. A. Justman, M. Springer and P. A. Silver, *ACS Synth. Biol.*, 2024, **13**, 958–962.
142 L. L. Clainche, M. Figuet, V. Montjardet-Bas, S. Blanchard and C. Vita, *Biotechnol. Bioeng.*, 2006, **95**, 29–36.
143 S. M. Gutenthaler, S. Tsushima, R. Steudtner, M. Gailer, A. Hoffmann-Röder, B. Drobot and L. J. Daumann, *Inorg. Chem. Front.*, 2022, **9**, 4009–4021.
144 S. C. Zondlo, F. Gao and N. J. Zondlo, *J. Am. Chem. Soc.*, 2010, **132**, 5619–5621.
145 S. Balakrishnan and N. J. Zondlo, *J. Am. Chem. Soc.*, 2006, **128**, 5590–5591.
146 A. R. Urmey and N. J. Zondlo, *Biochemistry*, 2019, **58**, 2822–2833.
147 A. R. Urmey and N. J. Zondlo, *Free Radical Biol. Med.*, 2020, **152**, 166–174.
148 F. Gao, B. S. Thornley, C. M. Tressler, D. Naduthambi and N. J. Zondlo, *Org. Biomol. Chem.*, 2019, **17**, 3984–3995.
149 L. L. Liu and K. J. Franz, *J. Am. Chem. Soc.*, 2005, **127**, 9662–9663.
150 J. A. Mattocks, J. L. Tirsch and J. A. Cotruvo, *Methods in Enzymology*, Elsevier, 2021, vol. 651, pp. 23–61.
151 B. Mwewa, M. Tadie, S. Ndlovu, G. S. Simate and E. Matinde, *J. Environ. Chem. Eng.*, 2022, **10**, 107704.
152 S. Pramanik, S. Kaur, I. Popovs, A. S. Ivanov and S. Jansone-Popova, *Eur. J. Inorg. Chem.*, 2024, e202400064.
153 J. Haiech, C. B. Klee, J. G. Demaille and J. Haiech, *Biochemistry*, 1981, **20**, 3890–3897.
154 D. M. Park, D. W. Reed, M. C. Yung, A. Eslamimanesh, M. M. Lencka, A. Anderko, Y. Fujita, R. E. Riman, A. Navrotsky and Y. Jiao, *Environ. Sci. Technol.*, 2016, **50**, 2735–2742.
155 G. J.-P. Deblonde, J. A. Mattocks, D. M. Park, D. W. Reed, J. A. Cotruvo and Y. Jiao, *Inorg. Chem.*, 2020, **59**, 11855–11867.
156 T. L. Pham, M. R. Conde González, S. Fazliev, A. Kishore, P. Comba and F. Thomas, *ChemBioChem*, 2024, **25**, e202300715.
157 D. Ghosh, K.-H. Lee, B. Demeler and V. L. Pecoraro, *Biochemistry*, 2005, **44**, 10732–10740.

Open Access Article. Published on 22 September 2025. Downloaded on 4/1/2026 8:13:17 PM.
This article is licensed under a Creative Commons Attribution-NonCommercial 3.0 Unported Licence.

158 J. A. Peters, K. Djanashvili, C. F. G. C. Geraldes and C. Platas-Iglesias, *Coord. Chem. Rev.*, 2020, **406**, 213146.
159 R. K. Wilharm, S.-Y. Huang, I. J. Gugger and V. C. Pierre, *Inorg. Chem.*, 2021, **60**, 15808–15817.
160 A. Roca-Sabio, M. Mato-Iglesias, D. Esteban-Gómez, É. Tóth, A. de Blas, C. Platas-Iglesias and T. Rodríguez-Blas, *J. Am. Chem. Soc.*, 2009, **131**, 3331–3341.
161 A. Hu, S. N. MacMillan and J. J. Wilson, *J. Am. Chem. Soc.*, 2020, **142**, 13500–13506.
162 S. L. Wu and W. D. W. Horrocks, *J. Chem. Soc., Dalton Trans.*, 1997, 1497–1502.
163 A. Hu, E. Aluicio-Sarduy, V. Brown, S. N. MacMillan, K. V. Becker, T. E. Barnhart, V. Radchenko, C. F. Ramogida, J. W. Engle and J. J. Wilson, *J. Am. Chem. Soc.*, 2021, **143**, 10429–10440.
164 T. Hatanaka, N. Kikkawa, A. Matsugami, Y. Hosokawa, F. Hayashi and N. Ishida, *Sci. Rep.*, 2020, **10**, 19468.
165 H. Singer, B. Drobot, C. Zeymer, R. Steudtner and L. J. Daumann, *Chem. Sci.*, 2021, **12**, 15581–15587.
166 J. A. Mattocks, J. L. Tirsch and J. A. Cotruvo, *Methods in Enzymology*, Elsevier, 2021, vol. 651, pp. 23–61.
167 Z. Dong, J. A. Mattocks, J. A. Seidel, J. A. Cotruvo and D. M. Park, *Sep. Purif. Technol.*, 2024, **333**, 125919.
168 J. Seidel, P. Diep, Z. Dong, J. A. Cotruvo and D. M. Park, *JACS Au*, 2024, **4**(11), 4273–4284.
169 C. S. Bonnet, M. Devocelle and T. Gunnlaugsson, *Org. Biomol. Chem.*, 2012, **10**, 126–133.
170 G. J.-P. Deblonde, J. A. Mattocks, H. Wang, E. M. Gale, A. B. Kersting, M. Zavarin and J. A. Cotruvo, *J. Am. Chem. Soc.*, 2021, **143**, 15769–15783.
171 G. J.-P. Deblonde, J. A. Mattocks, Z. Dong, P. T. Wooddy, J. A. Cotruvo and M. Zavarin, *Sci. Adv.*, 2021, **7**, eabk0273.
172 G. J.-P. Deblonde, K. Morrison, J. A. Mattocks, J. A. Cotruvo, M. Zavarin and A. B. Kersting, *Environ. Sci. Technol.*, 2023, **57**, 20830–20843.
173 R. M. Smith and A. E. Martell, *Sci. Total Environ*, 1987, **64**, 125–147.
174 J. A. Mattocks, J. A. Cotruvo and G. J.-P. Deblonde, *Chem. Sci.*, 2022, **13**, 6054–6066.
175 S. Özçubukçu, K. Mandal, S. Wegner, M. P. Jensen and C. He, *Inorg. Chem.*, 2011, **50**, 7937–7939.
176 H. Singer, R. Steudtner, A. S. Klein, C. Rulofs, C. Zeymer, B. Drobot, A. Pol, N. Cecilia Martinez-Gomez, H. J. M. Op den Camp and L. J. Daumann, *Angew. Chem., Int. Ed.*, 2023, **62**, e202303669.
177 A. Shah, M. J. Taylor, G. Molinaro, S. Anbu, M. Verdu, L. Jennings, I. Mikulska, S. Diaz-Moreno, H. E. L. Mkami, G. M. Smith, M. M. Britton, J. E. Lovett and A. F. A. Peacock, *Proc. Natl. Acad. Sci. U. S. A.*, 2023, **120**, e2219036120.
178 C. S. Bonnet, M. Devocelle and T. Gunnlaugsson, *Chem. Commun.*, 2008, 4552–4554.
179 S. K. Drake and J. J. Falke, *Biochemistry*, 1996, **35**, 1753–1760.
180 M. C. Heffern, L. M. Matosziuk and T. J. Meade, *Chem. Rev.*, 2014, **114**, 4496–4539.
181 A. J. Amoroso and S. J. A. Pope, *Chem. Soc. Rev.*, 2015, **44**, 4723–4742.
182 E. Mathieu, A. Sipos, E. Demeyere, D. Phipps, D. Sakaveli and K. E. Borbas, *Chem. Commun.*, 2018, **54**, 10021–10035.
183 U. Cho and J. K. Chen, *Cell Chem. Biol.*, 2020, **27**, 921–936.
184 J. H. S. K. Monteiro, *Molecules*, 2020, **25**, 2089.
185 R. Lengacher, K. E. Martin, D. Śmiłowicz, H. Esseln, P. Lotlikar, A. Grichine, O. Maury and E. Boros, *J. Am. Chem. Soc.*, 2023, **145**, 24358–24366.
186 J.-C. G. Bünzli, *Chem. Rev.*, 2010, **110**, 2729–2755.
187 S. V. Eliseeva, *Angew. Chem., Int. Ed.*, 2015, **54**, 8598.
188 A. D'Aléo, F. Pointillart, L. Ouahab, C. Andraud and O. Maury, *Coord. Chem. Rev.*, 2012, **256**, 1604–1620.
189 J.-C. G. Bünzli, *Coord. Chem. Rev.*, 2015, **293–294**, 19–47.
190 D. Kovacs and K. E. Borbas, *Coord. Chem. Rev.*, 2018, **364**, 1–9.
191 J. De Jersey, P. J. Morley and R. B. Martin, *Biophys. Chem.*, 1981, **13**, 233–243.
192 M. Latva, H. Takalo, V.-M. Mukkala, C. Matachescu, J. C. Rodríguez-Ubis and J. Kankare, *J. Lumin.*, 1997, **75**, 149–169.
193 W. D. Horrocks, J. P. Bolender, W. D. Smith and R. M. Supkowski, *J. Am. Chem. Soc.*, 1997, **119**, 5972–5973.
194 E. Falcone, P. Gonzalez, L. Lorusso, O. Sénèque, P. Faller and L. Raibaut, *Chem. Commun.*, 2020, **56**, 4797–4800.
195 A. M. Reynolds, B. R. Sculimbrene and B. Imperiali, *Bioconjugate Chem.*, 2008, **19**, 588–591.
196 J. Wang, X. Liu, K. Li, T. Shi, Q. Xu, T. Peng, Q. Huang, Z. Gao, H. Zhou, W. Lu and J. Wang, *J. Am. Chem. Soc.*, 2025, **147**, 15205–15215.
197 M. Starck, J. D. Fradgley, S. Di Vita, J. A. Mosely, R. Pal and D. Parker, *Bioconjugate Chem.*, 2020, **31**, 229–240.
198 H.-F. Chau, Y. Wu, W.-Y. Fok, W. Thor, W. C.-S. Cho, P. Ma, J. Lin, N.-K. Mak, J.-C. G. Bünzli, L. Jiang, N. J. Long, H. L. Lung and K.-L. Wong, *JACS Au*, 2021, **1**, 1034–1043.
199 J.-H. Choi, G. Fremy, T. Charnay, N. Fayad, J. Pécaut, S. Erbek, N. Hildebrandt, V. Martel-Frachet, A. Grichine and O. Sénèque, *Inorg. Chem.*, 2022, **61**, 20674–20689.
200 C. Cepeda, S. A. Denisov, D. Boturyn, N. D. McClenaghan and O. Sénèque, *Inorg. Chem.*, 2021, **60**, 17426–17434.
201 M. Isaac, L. Raibaut, C. Cepeda, A. Roux, D. Boturyn, S. V. Eliseeva, S. Petoud and O. Sénèque, *Chem. – Eur. J.*, 2017, **23**, 10992–10996.
202 Y.-H. Yeung, H.-F. Chau, H.-Y. Kai, W. Zhou, K. H.-Y. Chan, W. Thor, L. J. Charbonnière, F. Zhang, Y. Fan, Y. Wu and K.-L. Wong, *Adv. Opt. Mater.*, 2024, **12**, 2302070.
203 C. Cepeda, L. Raibaut, G. Fremy, S. V. Eliseeva, A. Romieu, J. Pécaut, D. Boturyn, S. Petoud and O. Sénèque, *Chem. – Eur. J.*, 2020, **26**, 13476–13483.
204 C. Penas, J. L. Mascareñas and M. E. Vázquez, *Chem. Sci.*, 2016, **7**, 2674–2678.
205 B. R. Sculimbrene and B. Imperiali, *J. Am. Chem. Soc.*, 2006, **128**, 7346–7352.
206 K. Y. Huang, L. Cardenas, A. D. Ellington and D. J. F. Walker, *Nat. Commun.*, 2024, **15**, 9200.

 This journal is © The Royal Society of Chemistry 2025

Open Access Article. Published on 22 September 2025. Downloaded on 4/1/2026 8:13:17 PM.
This article is licensed under a Creative Commons Attribution-NonCommercial 3.0 Unported Licence.

207 L. Raibaut, W. Vasseur, G. D. Shimberg, C. Saint-Pierre, J.-L. Ravanat, S. L. J. Michel and O. Sénèque, *Chem. Sci.*, 2017, **8**, 1658–1664.
208 E. Pazos, M. Goličnik, J. L. Mascareñas and M. E. Vázquez, *Chem. Commun.*, 2012, **48**, 9534–9536.
209 R. Sánchez-Fernández, A. Sánchez-Temprano, D. Esteban-Gómez and E. Pazos, *ChemBioChem*, 2023, **24**, e202300072.
210 E. Falcone, B. Vileno, M. Hoang, L. Raibaut and P. Faller, *J. Inorg. Biochem.*, 2021, **221**, 111478.
211 M. J. Scheuermann, C. R. Forbes and N. J. Zondlo, *Biochemistry*, 2018, **57**, 6956–6963.
212 J. Wahsner, E. M. Gale, A. Rodríguez-Rodríguez and P. Caravan, *Chem. Rev.*, 2019, **119**, 957–1057.
213 M. E. Ladd, P. Bachert, M. Meyerspeer, E. Moser, A. M. Nagel, D. G. Norris, S. Schmitter, O. Speck, S. Straub and M. Zaiss, *Prog. Nucl. Magn. Reson. Spectrosc.*, 2018, **109**, 1–50.
214 P. Caravan, *Chem. Soc. Rev.*, 2006, **35**, 512–523.
215 P. Caravan, J. J. Ellison, T. J. McMurry and R. B. Lauffer, *Chem. Rev.*, 1999, **99**, 2293–2352.
216 D. H. Powell, O. M. N. Dhubhghaill, D. Pubanz, L. Helm, Y. S. Lebedev, W. Schlaepfer and A. E. Merbach, *J. Am. Chem. Soc.*, 1996, **118**, 9333–9346.
217 J. J. Yang, J. Yang, L. Wei, O. Zurkiya, W. Yang, S. Li, J. Zou, Y. Zhou, A. L. W. Maniccia, H. Mao, F. Zhao, R. Malchow, S. Zhao, J. Johnson, X. Hu, E. Krogstad and Z.-R. Liu, *J. Am. Chem. Soc.*, 2008, **130**, 9260–9267.
218 S. Xue, H. Yang, J. Qiao, F. Pu, J. Jiang, K. Hubbard, K. Hekmatyar, J. Langley, M. Salarian, R. C. Long, R. G. Bryant, X. P. Hu, H. E. Grossniklaus, Z.-R. Liu and J. J. Yang, *Proc. Natl. Acad. Sci. U. S. A.*, 2015, **112**, 6607–6612.
219 C. S. Bonnet, P. H. Fries, S. Crouzy and P. Delangle, *J. Phys. Chem. B*, 2010, **114**, 8770–8781.
220 Y. Liu, D. Gao, Y. He, J. Ma, S. Y. Chong, X. Qi, H. J. Ting, Z. Luo, Z. Yi, J. Tang, C. Chang, J. Wang, Z. Sheng, H. Zheng and X. Liu, *Nat. Commun.*, 2024, **15**, 9834.
221 D. Li, M. Kirberger, J. Qiao, Z. Gui, S. Xue, F. Pu, J. Jiang, Y. Xu, S. Tan, M. Salarian, O. Ibhagui, K. Hekmatyar and J. J. Yang, *Invest. Radiol.*, 2024, **59**, 170–186.
222 F. Pu, M. Salarian, S. Xue, J. Qiao, J. Feng, S. Tan, A. Patel, X. Li, K. Mamouni, K. Hekmatyar, J. Zou, D. Wu and J. J. Yang, *Nanoscale*, 2016, **8**, 12668–12682.
223 M. Salarian, H. Yang, R. C. Turaga, S. Tan, J. Qiao, S. Xue, Z. Gui, G. Peng, H. Han, P. Mittal, H. E. Grossniklaus and J. J. Yang, *Biomaterials*, 2019, **224**, 119478.
224 S. Tan, H. Yang, S. Xue, J. Qiao, M. Salarian, K. Hekmatyar, Y. Meng, R. Mukkavilli, F. Pu, O. Y. Odubade, W. Harris, Y. Hai, M. L. Yushak, V. M. Morales-Tirado, P. Mittal, P. Z. Sun, D. Lawson, H. E. Grossniklaus and J. J. Yang, *Sci. Adv.*, 2020, **6**, eaav7504.
225 H. Yang, S. Tan, J. Qiao, Y. Xu, Z. Gui, Y. Meng, B. Dong, G. Peng, O. Y. Ibhagui, W. Qian, J. Lu, Z. Li, G. Wang, J. Lai, L. Yang, H. E. Grossniklaus and J. J. Yang, *Cancer Gene Ther.*, 2022, **29**, 1827–1839.
226 O. Y. Ibhagui, D. Li, H. Han, G. Peng, M. L. Meister, Z. Gui, J. Qiao, M. Salarian, B. Dong, Y. Yuan, Y. Xu, H. Yang, S. Tan, G. Satyanarayana, S. Xue, R. C. Turaga, M. Sharma, Y. Hai, Y. Meng, K. Hekmatyar, P. Sun, G. Sica, X. Ji, Z.-R. Liu and J. J. Yang, *Chem. Biomed. Imaging*, 2023, **1**, 268–285.
227 Q. N. Do, J. S. Ratnakar, Z. Kovács and A. D. Sherry, *ChemMedChem*, 2014, **9**, 1116–1129.
228 G. Angelovski and É. Tóth, *Chem. Soc. Rev.*, 2017, **46**, 324–336.
229 J. Lux and A. D. Sherry, *Curr. Opin. Chem. Biol.*, 2018, **45**, 121–130.
230 C. S. Bonnet and É. Tóth, *Curr. Opin. Chem. Biol.*, 2021, **61**, 154–169.
231 H. Lu, A. Chen, X. Zhang, Z. Wei, R. Cao, Y. Zhu, J. Lu, Z. Wang and L. Tian, *Nat. Commun.*, 2022, **13**, 7948.
232 M. Isaac, A. Pallier, F. Szeremeta, P.-A. Bayle, L. Barantin, C. S. Bonnet and O. Sénèque, *Chem. Commun.*, 2018, **54**, 7350–7353.
233 K. P. Malikidogo, A. Pallier, F. Szeremeta, C. S. Bonnet and O. Sénèque, *Dalton Trans.*, 2023, **52**, 6260–6266.
234 M. Sethurajan, E. D. van Hullebusch, D. Fontana, A. Akcil, H. Deveci, B. Batinic, J. P. Leal, T. A. Gasche, M. Ali Kucuker, K. Kuchta, I. F. F. Neto, H. M. V. M. Soares and A. Chmielarz, *Crit. Rev. Environ. Sci. Technol.*, 2019, **49**, 212–275.
235 K. Binnemans, P. T. Jones, T. Müller and L. Yurramendi, *J. Sustainable Metall.*, 2018, **4**, 126–146.
236 K. Binnemans, P. T. Jones, B. Blanpain, T. Van Gerven and Y. Pontikes, *J. Cleaner Prod.*, 2015, **99**, 17–38.
237 S. Pramanik, S. Kaur, I. Popovs, A. S. Ivanov and S. Jansone-Popova, *Eur. J. Inorg. Chem.*, 2024, e202400064.
238 N. C. Martinez-Gomez, H. N. Vu and E. Skovran, *Inorg. Chem.*, 2016, **55**, 10083–10089.
239 S. Dev, A. Sachan, F. Dehghani, T. Ghosh, B. R. Briggs and S. Aggarwal, *Chem. Eng. J.*, 2020, **397**, 124596.
240 R. M. Brown, A. Mirkouei, D. Reed and V. Thompson, *Renewable Sustainable Energy Rev.*, 2023, **173**, 113099.
241 M. Chakankar, F. Lederer, R. Jain, S. Matys, S. Kutschke and K. Pollmann, *Management of Electronic Waste*, John Wiley & Sons, Ltd, 2024, pp. 375–405.
242 X. Qian, C. Ma, H. Zhang and K. Liu, *Bioorg. Chem.*, 2024, **143**, 107040.
243 M. Vítová and D. Mezricky, *World J. Microbiol. Biotechnol.*, 2024, **40**, 189.
244 H. Singer, R. Steudtner, I. Sottorff, B. Drobot, A. Pol, H. J. M. O. den Camp and L. J. Daumann, *Chem. Commun.*, 2023, **59**, 9066–9069.
245 I. Chae, A. Shivkumar, F. M. Doyle and S.-W. Lee, *Nano Lett.*, 2024, **24**, 9946–9952.
246 I. Chae, F. M. Doyle and S.-W. Lee, *TMS 2025 154th Annual Meeting & Exhibition Supplemental Proceedings*, Springer, Cham, 2025, pp. 1139–1148.
247 D. M. Park, A. Brewer, D. W. Reed, L. N. Lammers and Y. Jiao, *Environ. Sci. Technol.*, 2017, **51**, 13471–13480.
248 A. Brewer, E. Chang, D. M. Park, T. Kou, Y. Li, L. N. Lammers and Y. Jiao, *Environ. Sci. Technol.*, 2019, **53**, 7714–7723.
249 A. Brewer, A. Dohnalkova, V. Shutthanandan, L. Kovarik, E. Chang, A. M. Sawvel, H. E. Mason, D. Reed, C. Ye, W. F.

Open Access Article. Published on 22 September 2025. Downloaded on 4/1/2026 8:13:17 PM.
This article is licensed under a Creative Commons Attribution-NonCommercial 3.0 Unported Licence.

Hynes, L. N. Lammers, D. M. Park and Y. Jiao, *Environ. Sci. Technol.*, 2019, **53**, 13888–13897.
250 D. Park, A. Middleton, R. Smith, G. Deblonde, D. Laudal, N. Theaker, H. Hsu-Kim and Y. Jiao, *Sep. Purif. Technol.*, 2020, **241**, 116726.
251 E. Chang, A. W. Brewer, D. M. Park, Y. Jiao and L. N. Lammers, *Appl. Geochem.*, 2020, **112**, 104478.
252 X. Xie, K. Yang, Y. Lu, Y. Li, J. Yan, J. Huang, L. Xu, M. Yang and Y. Yan, *J. Hazard. Mater.*, 2022, **438**, 129561.
253 M. Gut, T. Wilhelm, O. Beniston, S. Ogundipe, C.-C. Kuo, K. Nguyen and A. Furst, *Adv. Mater.*, 2025, **37**, 2412607.
254 F. F. Khoury, B. S. Heater, D. R. Marzolf, S. S. Abeyrathna, J. W. Picking, P. Kumar, S. A. Higgins, R. Jones, A. T. Lewis, K. H. Kucharzyk and S. Banta, *Chem. Sci.*, 2025, **16**, 15333–15346.
255 P. K. R. Tay, A. Manjula-Basavanna and N. S. Joshi, *Green Chem.*, 2018, **20**, 3512–3520.
256 R. A. Scheel, J. K. Sahoo, L. D. Morton, Z. Xia, J. R. Blum, Z. Martin-Moldes and D. L. Kaplan, *ACS ES&T Eng.*, 2024, **4**(9), 2135–2144.
257 Z. Dong, J. A. Mattocks, G. J.-P. Deblonde, D. Hu, Y. Jiao, J. A. Cotruvo and D. M. Park, *ACS Cent. Sci.*, 2021, **7**, 1798–1808.
258 Z. Hussain, S. Kim, J. Cho, G. Sim, Y. Park and I. Kwon, *Adv. Funct. Mater.*, 2022, **32**, 2109158.
259 Z. Hussain, D. Dwivedi and I. Kwon, *Front. Bioeng. Biotechnol.*, 2024, **12**, DOI: 10.3389/fbioe.2024.1385845.
260 Q. Ye, X. Jin, B. Zhu, H. Gao and N. Wei, *Environ. Sci. Technol.*, 2023, **57**, 4276–4285.
261 L. Johnson and C. E. Duval, *Langmuir*, 2025, **41**, 9581–9589.
262 Q. Ye, X. Jin, B. Zhu, H. Gao and N. Wei, *Environ. Sci. Technol.*, 2023, **57**, 4276–4285.
263 H. Jin, D. M. Park, M. Gupta, A. W. Brewer, L. Ho, S. L. Singer, W. L. Bourcier, S. Woods, D. W. Reed, L. N. Lammers, J. W. Sutherland and Y. Jiao, *ACS Sustainable Chem. Eng.*, 2017, **5**, 10148–10155.
264 J. T. Welch, M. Sirish, K. M. Lindstrom and S. J. Franklin, *Inorg. Chem.*, 2001, **40**, 1982–1984.
265 M. Sirish and S. J. Franklin, *J. Inorg. Biochem.*, 2002, **91**, 253–258.
266 Y. Kim and S. J. Franklin, *Inorg. Chim. Acta*, 2002, **341**, 107–112.
267 L. Wang, K. Liu, Z. Song, H. Do, L. Yang, J. Wu, L. Jiang and H. Yu, *Colloids Surf., B*, 2025, **251**, 114596.
268 M. J. Allen, *Synlett*, 2016, 1310–1317.
269 H. Pellissier, *Coord. Chem. Rev.*, 2017, **336**, 96–151.
270 Y. Qiao and E. J. Schelter, *Acc. Chem. Res.*, 2018, **51**, 2926–2936.
271 A. Prieto and F. Jaroschik, *Curr. Org. Chem.*, 2022, **26**, 6–41.
272 N. Mahieu, J. Piątkowski, T. Simler and G. Nocton, *Chem. Sci.*, 2023, **14**, 443–457.
273 R. Bhimpuria, R. Charaf, K. Ye, A. Thapper, H. Sathyan, M. Ahlquist, L. Hammarström and K. E. Borbas, *Chem*, 2025, 102547.
274 R. Bhimpuria, M. Tomar, A. Thapper, M. Ahlquist and K. E. Borbas, *Chem*, 2025, 102450.
275 F. Schwizer, Y. Okamoto, T. Heinisch, Y. Gu, M. M. Pellizzoni, V. Lebrun, R. Reuter, V. Köhler, J. C. Lewis and T. R. Ward, *Chem. Rev.*, 2018, **118**, 142–231.
276 P. Kouba, P. Kohout, F. Haddadi, A. Bushuiev, R. Samusevich, J. Sedlar, J. Damborsky, T. Pluskal, J. Sivic and S. Mazurenko, *ACS Catal.*, 2023, **13**, 13863–13895.
277 P. Notin, N. Rollins, Y. Gal, C. Sander and D. Marks, *Nat. Biotechnol.*, 2024, **42**, 216–228.
278 A. Winnifrith, C. Outeiral and B. L. Hie, *Curr. Opin. Struct. Biol.*, 2024, **86**, 102794.
279 K. K. Yang, Z. Wu and F. H. Arnold, *Nat. Methods*, 2019, **16**, 687–694.
280 J. A. Mattocks, J. J. Jung, C.-Y. Lin, Z. Dong, N. H. Yennawar, E. R. Featherston, C. S. Kang-Yun, T. A. Hamilton, D. M. Park, A. K. Boal and J. A. Cotruvo, *Nature*, 2023, **618**, 87–93.

 This journal is © The Royal Society of Chemistry 2025